# MEASUREMENT OF $\sigma \cdot BR(W + \gamma)$ AND $\sigma \cdot BR(Z + \gamma)$ AND SEARCH FOR ANOMALOUS $W\gamma$ AND $Z\gamma$ COUPLINGS AT $\sqrt{s} = 1.8$ TEV

BY

MARK FRANK VONDRACEK

B.S., University of Illinois at Urbana-Champaign, 1990
M.S., University of Illinois at Urbana-Champaign, 1992

THESIS

Submitted in partial fulfillment of the requirements
for the degree of Doctor of Philosophy in Physics
in the Graduate College of the
University of Illinois at Urbana-Champaign, 1995

Urbana, Illinois

# UNIVERSITY OF ILLINOIS AT URBANA-CHAMPAIGN

*GRADUATE COLLEGE DEPARTMENTAL FORMAT APPROVAL*

THIS IS TO CERTIFY THAT THE FORMAT AND QUALITY OF PRESENTATION OF THE THESIS SUBMITTED BY MARK FRANK VONDRACEK AS ONE OF THE REQUIREMENTS FOR THE DEGREE OF DOCTOR OF PHILOSOPHY ARE ACCEPTABLE TO THE DEPARTMENT OF PHYSICS.

*Full Name of Department, Division or Unit*

11/15/94

*Date of Approval*

Robert A. Williams

*Departmental Representative*

MEASUREMENT OF $\sigma \cdot BR(W + \gamma)$ AND $\sigma \cdot BR(Z + \gamma)$ AND SEARCH FOR ANOMALOUS $W\gamma$ AND $Z\gamma$ COUPLINGS AT $\sqrt{s} = 1.8$ TEV

Mark Frank Vondracek, Ph.D.
Department of Physics
University of Illinois at Urbana-Champaign, 1994
Professor Tony Liss, Advisor

Measurements of the production cross section times branching ratio for $W + \gamma$ and $Z + \gamma$ processes, where the $W$ decays into a muon and neutrino and the $Z$ decays into a muon pair, have been made from the analysis of $18.6 \pm 0.7\ pb^{-1}$ of high-$P_T$ muon data from proton-antiproton ($p\overline{p}$) collisions. The data were collected with the Collider Detector at Fermilab (CDF) during the 1992-93 run. In a search for central photons ($|\eta| < 1.1$) with transverse energy above 7 $GeV$ and angular separation from the muon by at least $\Delta R = 0.7$, where $\Delta R = \sqrt{\Delta\phi^2 + \Delta\eta^2}$, we find 7 $W\gamma$ and 4 $Z\gamma$ candidates. This translates into cross section times branching ratios of $9.0 \pm 6.4\ pb$ for the $W\gamma$ process and $6.6 \pm 3.4\ pb$ for the $Z\gamma$ process. Separate measurements were made for photon $E_T$ values above 11 $GeV$ and 15 $GeV$. The cross section times branching ratio results were used to calculate a series of cross section ratios. An analysis designed to search for anomalous couplings between the gauge bosons was also carried out using these results. Assuming only one anomalous coupling to be non-zero at a time, the 95% CL limits on $W\gamma$ anomalous couplings are, $-3.7 < \Delta\kappa < 3.7$, $-1.2 < \lambda < 1.2$, $-3.8 < \tilde{\kappa} < 3.8$ and $-1.2 < \tilde{\lambda} < 1.2$. For $ZZ\gamma$ anomalous couplings the experimental limits are measured to be, at the 95% CL, $-4.6 < h_{30}^Z(h_{10}^Z) < 4.6$ and $-1.1 < h_{40}^Z(h_{20}^Z) < 1.1$. For $Z\gamma\gamma$ anomalous couplings the experimental limits are measured to be, at the 95% CL, $-4.9 < h_{30}^\gamma(h_{10}^\gamma) < 4.9$ and

$-1.2 < h_{40}^{\gamma}(h_{20}^{\gamma}) < 1.2$. Limits are placed on electromagnetic multipole moments for both the $W$ and $Z$ bosons using the measured limits of the anomalous couplings, and are presented in this thesis. All of the measurements presented in this thesis are consistent with Standard Model expectations.

I dedicate this to my loving parents, Rod and Patricia Vondracek,
because without their guidance and support this would never have happened.

# Acknowledgments

There have been many individuals who have helped me as I traveled the academic road to this point, and, though not all can be mentioned here, my deepest appreciation and thanks go out to them all. Some special thanks goes out to all my teachers along the way since they gave me the necessary building blocks to put two and two together. To Eric and Rodney, thanks for the countless hours of working those killer problem sets from "The Baym Show". To Dave and Jerry for keeping the computer system operational while this work was completed. To the masses of fellow collaborators at CDF, thanks for your help and expertise when collecting and analyzing the data. To the b-ballers (aka b-MAULers), thanks for the many spills and thrills during our sporting adventures...you all know who you are! To Shirley, Sue, and Tom, thanks for all your help with providing transportation to FNAL and for turning in all the travel vouchers. To Harold and Lee, thanks for all your help and advice when I had questions about any electronics gizmos.

To all my colleagues in Urbana (I'm sure I'll miss some): Chris, Doug, Dave, Ray, Debbie, Lee, the Dr. Toms, Rob, Alain, and last but not least Randrew, a big thanks! A *very* special thanks to Steve; this would never have been possible had you not answered my countless questions and spent so many hours trying to decipher my email. It was a wonderful experience working with you! And Tony, one couldn't wish for a better advisor

and teacher...thanks for everything. Maybe the Knicks will actually win a title for you; the Bulls have given us three so perhaps NY will have another opportunity to get one.

Finally, my greatest thanks to my family and my wife Kathy; your support from the very beginning is the reason I'm writing this now.

This research was supported in part by the U.S. Department of Energy under contract DE-FG02-91ER-40677 and the Alfred P. Sloan Foundation.

# Table of Contents

# List of Tables

# List of Figures

# Chapter 1

# Introduction

High energy particle physics is currently described within the framework of the Standard Model (SM) [1]. One of the foundations of the SM is the Glashow-Weinberg-Salam (GWS) theory of electroweak interactions. The GWS theory presents the electromagnetic and weak forces, two of four known forces in nature, as different manifestations of a single force which exists in high energy realms. The unified electroweak force is described by the gauge group $SU(2)_L \otimes U(1)_Y$, where $L$ represents weak isospin and $Y$ respresents hypercharge. A direct consequence of the SM is the existence of massive vector gauge bosons, the $W^{\pm}$ and $Z^0$, which mediate the weak charged and neutral currents, respectively. A massless gauge boson, the photon ($\gamma$), is responsible for the electromagnetic force. The remaining two forces in nature, the strong nuclear force and gravity, are also believed to be carried by massless particles. The strong force, which governs the behavior of quarks within nuclei, is mediated via the exchange of 'gluons' and is described by another foundational theory included in the SM called Quantum Chromodynamics

| *Particle* | *Associated Force* | *Mass* ($GeV/c^2$) | *Spin* | *Range of Force* |
|---|---|---|---|---|
| Gluon | Strong | 0 | $1\hbar$ | $\leq 1$ fm |
| $W^{\pm}$ | Weak Charged Current | 80.2 | $1\hbar$ | $\sim 10^{-3}$ fm |
| $Z^0$ | Weak Neutral Current | 91.2 | $1\hbar$ | $\sim 10^{-3}$ fm |
| Photon | Electromagnetic | 0 | $1\hbar$ | $\infty$ |
| Graviton | Gravity | 0 | $2\hbar$ | $\infty$ |

**Table 1.1**: Characteristics of Force-Carrying Particles.

(QCD). The more familiar gravitational force is believed to be mediated via the exchange of 'gravitons', although no realistic quantum theory of gravity exists at the present time which would describe such processes. Table 1.1 shows some basic characteristics of the particles which are responsible for the various forces.

Along with the gauge bosons, the SM requires three generations, or families, of fundamental particles which are the basic constituents of matter as we know it. The particles, which are known as fermions (spin 1/2 particles), are grouped into two classes, called leptons and quarks. The leptons are known as the electron, $e$, muon, $\mu$, and tau, $\tau$, along with their associated neutrinos $\nu_e$, $\nu_\mu$ and $\nu_\tau$. The quarks are known as up, $u$, down, $d$, charm, $c$, strange, $s$, bottom, $b$, and top, $t$. The generations can be represented as

$$\textit{Leptons} \qquad \begin{pmatrix} e \\ \nu_e \end{pmatrix} \begin{pmatrix} \mu \\ \nu_\mu \end{pmatrix} \begin{pmatrix} \tau \\ \nu_\tau \end{pmatrix}$$

$$\textit{Quarks} \qquad \begin{pmatrix} u \\ d \end{pmatrix} \begin{pmatrix} c \\ s \end{pmatrix} \begin{pmatrix} t \\ b \end{pmatrix}$$

Table 1.2 shows various properties of the leptons and quarks.

| Particle | Mass ($MeV/c^2$) | Charge ($e$) |
|---|---|---|
| $e$ ($\nu_e$) | 0.511 ($< 7 \times 10^{-6}$) | -1 (0) |
| $\mu$ ($\nu_\mu$) | 105 ($< 0.27$) | -1 (0) |
| $\tau$ ($\nu_\tau$) | 1777 ($< 35$) | -1 (0) |
| $u$ ($d$) | 2-8 (5-15) | $+\frac{2}{3}$ ($-\frac{1}{3}$) |
| $c$ ($s$) | 1300-1700 (100-300) | $+\frac{2}{3}$ ($-\frac{1}{3}$) |
| $t$ ($b$) | $\sim 1.74 \times 10^5$ (4700-5300) | $+\frac{2}{3}$ ($-\frac{1}{3}$) |

**Table 1.2**: Characteristics of Leptons and Quarks.

All quarks and leptons have been observed with the exception of the heavy top quark, $t$. However, the CDF experiment has found initial, direct evidence for the top's existence and, *assuming* that it is the top quark, has measured its mass as $174 \pm 17$ $GeV/c^2$ [2]. The D0 experiment, also at Fermilab, has established a lower limit on the mass of $t$ of 131 $GeV/c^2$ [3].

The SM predicts various properties of the gauge bosons and fermions. Some examples are production cross sections and decay branching ratios. It also predicts how these particles should behave when interacting with each other in the presence of the electroweak force. Many of the SM predictions have been measured experimentally with good precision, and in all cases no significant discrepancies have been observed between theory and experiment. However, not all aspects of the SM have been well-measured. For example, the non-Abelian nature of the GWS theory allows the gauge bosons to couple to each other. The properties associated with multi-boson vertices and the ensuing implications of possible non-SM, anomalous couplings between the gauge bosons are observable in a group of processes that have a small cross section. As a result, measurements associated with multi-boson vertices have been statistically limited. Anomalous couplings between

gauge bosons would arise if the $W$ and $Z$ bosons are composite particles. If anomalous couplings between $W$, $Z$ and photons exist, the cross sections for events having $W + \gamma$ or $Z + \gamma$ in the final state would be higher than the cross sections predicted by the SM, which assumes the $W$ and $Z$ are fundamental point-like particles. One would also observe different kinematic distributions compared to SM predictions, such as the transverse energy spectra of the final-state photons, if $W$ and $Z$ bosons are composite particles. Composite gauge bosons would mean the SM does not provide the ultimate description of high energy physics since the fundamentality of these particles is one of the foundations of the theory. The measurement of diboson production cross sections and the search for anomalous couplings is an important test of the SM, and results using data collected in 1992-93 with the Collider Detector at the Fermilab Tevatron are discussed in this thesis.

# Chapter 2

# Theory of $W\gamma$ and $Z\gamma$ Production

## 2.1 $W\gamma$ Production

The production of a $W$ and photon in the final state can arise from several types of processes. The relevant tree-level Feynman diagrams are shown in Figures 2.1a-d. The most interesting process is the $s$-channel diagram, shown in Figure 2.1c, since it deals with a 3-boson vertex. Figures 2.1a-b (the $u$- and $t$-channel diagrams, respectively) represent initial state radiation off of one of the quarks while Figure 2.1d represents final state/inner brehmsstrahlung of a photon from the lepton. Note that only a $WW\gamma$ vertex is shown as a result of the direct coupling of $W$ bosons to photons; $W\gamma\gamma$ and $WZ\gamma$ vertices are forbidden due to conservation of electric charge. In order to preserve electromagnetic gauge invariance, all of the Feynman diagrams must be summed together coherently when calculating matrix elements for $W\gamma$ production since all the diagrams

have the same final state, which, in this analysis, is a muon and neutrino from the $W$ decay (not shown in Fig. 2.1a-c) along with a photon.

The most general effective Lagrangian for $W\gamma$ production, with anomalous couplings, which preserves electromagnetic gauge invariance and Lorentz invariance for tree-level processes is given by [4]

$$L_{WW\gamma} = -ie[W^{\dagger}_{\mu\nu}W^{\mu}A^{\nu} - W^{\dagger}_{\mu}A_{\nu}W^{\mu\nu} + \kappa_f W^{\dagger}_{\mu}W_{\nu}F^{\mu\nu} + \frac{\lambda_f}{M_W^2}W^{\dagger}_{\lambda\mu}W^{\mu}_{\nu}F^{\nu\lambda} + \tilde{\kappa}_f W^{\dagger}_{\mu}W_{\nu}F'^{\mu\nu} + \frac{\tilde{\lambda}_f}{M_W^2}W^{\dagger}_{\lambda\mu}W^{\mu}_{\nu}F'^{\nu\lambda}] \qquad (2.1)$$

where $A^{\mu}$ and $W^{\mu}$ are the photon and $W$ fields, respectively, and $W_{\mu\nu} = \partial_{\mu}W_{\nu} - \partial_{\nu}W_{\mu}$, $F_{\mu\nu} = \partial_{\mu}A_{\nu} - \partial_{\nu}A_{\mu}$, $F'_{\mu\nu} = \frac{1}{2}\epsilon_{\mu\nu\rho\sigma}F^{\rho\sigma}$, $e$ is the charge of the proton, and $M_W$ is the mass of the $W$. The variables $\Delta\kappa_f = \kappa_f - 1$, $\lambda_f$, $\tilde{\kappa}_f$ and $\tilde{\lambda}_f$ are form factors. The photon is taken to be on-shell, while both the on-shell and virtual $W$ bosons are assumed to couple to massless fermions to allow $\partial_{\mu}W^{\mu} = 0$.

Within the SM the momentum-dependent form factors $a_f(P^2, q_1^2, q_2^2)$, where $a_f(P^2, q_1^2, q_2^2) = \Delta\kappa_f$, $\lambda_f$, $\tilde{\kappa}_f$, or $\tilde{\lambda}_f$, are predicted to have values of 0 at tree level. In this notation $P$ is the four-momentum of the intermediate $W$ boson, $q_1$ is the four-momentum of the final-state $W$, and $q_2$ is the four-momentum of the photon. The form factors are assumed to have a generalized dipole form [4], analogous to the proton and neutron form factors, of

$$a_f(P^2 = \hat{s}, q_1^2 = M_W^2, q_2^2 = 0) = \frac{a_0}{(1 + \hat{s}/\Lambda_W^2)^n} \qquad (2.2)$$

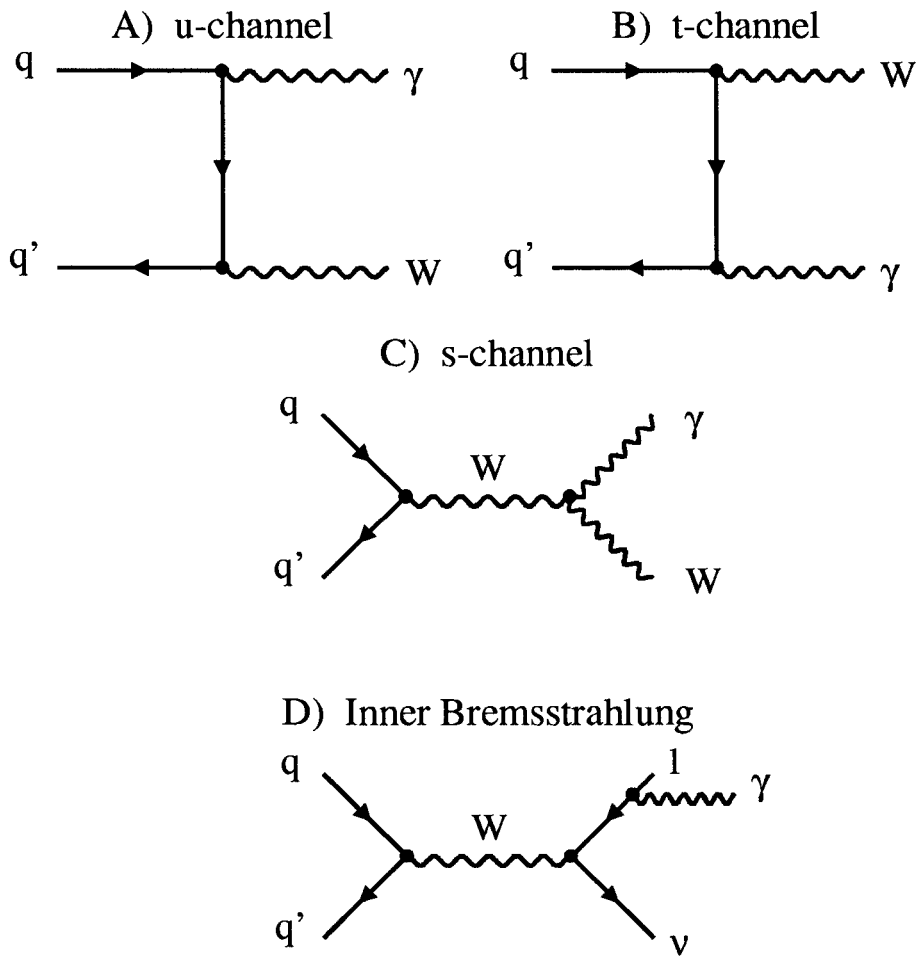


**Figure 2.1**: Feynman diagrams for $W\gamma$ production. This analysis searches for events where the $W$ decays into a muon and neutrino.

where the dimensionless anomalous couplings $a_0 = \Delta\kappa \equiv \kappa - 1, \lambda, \tilde{\kappa}$ or $\tilde{\lambda}$. In the SM these are all equal to 0 at tree level. All four of the couplings are even under the charge conjugation operator, $C$. The couplings $\Delta\kappa$ and $\lambda$ are even under parity, $P$, making them $CP$-conserving, whereas $\tilde{\kappa}$ and $\tilde{\lambda}$ are odd under parity, making them $CP$-violating. In Equation (2.2) we take $n = 2$ in order to guarantee the preservation of unitarity at high energies (see Section 2.3). The variable $\Lambda_W$ represents a form factor energy scale; that is, $\Lambda_W$ determines an energy scale at which new physics would become observable in the weak boson sector due to the compositeness of the $W$. The behavior of the generalized dipole form factors $a_f$ is shown in Figure 2.2, for exponent values of $n = 1, 2, 3, 4$. In this plot the center of mass energy $\sqrt{\hat{s}} = M_W = 80.2$ GeV.

The anomalous couplings can be related to classical electromagnetic multipole moments of the $W$ boson in the static limit, where the photon energy goes to 0. The expressions are given by [4] (with $\hbar = c = 1$)

$$\mu_W = \frac{e}{2M_W}(2 + \Delta\kappa + \lambda) \tag{2.3}$$

$$Q_W^e = -\frac{e}{M_W^2}(1 + \Delta\kappa - \lambda) \tag{2.4}$$

$$d_W^e = \frac{e}{2M_W}(\tilde{\kappa} + \tilde{\lambda}) \tag{2.5}$$

$$Q_W^m = -\frac{e}{M_W^2}(\tilde{\kappa} - \tilde{\lambda}) \tag{2.6}$$

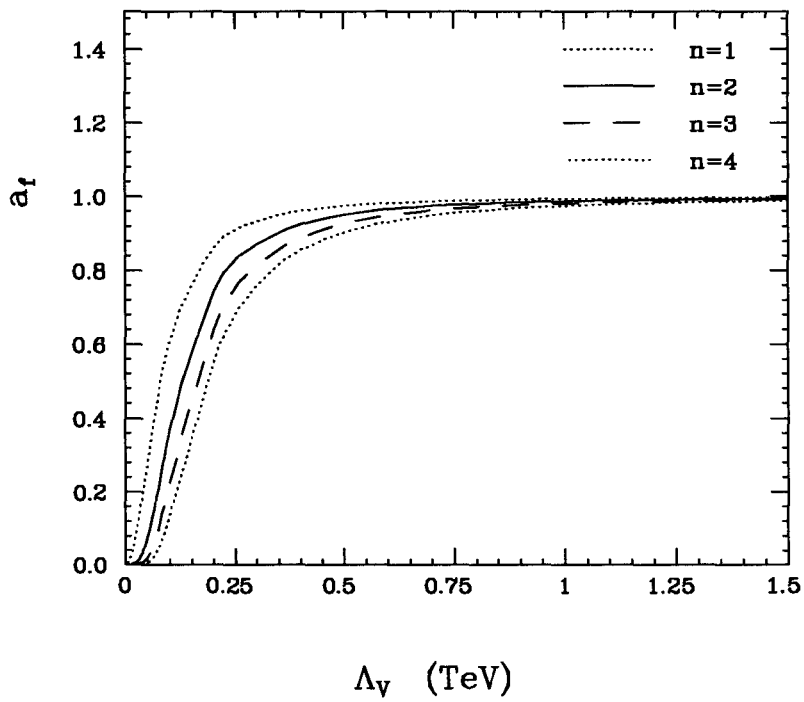


**Figure 2.2**: Behavior of the generalized dipole form factors assumed for the $W\gamma$ and $Z\gamma$ processes. The form factor $a_f$ vs $\Lambda_V$ for the coupling $a_0 = 1$ and the choices of form factor exponents $n = 1, 2, 3, 4$ are shown. The center of mass energy is taken to be $\sqrt{\hat{s}} = M_W = 80.2$ GeV.

where $\mu_W$ is the magnetic dipole moment, $Q_W^e$ is the electric quadrupole moment, $d_W^e$ is the electric dipole moment, and $Q_W^m$ is the magnetic quadrupole moment. One can also relate the mean-squared charge radius of the $W$ boson to the anomalous couplings as

$$< R_W^2 >= \frac{1}{M_W^2}(1 + \Delta\kappa + \lambda) \tag{2.7}$$

The $W$ is expected to have both a magnetic dipole and electric quadrupole moment within the SM because, for an arbitrary particle of spin $S$, $2S + 1$ $CP$-conserving electromagnetic moments are allowed [7]. Due to the symmetry properties of the various anomalous couplings, $\mu_W$ and $Q_W^e$ are $CP$-conserving and $d_W^e$ and $Q_W^m$ are $CP$-violating. Measurements on the magnitude of the neutron electric dipole moment, $d_n$, lead to *indirect*, model-dependent limits on the $CP$-violating couplings, $\tilde{\kappa}$ and $\tilde{\lambda}$. The upper limit on $d_n$ is $12 \times 10^{-26}$ $e - cm$ [8] and this implies $|\tilde{\kappa}|, |\tilde{\lambda}| < O(10^{-3})$ [9]. In Chapter 8 *direct* limits on these $CP$-violating couplings, extracted from data, will be presented. It will also be shown that the indirect limits extracted from the neutron electric dipole study are, after further theoretical review, not as good as previously thought, and that indeed the direct limits we set are needed to get a better idea of the magnitude of the $CP$-violating couplings.

The various Feynman diagrams of Figure 2.1 result in events with different kinematic properties. For example, the brehmsstrahlung diagram tends to emit photons that are colinear with the lepton, whereas photons emitted by the quarks (Figures 2.1a,b) tend to be colinear with the proton-antiproton beams. In all cases the photon transverse energy

($E_T$) spectra are peaked at photon energies of 0. In this analysis I'm most interested in Figure 2.1c and, as will be discussed below, I try to use appropriate selection criteria to separate out $W\gamma$ production events based on such kinematic information.

It is possible to represent the anomalous contributions to the $W\gamma$ production amplitudes in terms of the helicity states (dot product of a particle's spin and momentum) of the $W$ and photon, $\beta_W$ and $\beta_\gamma$. Denoting these contributions by $\Delta M_{\beta_\gamma \beta_W}$ one can write [4]

$$\Delta M_{\pm 0} = \frac{e^2}{\sin\theta_W} \frac{\sqrt{\hat{s}}}{2M_W} [\Delta\kappa + \lambda \mp i(\tilde{\kappa} + \tilde{\lambda})] \frac{1}{2}(1 \mp \cos\Theta) \tag{2.8}$$

$$\Delta M_{\pm\pm} = \frac{e^2}{\sin\theta_W} \frac{1}{2} [\frac{\hat{s}}{M_W^2}(\lambda \mp i\tilde{\lambda}) + (\Delta\kappa \mp i\tilde{\kappa})] \frac{1}{\sqrt{2}} \sin\Theta \tag{2.9}$$

Only four pairs of helicity combinations are allowed, as shown in the equations above. The combinations $(\beta_\gamma, \beta_W) = (+-)$ and $(-+)$ are forbidden by angular momentum conservation because they require a total spin of $J = 2$ for a $W$ boson, and we assume that the $W$ boson has the SM value spin $J = 1$. Figures 2.3a-d shows the four allowed combinations in terms of spin and momentum vectors in the rest frame of the off-shell $W$ in the $WW\gamma$ system. The fact that there are four allowed helicity states explains why four free parameters suffice to parameterize all effects of the $WW\gamma$ vertex in the production of $W\gamma$ events. Figures 2.3e-f show two helicity states in the same system which are *not* allowed because the $W$ does not possess a spin of $J = 2$. The combinations are all taken at tree level.

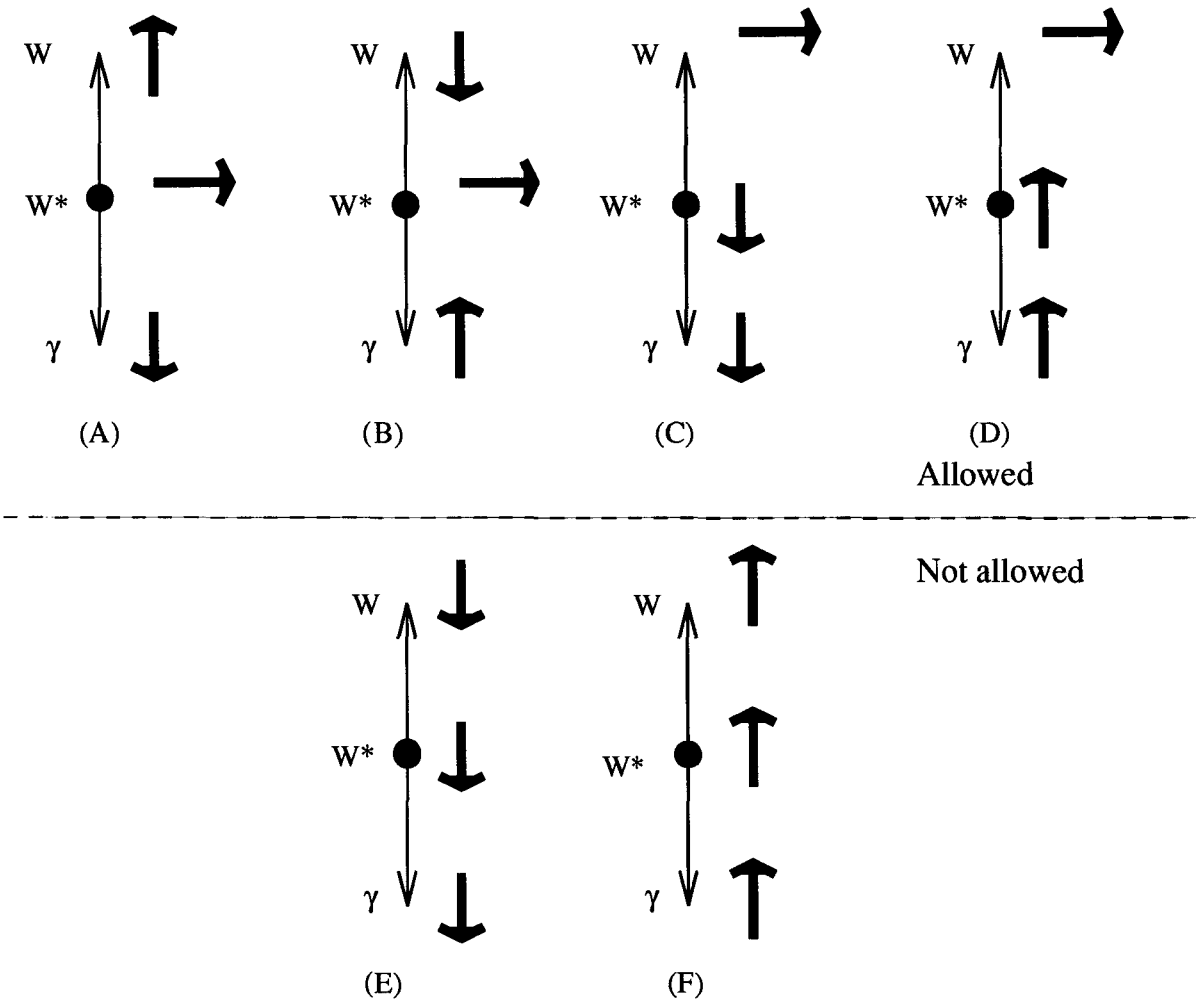


**Figure 2.3**: Helicity states in the $W^*$ rest frame. Figures (A)-(D) are allowed states, whereas Figures (E) and (F) are not allowed because of conservation of angular momentum, i.e the off-shell $W$ would need $J = 2$.

The production cross sections and event yield due to anomalous couplings are proportional to the square of the anomalous amplitude, shown above. For example, one can generally express the theoretical event yield for $W\gamma$ and $Z\gamma$ processes, as a function of four anomalous couplings, as

$$N(x,y,u,v) = N_{SM}^{pred} + ax + bx^2 + cy + dy^2 + exy + \beta u^2 + \delta v^2 + \epsilon uv \qquad (2.10)$$

where $x, y$ are $CP$-conserving couplings and $u, v$ are $CP$-violating couplings. The variables $a, b, c, d, e, \beta, \delta$, and $\epsilon$ are constants. Because the $CP$-conserving anomalous couplings in Eqs. 2.8 and 2.9 form the real part of the production amplitude and the $CP$-violating couplings form the imaginary part of the amplitude, there can be no cross terms in Eq. 2.10 between $x, y$ and $u, v$. Equation 2.10 will be used in the analysis to help extract limits on possible anomalous couplings (see Ch. 8).

An interesting consequence of coherently adding together all the Feynman diagrams in Figure 2.1 is that interference effects arise. For large scattering angles $\Theta$ between the photon and incoming quark in the $W\gamma$ center of mass frame, the $t$-channel and $u$-channel diagrams add destructively with the $s$-channel diagram when $\cos\Theta = -\frac{1}{3}$. The result is a "radiation zero" in the differential cross section $d\sigma/dcos\Theta$ for $W\gamma$ production [4]. This radiation zero also presents itself as a dip in the photon rapidity distribution in the center of mass frame, $y^*$[1], as shown in Figure 2.4. In real data, however, this dip in

[1]Rapidity is defined as $y^* = \frac{1}{2}\ln\frac{E+P_z}{E-P_z}$, where $E$ is energy and $P_z$ is the $z$-component of momentum.

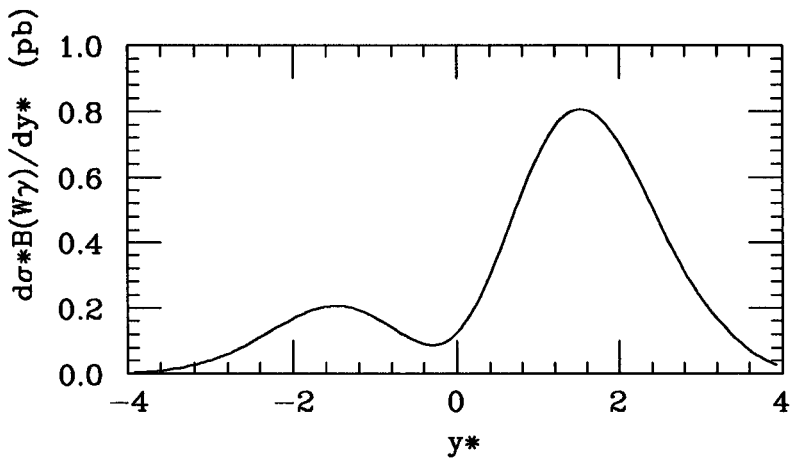


**Figure 2.4**: The photon center of mass rapidity distribution of $W\gamma$ events, where the $W$ is positively charged. The dip is predicted by the SM, and is the result of the "radiation zero". This distribution would be peaked and centered on 0 if there was no such radiation zero.

the rapidity distribution is expected to be partially filled in due to a number of things, such as misreconstruction of events, background processes, higher order QCD corrections [10], and structure function effects. From Equations 2.8 and 2.9 it is also clear that non-zero values of $\Delta\kappa$, $\lambda$, $\tilde{\kappa}$ and $\tilde{\lambda}$ will also contribute to filling the dip since none of the anomalous contributions to the scattering amplitude vanish at $\cos\Theta = -\frac{1}{3}$. In the future it may be possible to use the radiation zero to provide a sensitive means of investigating possible anomalous couplings, as larger statistics samples are collected. A related method of making use of the radiation zero is to use distributions of pseudorapidity differences between the lepton from the $W$ decay and the photon [6]. This method has an added benefit of using quantities from the lab frame rather than the $W\gamma$ rest frame. Such possibilities will be discussed in greater detail in Chapter 9.

## 2.2 $Z\gamma$ Production

As in the $W\gamma$ case, there are several processes which can lead to a final state $Z$ and photon. The tree-level Feynman diagrams for $Z\gamma$ production are shown in Figures 2.5a-d. In this analysis, events of interest are those which have a muon pair from the $Z$ decay (not shown in Fig. 2.5a,b,d) in association with a photon. The SM predicts no $ZZ\gamma$ or $Z\gamma\gamma$ couplings at the tree level because, like the photon, the $Z$ is its own antiparticle and therefore cannot have any static electromagnetic multipole moments. The $Z$ boson is also a neutral particle, and photons only directly couple to electric charge. Figures 2.5a-c, therefore, are the SM diagrams for $Z\gamma$ production and correspond to initial and final state radiation in the form of inner brehmsstrahlung. Only if one were to assume there are non-SM anomalous couplings can diagrams with a 3-boson vertex (Figure 2.5d) be drawn. Due to energy conservation, if non-zero anomalous $ZZ\gamma$ or $Z\gamma\gamma$ couplings exist, one of the $Z$ bosons or photons must be off-shell.

A convenient and useful way of looking at the $ZZ\gamma$ vertex is by writing the most general anomalous $ZZ\gamma$ vertex function. This also takes into account four different non-SM anomalous couplings, as allowed by electromagnetic gauge invariance. The $ZZ\gamma$ vertex function is given in Ref. [5], and is

$$\Gamma^{\alpha\beta\mu}_{Z\gamma Z}(q_1,q_2,P) = (\frac{P^2-q_1^2}{M_Z^2}) \times [h_1^Z(q_2^\mu g^{\alpha\beta} - q_2^\alpha g^{\mu\beta}) + \frac{h_2^Z}{M_Z^2}P^\alpha(P\cdot q_2 g^{\mu\beta} - q_2^\mu P^\beta) + h_3^Z \epsilon^{\mu\alpha\beta\rho} q_{2\rho} + \frac{h_4^Z}{M_Z^2} P^\alpha \epsilon^{\mu\beta\rho\sigma} P_\rho q_{2\sigma}] \quad (2.11)$$

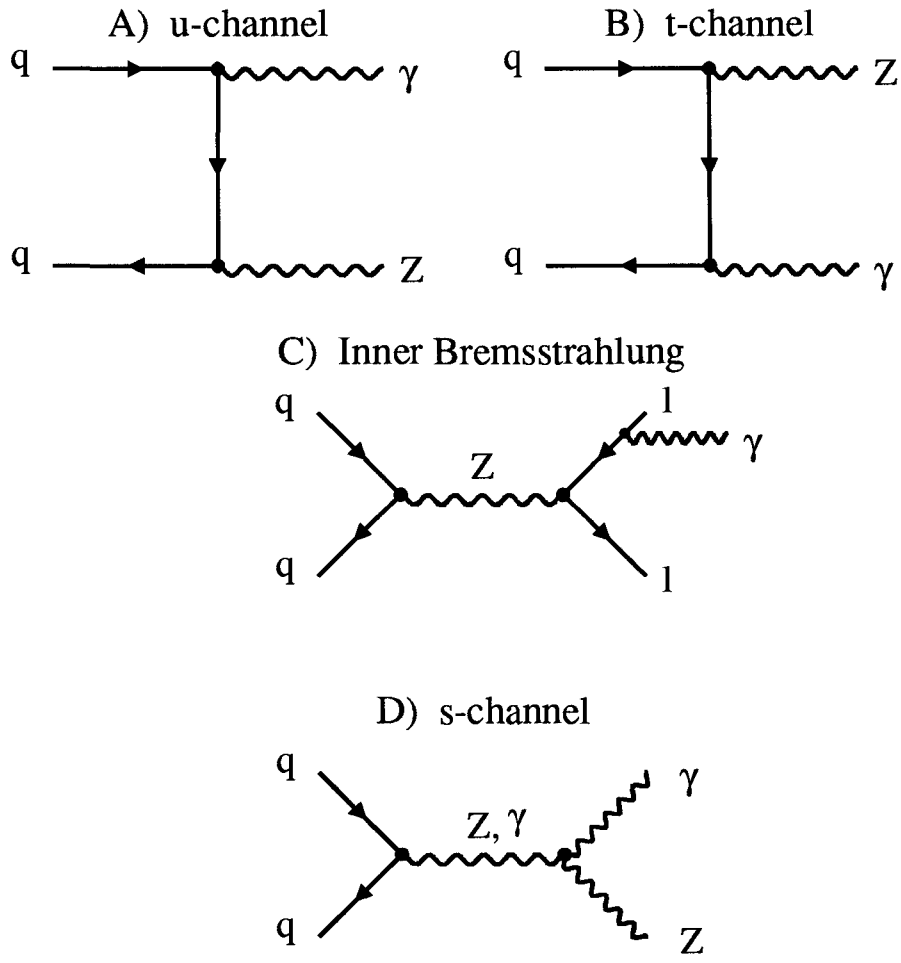


**Figure 2.5**: Feynman diagrams for $Z\gamma$ production. Figure d is the non-Standard Model diagram which requires anomalous couplings between the $Z$ and photon. This analysis searches for events in which the $Z$ decays into a muon pair.

where $M_Z$ is the $Z$ mass, $P$ and $q_1$ are the incoming and outgoing $Z$ four-momenta (Lorentz indices $\mu$ and $\alpha$, respectively), and $q_2$ is the four-momenta of the outgoing photon, which is on-shell and has a Lorentz index of $\beta$. The variables $h_i^Z$, where $i = 1-4$, are form factors. Note that the same helicity arguments hold for $Z\gamma$ processes as in $W\gamma$ processes, again which is why four free parameters are needed to describe the anomalous contributions to the $ZZ\gamma$ and $Z\gamma\gamma$ vertices at tree level ($Z$ bosons have a spin of $J = 1$). The vertex function for $Z\gamma\gamma$ processes can be written by making the substitutions

$$\frac{P^2 - q_1^2}{M_Z^2} \rightarrow \frac{q_2^2}{M_Z^2} \tag{2.12}$$

and

$$h_i^Z \rightarrow h_i^\gamma \tag{2.13}$$

in Equation 2.10.

The form factors $h_i^V$ $(V = Z, \gamma; i = 1 - 4)$ are, as is the case with $W\gamma$ form factors, dimensionless functions of $q_1^2, q_2^2$ and $P^2$, and they are expected to take the generalized dipole form

$$h_i^V(P^2 = \hat{s}, q_1^2 = M_Z^2, q_2^2 = 0) = \frac{h_{i0}^V}{(1 + \hat{s}/\Lambda_Z^2)^n} \tag{2.14}$$

The form factor scale $\Lambda_Z$ is analogous to the $W$ form factor scale $\Lambda_W$, and is expected to be on order of at least a few hundred $GeV$. This scale determines the energy regime where the $Z$ no longer appears point-like. In order to preserve unitarity at all energies, exponent values of $n = 3$ for $h_{1,3}^V$ and $n = 4$ for $h_{2,4}^V$ are chosen [11]. Figures 2.6a-d illustrate what

happens to the cross section of both $W\gamma$ and $Z\gamma$ processes when the anomalous couplings and form factor scales are non-zero, i.e. are at non-SM values. For $W\gamma$ two cases are shown; one with $\Delta\kappa = 3, \lambda = 0$ and another with $\Delta\kappa = 0, \lambda = 2$. Figures 2.6a,c show how the cross section varies for these anomalous couplings as a function of the form factor scale. For $Z\gamma$, two cases with $h_{30} = 0.9, h_{40} = 0$ and $h_{30} = 0, h_{40} = 7.5$ are shown as the $Z$ form factor scale varies (Figures 2.5b,d). For all four figures, the value at $\Lambda_{W,Z} = 0$ gives the SM value of the cross section times branching ratio. The cross section increases rapidly at lower values of the form factor scale, and then gradually evens off to almost a constant value.

From the symmetry properties of the $ZZ\gamma/Z\gamma\gamma$ vertex function all terms are $C$-odd, while terms with $h_1$ or $h_2$ are $P$-even ($CP$-violating) and terms with $h_3$ or $h_4$ are $P$-odd ($CP$-conserving). In the SM all of the form factors $h_{i0}^V$ vanish at tree-level. However, at the one-loop level any $CP$-conserving couplings, such as $h_{30}^V$ and $h_{40}^V$, are non-zero, whereas $CP$-violating couplings are zero. This is because in order to generate these couplings at the one-loop level it is necessary to involve the $CP$-violating phase in the quark mixing matrix. This is not possible with one-loop corrections, but would be possible at the 2- or 3-loop level [12]. These values, though, are expected to be quite small (on order of $10^{-4}$), whereas if the couplings are large one would conclude that the $Z$ is a composite particle.

In principle, the electric dipole and magnetic quadrupole *transition* moments of the $Z$ boson, $d_{Z_T}$ and $Q_{Z_T}^m$, respectively, are related in the static limit (photon energy $k \to 0$) to combinations of the $h_{30}^Z$ and $h_{40}^Z$ anomalous couplings. The $CP$-violating couplings $h_{10}^Z$

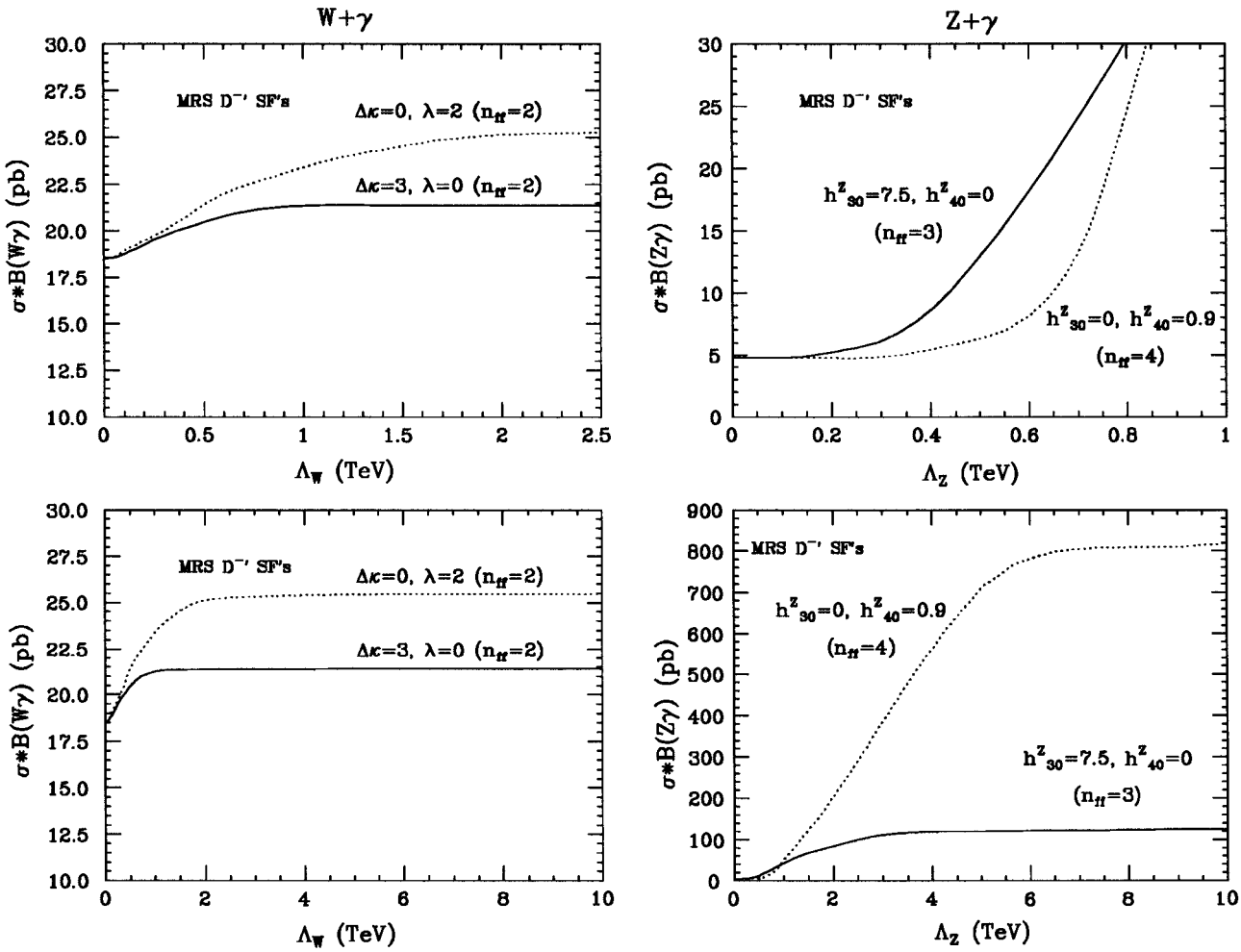


**Figure 2.6**: Figures show how the cross sections for $W+\gamma$ and $Z+\gamma$ vary, for non-zero values of anomalous couplings, as a function of form factor scale. Figures (a) and (b) show the behavior at lower values of the form factor scales, while Figures (c) and (d) show the overall behavior.

and $h_{20}^Z$ are related in a similar fashion to the magnetic dipole and electric quadrupole transition moments of the $Z$ ($\mu_{Z_T}$ and $Q^e_{Z_T}$). The expressions for the $Z$ transition moments are given by [13] (with $\hbar = c = 1$)

$$d_{Z_T} = \frac{e}{M_Z}\frac{1}{\sqrt{2}}\frac{k^2}{M_Z^2}(h_{30}^Z - h_{40}^Z) \tag{2.15}$$

$$Q^m_{Z_T} = \frac{e}{M_Z^2}\sqrt{10}(2h_{30}^Z) \tag{2.16}$$

$$\mu_{Z_T} = 1\frac{e}{M_Z}\frac{1}{\sqrt{2}}\frac{k^2}{M_Z^2}(h_{10}^Z - h_{20}^Z) \tag{2.17}$$

$$Q^e_{Z_T} = \frac{e}{M_Z^2}\sqrt{10}(2h_{10}^Z) \tag{2.18}$$

There is no analog of a charge radius for the $Z$ because the $Z$ has no static electromagnetic multipole moments. The transition moments for the $Z$ boson are analogous to the E1 and M2 transitions of hydrogen in standard quantum mechanics.

In $W\gamma$ processes interference between various Feynman diagrams results in a radiation zero. This is not expected to be observed in SM $Z\gamma$ processes because there is no $s$-channel $Z$-photon coupling at tree level to interfere with the $u$- and $t$-channel diagrams. The ratio of $W\gamma$ to $Z\gamma$ cross section times branching ratios is calculated in the SM to be about 4 [45]. This can be compared to the ratio of inclusive $W$ to inclusive $Z$ cross section times branching ratios, which is around 10.9 in the SM. The difference between the two ratios relates directly to the interference in the $W\gamma$ channel; the total $W\gamma$ cross section is reduced because several diagrams interfere with each other destructively. The cross section ratios provide a sensitive test of the SM [45] because any common

uncertainties, efficiencies and acceptances of the two cross sections cancel, and the ratios are well-predicted by the SM.

## 2.3 Unitarity Constraints for $W\gamma$ and $Z\gamma$ Processes

In the sections above, it was mentioned that unitarity preservation was a concern when dealing with the form factors which would describe compositeness of the $W$ and/or $Z$ bosons. The concept of unitarity and compositeness scales will be discussed in this section. It should be mentioned that the idea of unitarity refers essentially to the conservation of probability. For example, from ordinary quantum mechanics one can carry out a sum of partial waves to calculate the cross section for a given tree-level process. The result would have a maximum value, $\sigma_{max}$. One could then use the methods of quantum field theory (such as Feynman diagrams and the corresponding rules) to calculate the cross section of the same process. That result would have the constraint that the cross section cannot exceed $\sigma_{max}$. That would be referred to as a unitarity constraint. Reference [1] has an example of such calculations.

### 2.3.1 $W\gamma$ Unitarity Constraints

Restrictions can be placed on the reduced amplitudes for $W\gamma$ processes, $A^W_{\beta_W\beta_\gamma}$, through the use of partial wave unitarity. The restrictions can be written in terms of the anomalous couplings. For the case of $\Delta\kappa$ and $\lambda$, two such unitarity restrictions arise: i) one

associated with $W+\gamma$ production and, ii) one associated with $W^+W^-$ production. For $W+\gamma$ production the unitarity restriction is [4, 13]

$$\sum_{\beta_W \beta_\gamma} |A^W_{\beta_W \beta_\gamma}|^2 < \frac{3\sin^2\theta_W}{\alpha^2(1-\frac{M_W^2}{\hat{s}})} \tag{2.19}$$

where, again, $\beta_W$ and $\beta_\gamma$ are the helicities of the $W$ and photon, $\theta_W$ is the weak mixing angle and $\alpha(q^2) = 1/128$ is the fine structure constant at $q^2 = M_Z^2$ [15]. For an assumed dipole form factor, with an exponent of $n = 2$ as shown above, unitarity would be violated if

$$\frac{\frac{\hat{s}}{M_W^2}-1}{(1+\frac{\hat{s}}{\Lambda_W^2})^4}[(\Delta\kappa+\lambda)^2 + (\frac{\hat{s}}{M_W^2})(\Delta\kappa(\frac{M_W^2}{\hat{s}})+\lambda)^2] \geq \frac{6\sin^2\theta_W}{\alpha^2} \tag{2.20}$$

over the range $M_W < \sqrt{\hat{s}} < 1.8\ TeV$.

For $W^+W^-$ production, the unitarity restriction is [4, 13]

$$\sum_{\beta_{W^+}\beta_{W^-}} |A^W_{\beta_{W^+}\beta_{W^-}}|^2 < \frac{3(3-6\sin^2\theta_W+8\sin^4\theta_W)}{5\alpha^2(1-\frac{4M_W^2}{\hat{s}})^{\frac{3}{2}}} \tag{2.21}$$

The terms $\beta_{W^\pm}$ are the helicities of the $W^\pm$ boson. If a dipole form factor is used then unitarity would be violated in $W^+W^-$ production if

$$\frac{(1-\frac{4M_W^2}{\hat{s}})^{3/2}}{(1+\frac{\hat{s}}{\Lambda_W^2})^4}[(\frac{\hat{s}}{M_W^2}(\Delta\kappa+\lambda)^2+\frac{1}{2}(\frac{\hat{s}}{M_W^2})^2\lambda^2$$
$$+\frac{1}{4}(\frac{\hat{s}}{M_W^2})^2\Delta\kappa^2] \geq \frac{3(3-6\sin^2\theta_W+8\sin^4\theta_W)}{5\alpha^2} \tag{2.22}$$

over the range $2M_W < \sqrt{\hat{s}} < 1.8\ TeV$.

If one makes the assumption that only one coupling is non-zero at a time, then, in the limit $\Lambda_W >> M_W$ and for the assumed dipole form factor and exponent $n = 2$, the unitarity limits are [14]

$$W\gamma: \quad |\Delta\kappa| < \frac{37.1\ TeV}{\Lambda_W} \quad (\lambda = 0)$$
$$|\lambda| < \frac{3.9\ TeV^2}{\Lambda_W^2} \quad (\Delta\kappa = 0)$$

$$W^+W^-: \ |\Delta\kappa| < \frac{7.3\ TeV^2}{\Lambda_W^2} \quad (\lambda = 0)$$
$$|\lambda| < \frac{5.3\ TeV^2}{\Lambda_W^2} \quad (\Delta\kappa = 0)$$

### 2.3.2 $Z\gamma$ Unitarity Constraints

For $ZZ\gamma$ processes, partial wave unitarity leads to the following bound on the reduced amplitude [11]:

$$(\sum_{\beta_Z\beta_\gamma} |A^Z_{\beta_Z\beta_\gamma}|^2)^{1/2} \leq \frac{1}{\alpha}\sqrt{\frac{3}{10}}4\sin\theta_W\cos\theta_W \tag{2.23}$$

where again $\theta_W$ is the weak mixing angle, $\beta_{Z,\gamma}$ are the helicities of the $Z$ and photon, respectively, and $\alpha$ is the fine structure constant. For $Z\gamma\gamma$ processes:

$$(\sum_{\beta_Z\beta_\gamma} |A^{\gamma}_{\beta_Z\beta_\gamma}|^2)^{1/2} \leq \frac{1}{\alpha}\frac{3}{5}(3 - 6\sin^2\theta_W + 8\sin^4\theta_W)^{1/2} \tag{2.24}$$

If one makes the assumption that only one anomalous coupling is non-zero at a time, then, in the limit $\Lambda_Z >> M_Z$ ($\Lambda_Z$ is the $Z$ form factor scale),

$$|h^Z_{10}|, |h^Z_{30}| < \frac{1.00\ TeV^3}{\Lambda_Z^3} \quad (n = 3) \tag{2.25}$$

$$|h^Z_{20}|, |h^Z_{40}| < \frac{0.030\ TeV^5}{\Lambda_Z^5} \quad (n = 4) \tag{2.26}$$

and

$$|h^\gamma_{10}|, |h^\gamma_{30}| < \frac{1.20\ TeV^3}{\Lambda_Z^3} \quad (n = 3) \tag{2.27}$$

$$|h^\gamma_{20}|, |h^\gamma_{40}| < \frac{0.036\ TeV^5}{\Lambda_Z^5} \quad (n = 4) \tag{2.28}$$

In these expressions it was assumed that the form factor exponent had the values of $n = 3$ for $h^V_{10}$ and $h^V_{30}$, and $n = 4$ for $h^V_{20}$ and $h^V_{40}$. Also, $\sin^2\theta_W = 0.23$ and $M_Z = 91.2\ GeV/c^2$ were used.

For both the $W\gamma$ and $Z\gamma$ unitarity constraints, the experimental sensitivity to the possible internal structure of the $W$ and $Z$ bosons can be related to the form factor scale via

$$L_V = \frac{\hbar c}{\Lambda_V} \tag{2.29}$$

where $L_V$ is the distance scale and $V = W, Z$. The quantity $\hbar c$ is 197.3 $MeV \cdot fm$.

# Chapter 3

# Experimental Apparatus

## 3.1 The Tevatron

Fermi National Accelerator Laboratory (Fermilab) currently houses the highest energy accelerator in the world. Proton-antiproton ($p\overline{p}$) collisions take place at a center of mass energy of 1.8 TeV. Reaching such high energies is accomplished using a circular accelerator called the Tevatron, which is 4 miles in circumference. Powerful superconducting magnets line the beamline in order to hold the protons and antiprotons in a circular orbit. The CDF detector is located at site B0, one of six interaction regions around the Tevatron.

The method used to produce collisions at Fermilab is extremely complex and includes several smaller particle accelerators which boost the protons and antiprotons to various energy levels before injecting them into the Tevatron. Protons are created from hydrogen gas which is ionized and accelerated to 750 keV by a Cockcroft-Walton electrostatic accelerator. The initial beam of protons from the Cockcroft-Walton accelerator is injected

into a linear accelerator (linac), whose purpose is to boost the proton energy to about 200 MeV. From the linac the proton beam is transferred into the Booster Ring, which accelerates the protons again to 8 GeV. The protons are injected into the Main Ring from the Booster Ring. The Main Ring is the original accelerator at Fermilab, and it now sits on top of the Tevatron in the accelerator tunnel. The Main Ring accelerates the protons from 8 GeV up to 120 GeV, at which time they are injected into the Tevatron in six separate 'bunches'. A 'bunch' is an intense group of many protons ($\sim 10^{12}$ protons) and is about one meter long.

Not all of the protons make it to the Tevatron. A great number of protons are needed to produce the antiprotons, which do not exist naturally on Earth. Protons from the Main Ring are used to strike a stationary tungsten target. The ratio of number of antiprotons produced to number of protons used to produce them is $\sim 10^{-7}$. Antiprotons that are produced at the target are swept off by magnets to the 'Debuncher Ring', which is designed to focus the antiprotons into a beam so they can be tansferred into an accumulator. Antiprotons are stored in the accumulator, which is a small ring, as more antiprotons are produced. The process of producing and storing antiprotons is called 'stacking'. When the antiproton stack reaches some pre-determined current level (on order of $\sim 10^{10}$ antiprotons) six bunches of antiprotons are injected into the Main Ring, in a direction opposite that of the proton bunches. After the antiprotons reach an energy of 120 GeV, they are injected into the Tevatron, and collisions are possible. Proton and antiproton bunches make crossings in the middle of the CDF detector every 3.5 $\mu$s.

## 3.2 CDF Detector

The Collider Detector at Fermilab (CDF) [16] is a 5000 ton detector which is located at one of six interaction regions of the Tevatron. Those subsystems of the detector which are relevant to this analysis are described in this section: The tracking system, the calorimeters and the muon system. These include several detector components which were new for the 1992-93 data taking run (Run 1A). These are, a silicon vertex detector (SVX), a new vertex time projection chamber (VTX) and new muon detectors (CMP, CMX).

The coordinate system used at CDF is a right-handed system in which the $z$ direction is in the direction of the proton beam. The $x$ and $y$ coordinates are then transverse to the beam, with the $y$ axis pointing vertically upward and the $x$ axis pointing radially outward from the beamline. The usual polar angle $\theta$ and the azimuthal angle $\phi$ are used (See Figure 3.1). It is more common to use pseudorapidity, $\eta = -\ln\tan(\theta/2)$, rather than $\theta$ because at relativistic energies differences in this variable are approximately Lorentz invariant.

### 3.2.1 Tracking

The tracking system is closest to the interaction region and is contained within the volume of a superconducting solenoid. The solenoid is 1.5 meters in radius, and the magnetic field is 1.4 Tesla and is oriented along the beam line in the proton direction. The tracking

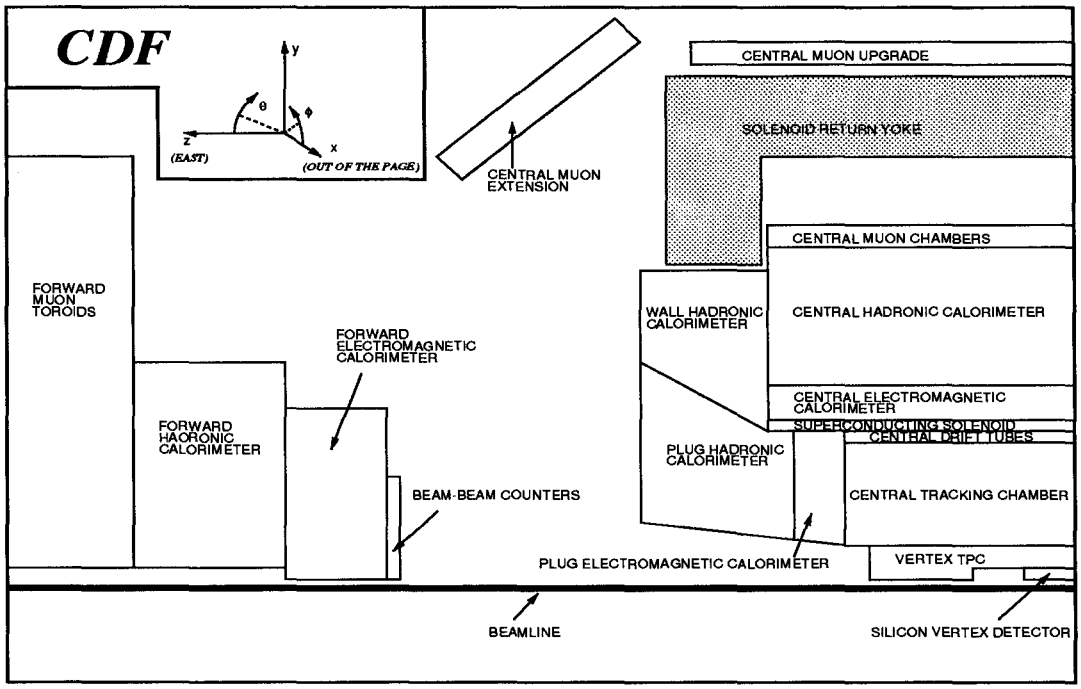


**Figure 3.1**: One quadrant of the CDF detector.

detectors, as well as the muon detectors, use a gas mixture of 50% Argon-50% Ethane to detect charged particles which result from the $p\overline{p}$ collisions.

The SVX is the innermost detector and provides high precision vertex information in $r - \phi$ with a measured single hit resolution of $\sigma = 11\ \mu m$ [17]. The SVX is 51 cm long and covers the range $|\eta| < 2.8$. A vertex time projection chamber (VTX) lies just outside the SVX. The VTX provides tracking information up to a radius of 22 cm and within a region defined by $|\eta| < 3.2$, and determines where the interaction occurs along the $z$-axis. The VTX resolution along the $z$ axis is about 1 mm. The SVX and VTX are mounted within the central tracking chamber (CTC) [18].

The CTC is a 3.2 m long cylinder and has an outer radius of 132 cm. The CTC consists of 84 layers of sense wires of which 24 are tilted at $\pm 3°$ with respect to the beam

direction for tracking in the $r - z$ plane. All wire cells are inclined at 45° relative to the radial direction from the beam axis to compensate for the drifting of electric charges in the magnetic field. The net drift velocity of charged particles in electromagnetic fields forms an angle relative to the electric field given by

$$\tan \beta = \frac{v \cdot B}{k \cdot E} \tag{3.1}$$

where $\beta$ is the Lorentz angle, $E$ and $B$ are the electric and magnetic field strengths, respectively, $v$ is the drift velocity with no magnetic field, and $k$ is a parameter which depends on the gas being used. For 50%-50% mixtures of Argon-Ethane $k$ is approximately 0.7. The electric field strength is chosen such that the Lorentz angle is about 45°. Tilting the wires results in drift trajectories which are approximately azimuthal. This helps simplify track reconstruction.

Charged particles which are produced in collisions and traverse the tracking region have their tracks reconstructed and, due to the curvature of the tracks caused by the magnetic field, their momenta measured by the CTC. The momentum resolution of the CTC is $\frac{\delta P_T}{P_T} = 0.0020 \times P_T$ for isolated tracks, where $P_T$ is the momentum transverse to the beam and is measured in $GeV/c$. If the tracks are constrained to originate from the interaction vertex, the momentum resolution is improved to $\frac{\delta P_T}{P_T} = 0.0008 \times P_T$. Tracks placed under this constraint are called "beam-constrained" tracks. The region where tracking is fully efficient is $-1.1 < \eta < 1.1$ ($40° < \theta < 140°$). The tracking efficiency as a function of $\eta$ for Run 1A is shown in Figure 3.2 [19].

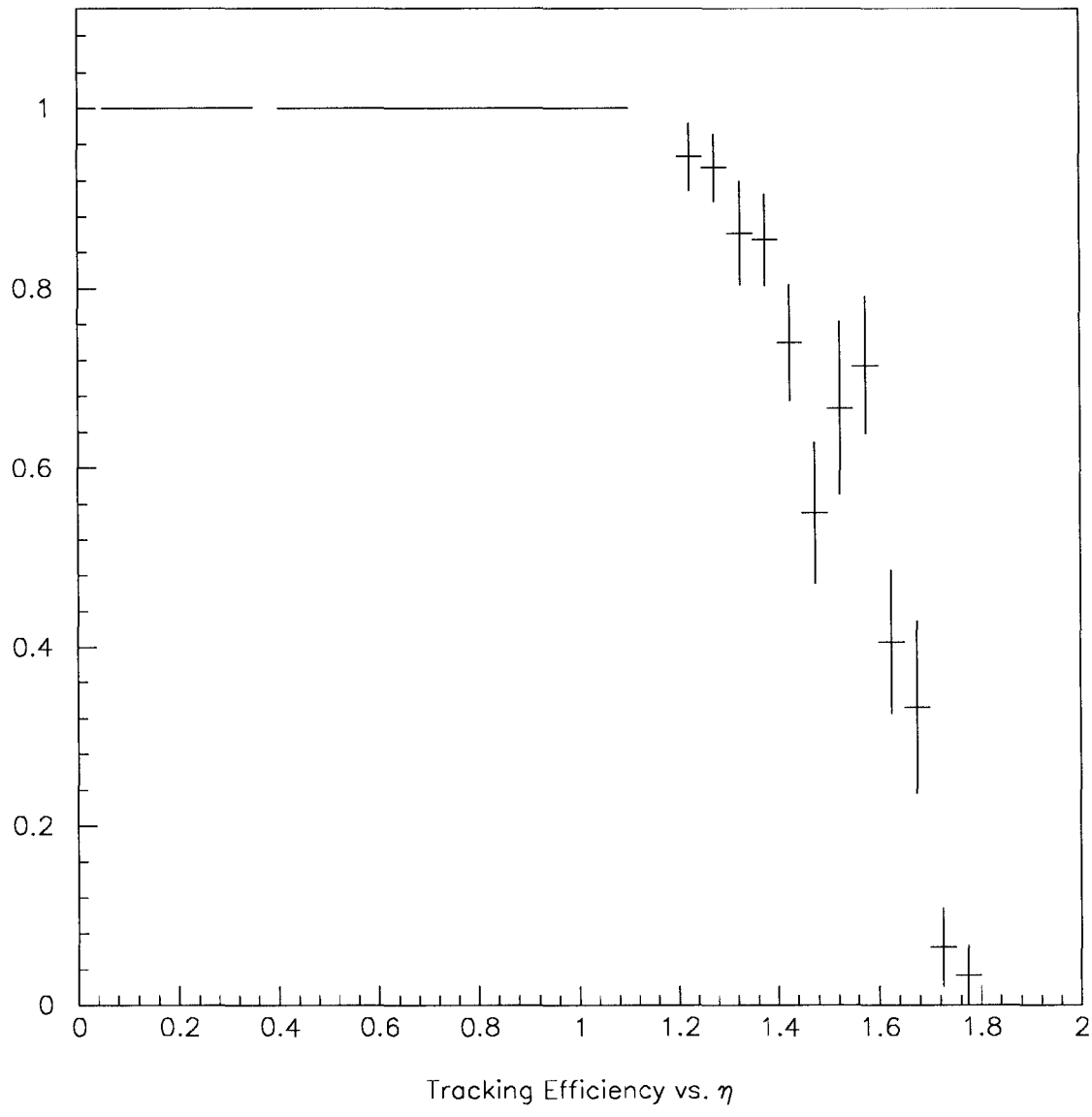


**Figure 3.2**: CTC tracking efficiency as a function of $\eta$.

The central drift tubes (CDT) are outside the CTC and provide additional tracking in $r - \phi$ and $z$ [20].

### 3.2.2 Calorimeters

Surrounding the tracking system, outside the magnet, is the calorimeter. The calorimeter is used to determine the energy of particles produced in the $p\bar{p}$ collisions. The calorimeters cover $2\pi$ in $\phi$ and are broken up into 3 main regions in terms of $\eta$: the central region ($|\eta| < 1.1$), the plug region ($1.1 < |\eta| < 2.4$), and the forward region ($2.2 < |\eta| < 4.2$). These separate regions are referred to as the CEM(CHA), PEM(PHA) and FEM(FHA) for electromagnetic (hadronic) calorimeters. The calorimeters are organized in projective towers which point back to the nominal interaction region and have fine segmentation in $\eta - \phi$ space. The central calorimeters are scintillator based, and the central towers are 15° wide in $\phi$ and 0.1 units wide in $\eta$. The electromagnetic calorimeter [21] absorber is lead, and the CEM energy resolution is $\frac{\delta E}{E} = \frac{13.5\%}{\sqrt{E_T}} \oplus 1.2\%$ [22], where $E$ is the total energy and $E_T$ is the transverse energy, defined as $E_T \equiv E \sin\theta$ ($\theta$ is the polar angle). Both energies are in $GeV$. The term "$\oplus$1.2%" signifies that a constant term is added in quadrature in the resolution. This term arises from finite statistics used to calibrate the calorimeter. The hadronic calorimeter absorber is iron, and the CHA energy resolution is $\frac{\delta E}{E} = \frac{75\%}{\sqrt{E}} \oplus 3\%$ for isolated pions [23].

Located 6.3 radiation lengths into the CEM (approximately at shower maximum for electromagnetic showers) are central proportional chambers (CES) with both strip and wire readout [24]. The CES is used for the determination of transverse shower

development, and it provides the precise location of electromagnetic showers. The rms accuracy of the CES is $\sim$ 3 mm in $R - z$ and $\sim$ 1.7 mm in $R - \phi$. Figure 3.3 shows a CEM calorimeter wedge and Figure 3.4 shows the orientation of the anode wires and cathode strips in the CES.

In this analysis the central calorimeters are used to help identify photons, which are characterized by mostly electromagnetic energy 'clusters' in the calorimeters. A 'cluster' is defined as an energy deposit which is contained within some number of calorimeter towers. The tower with the highest $E_T$, called the seed tower, must be above some threshold (typically 3 $GeV$), and the sum of the $E_T$ of the seed tower and adjacent towers then must be above some higher threshold, typically 5 $GeV$. Appendix B discusses the calorimeter clustering algorithm in more detail. Muons are characterized by depositing very little energy in the calorimeters (minimum ionizing particles). The CES was used in identifying photons and separating single photons from multi-photon backgrounds, such as $\pi^0$ decays.

### 3.2.3 Muon Detection

Muon detectors are furthest out from the interaction region. The muon detectors used in this analysis are the central muon chambers (CMU) [25] , which overlay the calorimeter wedges, and the central muon upgrade chambers (CMP) [26], which form a nearly continuous box in $\phi$ surrounding the detector. The CMP was a new addition to CDF for Run 1A and has the added benefit of extra steel between the chambers and the interaction region, which results in better muon identification (the extra steel helped to ensure only

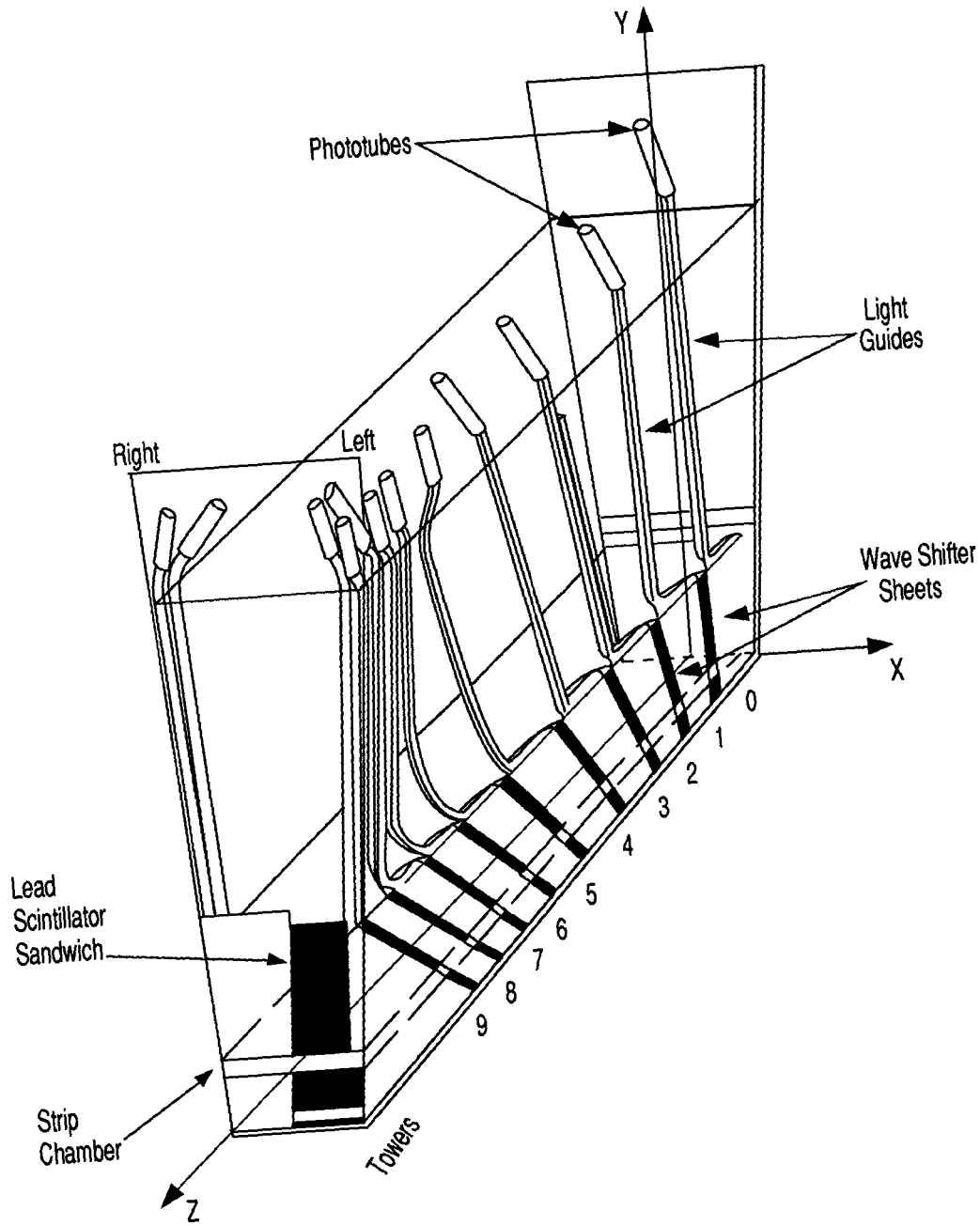


**Figure 3.3**: Schematic of CEM calorimeter wedge.

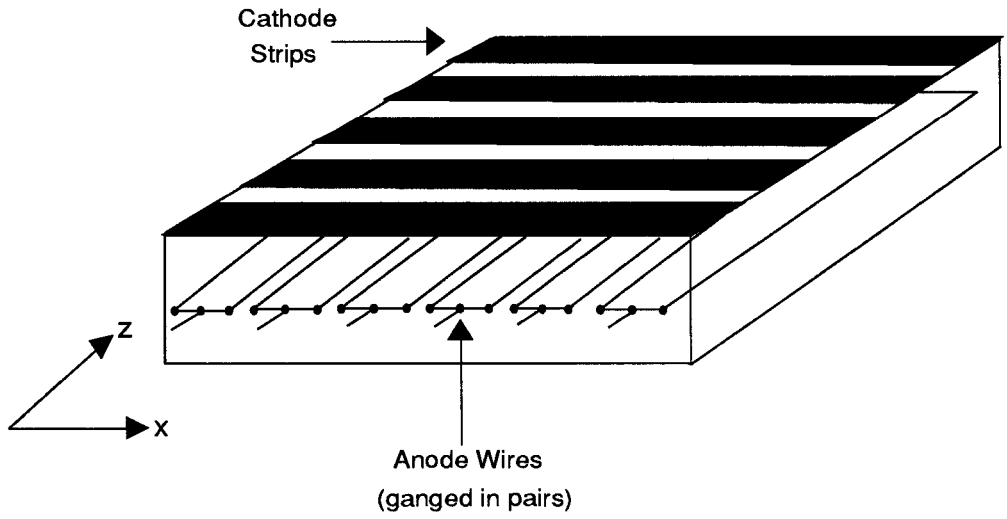


**Figure 3.4**: Schematic of CES wires and strips.

muons get to the CMP and not hadronic 'punchthrough'). The CMP is used to confirm CMU hits in regions where both provide coverage. The coverage provided by the CMU and CMP extends out to 0.6 in $|\eta|$. The central muon extension (CMX) [27] was also added for Run 1A but is not used in this analysis. The CMX extends coverage from $0.6 < |\eta| < 1.0$.

The CMU detector makes up the original muon system at CDF. These drift cells are 3470 mm from the beam line and use a 50%-50% mixture of argon-ethane gas with a small trace (roughly 0.7%) of isopropyl alcohol. The calorimeters provide about 5 hadronic interaction lengths of material between the CMU and the interaction region, and act as an absorber of hadrons which can be mistaken as muons. Muons with $P_T$ above 1.5 $GeV/c$ can reach the CMU. Muons with energy lower than that cannot pass through the calorimeters because they would lose all of their energy through ionization.

Only 12.6° of each central wedge is actually covered by the chambers, leaving a 2.4° gap between adjacent wedges. Groups of 4 cells are glued together to form CMU chambers, and three chambers are placed in each wedge. Figure 3.5 shows a schematic of how CMU chambers are organized within a central stack.

The CMP consists of long aluminum extrusions (about 6.4 m long) which sit behind an extra 60 cm of steel. Each extrusion has a single wire strung in it. The CMP is comprised of stacks of 4 extrusions (a total of 4 wires) which are glued together in a staggered manner. There are holes in $\phi$ where no supporting structures existed to put additional stacks. In all, about 13% of the possible $\phi$ coverage is lost. The single hit tracking resolution of the CMP chambers is approximately 250 $\mu$m and the average drift velocity is 43 $\mu$m/ns. Multi-hit TDCs are used to readout drift timing information. Appendix A discusses the CMP chambers and electronics in greater detail. Figure 3.6 summarizes how muons are observed from the CDF detector standpoint.

### 3.2.4 Determination of the Luminosity

If one has hopes of measuring a cross section at CDF the integrated luminosity needs to be measured. The integrated luminosity for data collected during the collider run was determined using the beam-beam counters (BBC's). The BBC's consist of two planes of scintillation counters covering a range in $\eta$ of $3.2 < |\eta| < 5.9$ (0.32° to 4.47° in the forward and backward directions) [16]. The number of forward-backward coincidences in the BBC's, divided by the effective cross section of the counters, gives the integrated luminosity. The effective cross section of the BBC's was measured to be $51.1 \pm 1.7$ *mb*.

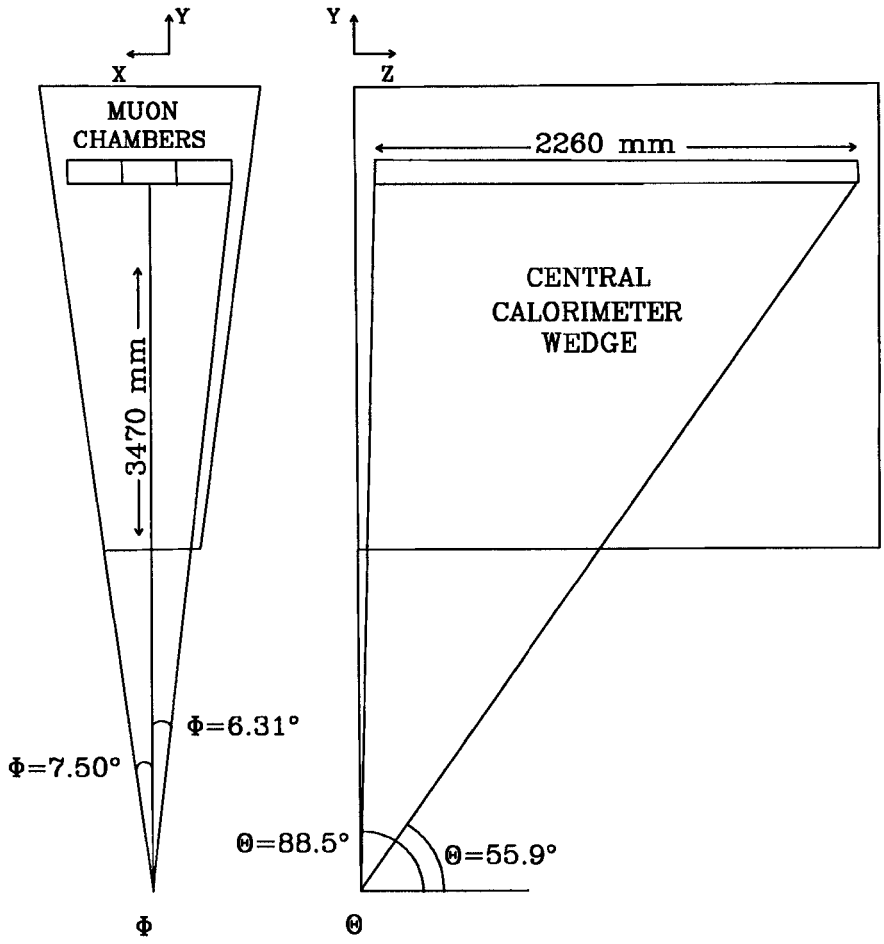


**Figure 3.5**: Schematic of CMU chambers in a central wedge.

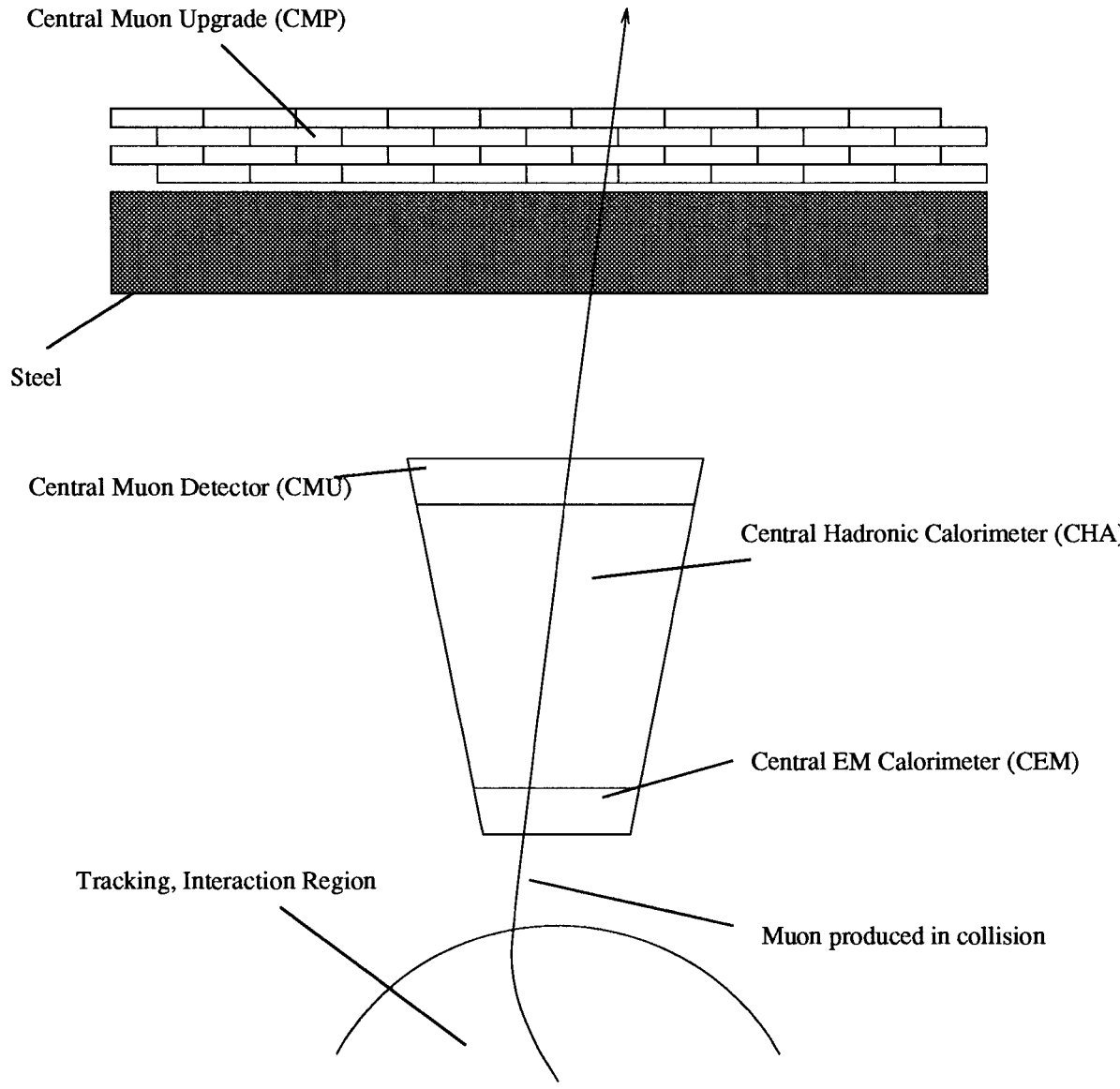


**Figure 3.6**: Muon detection using the CDF detector. A muon from a collision bends in the magnetic field in the tracking chambers, passes through the calorimeters and is detected by the CMU and/or CMP.

The average luminosity per data-taking run was around $3 \times 10^{30}$ cm$^{-2}$sec$^{-1}$. The total integrated luminosity written to tape for Run 1A was $19.3 \pm 0.7$ $pb^{-1}$. The high-$P_T$ muon sample, after removing data runs in which muon data was considered to be bad, had a total integrated luminosity of $18.6 \pm 0.7$ $pb^{-1}$.

### 3.2.5 Trigger System

The interaction rate during Run 1A was on the order of $10^5$ times higher than the capacity of the CDF data acquisition system. A trigger system consisting of three levels was used to select interesting events which were to be written to magnetic tape for further processing and analysis. In addition, the trigger system maximizes the amount of time that the CDF detector actually takes data (or, equivalently, minimizes detector 'dead-time'). Each trigger level was a logical OR of a number of triggers designed to select events with electrons, muons, or jets. Below is a brief description of the trigger system hardware and software.

The first trigger level, level 1, uses direct outputs from the calorimeters, CTC, and CMU, CMP and CMX detectors. A level 1 decision is based on global features of calorimeter energy deposition, overall energy balance and the presence of tracks in the muon chambers. Information from any of the above detectors can be used to make a level 1 decision. If, for a given $p\overline{p}$ collision, there is a no level 1 trigger accept, the front-end electronics are reset for taking data before the next beam crossing. If, however, there is a level 1 accept, the electronics are not reset and the event is passed to level 2. At a luminosity of $5 \times 10^{30}$ cm$^{-2}$sec$^{-1}$, the rate of level 1 triggers is $\sim 1$ kHz.

The level 2 trigger decides if the detector should be read out for the event which passed level 1. Level 2 does this based on the event topology, which means the requirements the event has to meet are more stringent than at level 1. At level 2, reconstructed tracks in the CTC which are matched to hits in the muon chambers are candidates for muons. Similarly, electron candidates are identified as electromagnetic energy clusters, contained in at most two calorimeter towers, which have single reconstructed tracks in the CTC associated with them. Jet candidates are identified as a set of contiguous calorimeter towers, each with transverse energy above a threshold. The transverse energy of the jet is defined as the sum of the transverse energies of the calorimeter towers in the jet. The transverse energy balance in the detector is done at level 2. This is accomplished using the vector sum of transverse energy in all calorimeter towers $i$, $\mathbf{E_T} = \sum_i E_{T_i} \cdot \hat{\mathbf{n}}_i$. Here, $\hat{\mathbf{n}}$ is a unit vector pointing from the interaction vertex to the calorimeter tower. Because of momentum conservation $\mathbf{E_T}$ should be zero. However, certain events are selected if there is an energy imbalance, which can occur, for instance, if neutrinos are present. Such an energy imbalance is referred to as "missing $E_T$", $\not\!\!E_T$.

The tracking information at level 2 comes from the central fast tracker (CFT), which is a hardware track processor that uses fast timing information from the CTC. The CFT provides lists of tracks in $R-\phi$ space and has a momentum resolution of $\frac{\delta P_T}{P_T} = 0.035 \times P_T$. The CFT efficiency for finding tracks with $P_T$ above 10 $GeV/c$ is 93.5 $\pm$ 0.3 %.

The level 2 trigger decision takes about 20 $\mu$s. If there is a level 2 accept, the detector is readout, and this takes an additional 3-5 ms. The total level 2 output rate is $\sim$ 15 Hz at a luminosity of $5 \times 10^{30}$ cm$^{-2}$sec$^{-1}$.

Data is written to a single magnetic tape at a rate of about 1-2 Hz, so a third trigger level is needed to bring the overall level 2 rate down to this value. The level 3 trigger system consists of a farm of commercial Silicon Graphics multi-CPU Power Servers which have a combined processing power of approximately 1 billion instructions per second. A high bandwidth VME interface allows the input event rate to be as high as 20 Hz, which matches the level 2 output rate. FORTRAN reconstruction computer programs are run at level 3 in order to make further cuts on the accepted level 2 triggers. The execution time, which is typically about 1.5 seconds, is dominated by tracking reconstruction of CTC data. Events which satisfy level 3 requirements are written to magnetic tape. A total of approximately 7 million events were written to tape for Run 1A. For this analysis, only events which pass the muon trigger, which is described in more detail in Section 4.1.1, are used.

# Chapter 4

# Event Selection

The $W\gamma$ and $Z\gamma$ samples studied for this thesis are subsets of larger, inclusive muon $W$ and $Z$ samples. In turn, the inclusive muon $W$ and $Z$ samples are subsets of an inclusive high $P_T$ muon data sample. The inclusive high $P_T$ muon sample was created by selecting events which passed a three level muon trigger. The inclusive $W$ and $Z$ samples were created from those events which were contained in the inclusive high $P_T$ muon sample, but also passed a series of muon quality selection criteria. In addition to the extra muon requirements, $W$ events had a missing energy requirement because the neutrino from the $W$ decay could not be detected, and $Z$ events had to possess two high $P_T$ muon candidates which formed an invariant mass close to the $Z$ mass of 91.1 $GeV/c^2$. Muon $W\gamma$ and $Z\gamma$ samples were selected from the inclusive $W$ and $Z$ samples, respectively. These events had to have a hard, well-isolated photon candidate in the event. This chapter describes the selection criteria of the $Z$ and $W$ samples as well as the photons. The efficiencies of the selection requirements will be discussed in Ch. 5.

## 4.1 Muon Selection

### 4.1.1 Muon Trigger

The purpose of the muon trigger is to select events which possibly have muons in them and then store the information from those events on magnetic tape for future analysis. The muon trigger is a combined 3-level hardware and software trigger in which each succeeding level makes more stringent selection requirements than the previous level. The least stringent muon trigger is called the level 1 muon trigger. An accepted level 1 muon trigger means that there are hits in multiple layers of the CMU or CMX muon detectors (a muon 'stub'), and that those hits are consistent with a muon with a $P_T$ above 6 $GeV/c$. In addition, each CMU tower defines a 'road' which is extended out towards the CMP. In regions where the CMP overlaps the CMU, at least two hits are required in CMP chambers which are in the road, thus providing confirmation of the CMU hits. The use of the CMP reduces the CMU-only trigger rate by a factor of around 15-20 while retaining full efficiency for real muons. The muon $P_T$ used at level 1 is based on differences in timing information from alternating muon cells. For example, a typical muon from the decay of a $W$ has a $P_T$ of more than 20 $GeV/c$. A muon with such high momentum is affected very little when traversing the magnetic field and will pass radially through the CMU. The drift time differences in alternating layers will be essentially zero because these pairs of wires in the CMU chamber are aligned radially (see Fig. 4.1). Lower $P_T$ muons will be affected to a greater extent by the magnetic field, and the track of the muon in the CMU chamber will form an angle with the line formed by the wires.

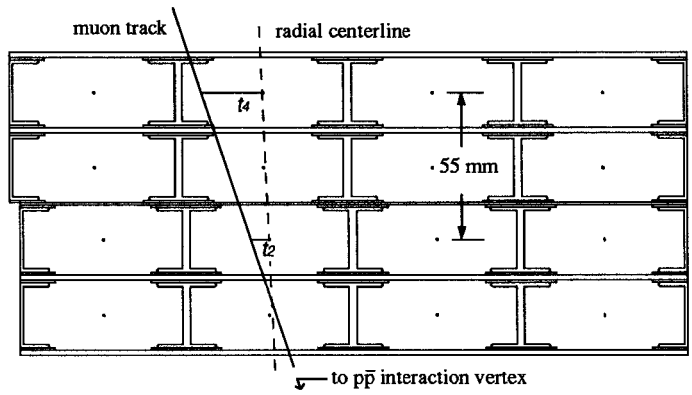


**Figure 4.1**: Cross section cut of CMU chamber. The time differences $|t_3 - t_1|$ or $|t_4 - t_2|$ determine a $P_T$ estimate for the level 1 muon trigger.

From the diagram, the time difference $\Delta t = |t_2 - t_4|$ is a measure of the angle the muon passes through the chamber, and thus can be related to the muon $P_T$. Likewise, the time difference between the other two layers, $\Delta t = |t_1 - t_3|$, which isn't shown on Fig. 4.1, is also a measure of the muon's $P_T$. The trigger uses the $OR$ of these two time differences in order to maintain maximum efficiency. The relationship between the time difference and muon $P_T$ is $P_T = \frac{154}{\Delta t}\ GeV/c$ [28].

If an event passes level 1, more stringent requirements are imposed by the level 2 muon trigger. The level 2 muon trigger requires a track found by the CFT (see Sec. 3.2.5) to be matched to a level 1 muon stub and to be above a certain $P_T$ threshold. The CFT identifies all high $P_T$ tracks above 2.5 $GeV/c$ and presents a list of tracks to the rest of the CDF trigger system. The level 2 muon trigger decodes the list of CFT tracks to predict where in the muon chambers the tracks could hit. This is accomplished using stored look-up tables in special FASTBUS modules. The $\phi$-coordinate is predicted for

| Trigger Level | Efficiency, % | Cross section |
|---|---|---|
| 1 | $94.6^{+1.4}_{-1.8}$ | 55 $\mu$b |
| 2 | $92.3^{+0.9}_{-0.9}$ | 600 nb |
| 3 | $98.6^{+0.8}_{-1.3}$ | 5 nb |
| Combined | $86.1^{+1.7}_{-2.1}$ | — |

**Table 4.1**: Muon trigger efficiencies and cross sections. The combined efficiency is just the product of level 1, 2 and 3 effciencies.

each CFT track, and each track is then matched to muon 'stubs' in the muon chambers. A match in a window of $\Delta\phi = 5°$ surrounding the track must be made in order to accept a track. A level 2 accept is made if a track, which has passed the matching requirement, also has a $P_T$ above 9 $GeV$.

Events which are level 2 accepts are then passed to the level 3 muon trigger. The level 3 muon trigger is a software trigger which, after running the full data reconstruction code online, requires the muon candidate to have a $P_T$ above 18 $GeV/c$ and less than 6 $GeV$ of energy deposited in the hadronic calorimeter tower it traversed. If the muon stub is in the CMU, there is an additional requirement that the difference between the position of the muon stub and the extrapolated track from the CTC in $R-\phi$ is less than 5 cm. The level 3 trigger has a measured efficiency of nearly 99%. Muon candidates which survive the level 3 selection are written to magnetic tape and make up the high-$P_T$ inclusive muon sample. The measured efficiencies and trigger cross sections (for luminosities of around $3 \times 10^{30}$ cm$^{-2}$sec$^{-2}$) for each muon trigger level are summarized in Table 4.1.

### 4.1.2 Muon Quality Selection Cuts

The muon selection for the inclusive $Z$ sample is made offline and requires events from the inclusive high $P_T$ muon sample to have two muon candidates with beam-constrained $P_T$ above 20 $GeV/c$. At least one of the two muons has to pass through the CMU; it can pass through the CMU only or it can pass through the CMU and CMP. The other muon candidate can be anywhere within a region of pseudorapidity $|\eta| < 1.2$, because beyond this $\eta$ range the tracking is inefficient (see Figure 3.2). The second muon is not required to pass through a muon detector.

Tighter requirements are made offline that are designed to take advantage of properties of muons, the most important of which is the minimum ionization characteristic. Muons deposit only a small portion of their total energy in the calorimeters, making them highly penetrating particles in comparison to others. Muon candidates are required to deposit less than 2 $GeV$ of electromagnetic energy and less than 6 $GeV$ of hadronic energy in the calorimeter tower through which they traverse (see Fig. 4.2a,b). The minimum ionization cuts are made on each leg of the $Z$ and are, like all the muon requirements which are discussed below, very efficient for selecting muons (all efficiencies are above 95% and are presented in Ch. 5). In addition, at least one of the muons has to pass the following quality cuts:

- The difference between the position of the extrapolated CTC track and the muon 'stub' in the muon chambers in $R-\phi$ has to be less than 2 cm if the muon stub is in the CMU and less than 5 cm if the stub is in the CMP. This cut is designed to

account for multiple scattering of the muon as it traverses the calorimeter and, for the CMP, the extra steel.

- The excess energy in a cone of $\Delta R = 0.4$ (where $\Delta R \equiv \sqrt{\Delta\phi^2 + \Delta\eta^2}$), defined as the total energy deposited in a cone of $\Delta R = 0.4$ centered on the muon but excluding the muon tower, has to be less than 2 $GeV$. This helps eliminate hadronic punchthrough and high $P_T$ tracks in jets which may be misidentified as muons.

- The impact parameter of the muons with respect to the beamline has to be less than 2 mm. This cut is used to help eliminate cosmic rays from the sample.

- The position of the $z$-vertex for the event has to be within 60 cm of the center of the detector. This cut also helps eliminate cosmic rays.

If at least one of the muon candidates passes *all* of these requirements, a cut is made on the dimuon invariant mass, centered on the $Z$ mass of 91.1 $GeV/c^2$, of $65 < M_{\mu\mu} < 115$ $GeV/c^2$. A total of 507 muon $Z$ candidates survive all selection requirements.

The selection of muon $W$ candidates starts with all events from the inclusive high $P_T$ sample which are not consistent with being $Z$ decays. The muon candidate must satisfy all the selection requirements listed above. Because of the presence of a neutrino in $W$ decays, and because neutrinos do not interact with the detector, a further requirement is made on the missing transverse energy carried off by the neutrino. A cut on missing $E_T$, $\not\!\!E_T$, of at least 20 $GeV$ is made to select $W$ candidates, because the presence of a neutrino creates an imbalance in the distribution of transverse energy in the calorimeters. The missing $E_T$ due to the neutrino (or equivalently, the neutrino $P_T$) is:

$$\not\!\!E_T = \sqrt{p_{\nu_x}^2 + p_{\nu_y}^2} \tag{4.1}$$

where $p_{\nu_x}$ and $p_{\nu_y}$ are defined as

$$p_{\nu_x} = \not\!\!E_{T_x} + (E_T^{cal} \cos\phi_\mu) - p_x^\mu \tag{4.2}$$

$$p_{\nu_y} = \not\!\!E_{T_y} + (E_T^{cal} \sin\phi_\mu) - p_y^\mu \tag{4.3}$$

Here, $p_{\nu_x}$ and $p_{\nu_y}$ are the neutrino's $x$ and $y$ momentum components. The $\not\!\!E_{T_{x,y}}$ are the $x$ and $y$ components of the missing $E_T$ vector, as measured by the calorimeter. The $p_{x,y}^\mu$ are the $x$ and $y$ components of the muon momentum, $E_T^{cal}$ is the energy deposited in the calorimeter by the muon, and $\phi_\mu$ is the muon's position in $\phi$.

A total of 6105 muon $W$ candidates survive all selection criteria, including the missing $E_T$ requirement. Figures 4.2a-d and 4.3a-d show some distributions from the high-$P_T$ inclusive muon sample. Figures 4.2a-d show the energy deposited in the hadronic and electromagnetic calorimeter towers the muon traversed, as well as the muon's impact parameter relative to the beamline, and the $z$ position of the muon in the event relative to the center of the detector. Figures 4.3a-d show the matching variables for the CMU and CMP detectors (the difference in $R-\phi$ between the muon stub and the extrapolated CTC track corresponding to the muon stub), along with the muon pseudorapidity and excess energy in a cone of $\Delta R = 0.4$ centered on the muon. All of these distributions were made from the $W$ sample and are typical of high $P_T$ muons in the CDF detector. Figures

4.4a-c show distributions for the muon $P_T$, the $W$ transverse mass and the missing $E_T$ (or $\nu$ $P_T$) from the inclusive $W$ sample. The $W$ transverse mass is defined as

$$M_W^T \equiv \sqrt{2P_T^\mu P_T^\nu [1 - \cos(\phi^\mu - \phi^\nu)]} \tag{4.4}$$

and is used in place of the $W$ invariant mass because there is no measurement of the neutrino's longitudinal momentum, $p_z^\nu$. Figure 4.4d shows the dimuon invariant mass from the inclusive $Z$ sample.

## 4.2 Photon Selection

The selection of the $W\gamma$ and $Z\gamma$ data samples involves searching the inclusive $W$ and $Z$ samples for events with single, isolated photon candidates. The photon candidates have to pass a separate series of selection criteria. The photon cuts are created based on distributions of testbeam electrons in the central calorimeters, since photons and electrons look nearly the same within the detector (minus a charged track for photons), as well as the effect each cut has on reducing backgrounds (see Ch. 7). The cuts used in this analysis to select photons are:

- A 3 tower cluster of electromagnetic energy deposited in the CEM has to satisfy $E_T \geq 7GeV$ and is required to be in a good fiducial region as determined by its position from CES information.

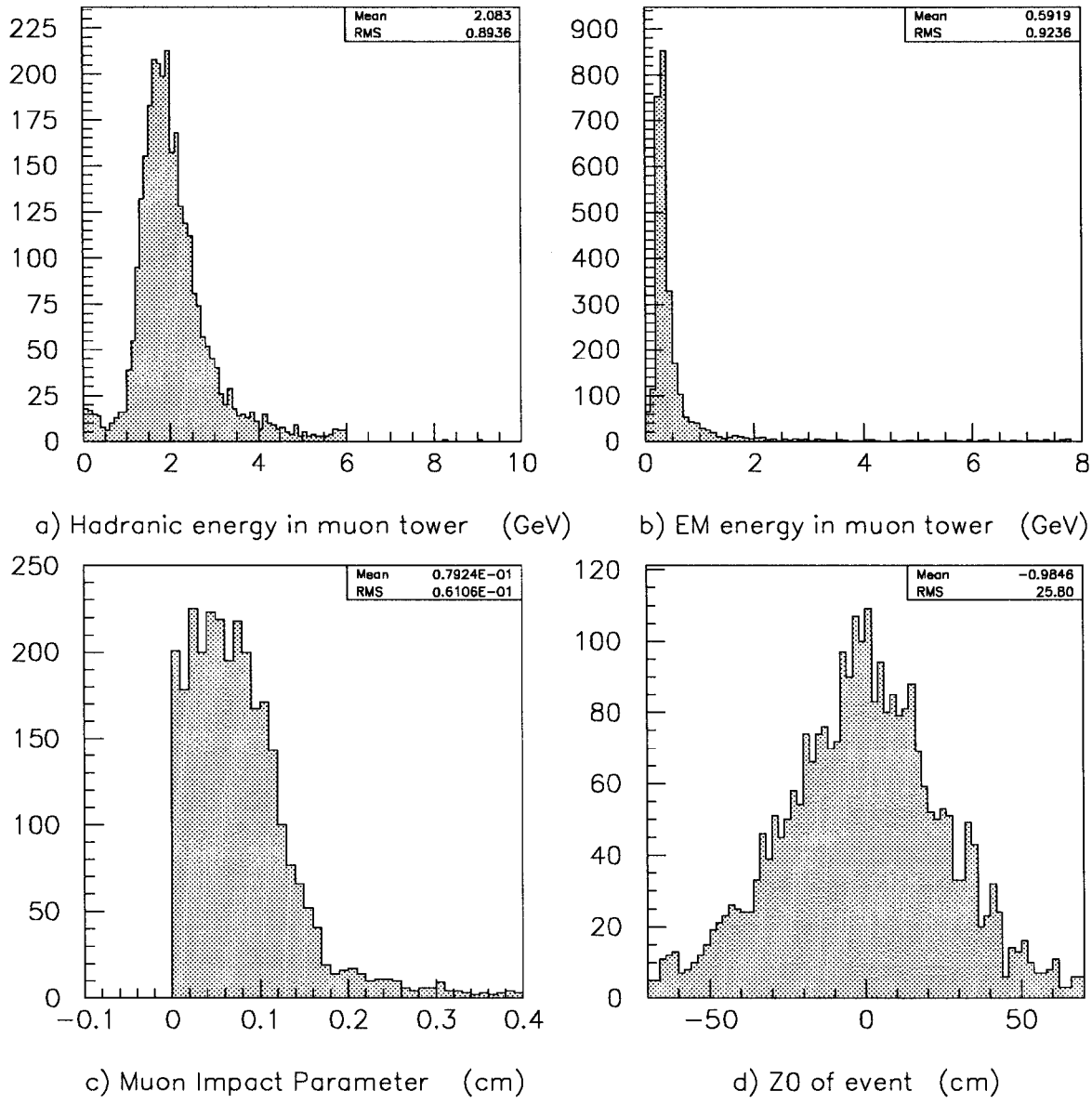


**Figure 4.2**: Muon variables. Figure (a) and (b) show the calorimeter energies in the muon tower. Figures (c) and (d) show the impact parameter and $z$-vertex. These are from the high-$P_T$ muon sample.

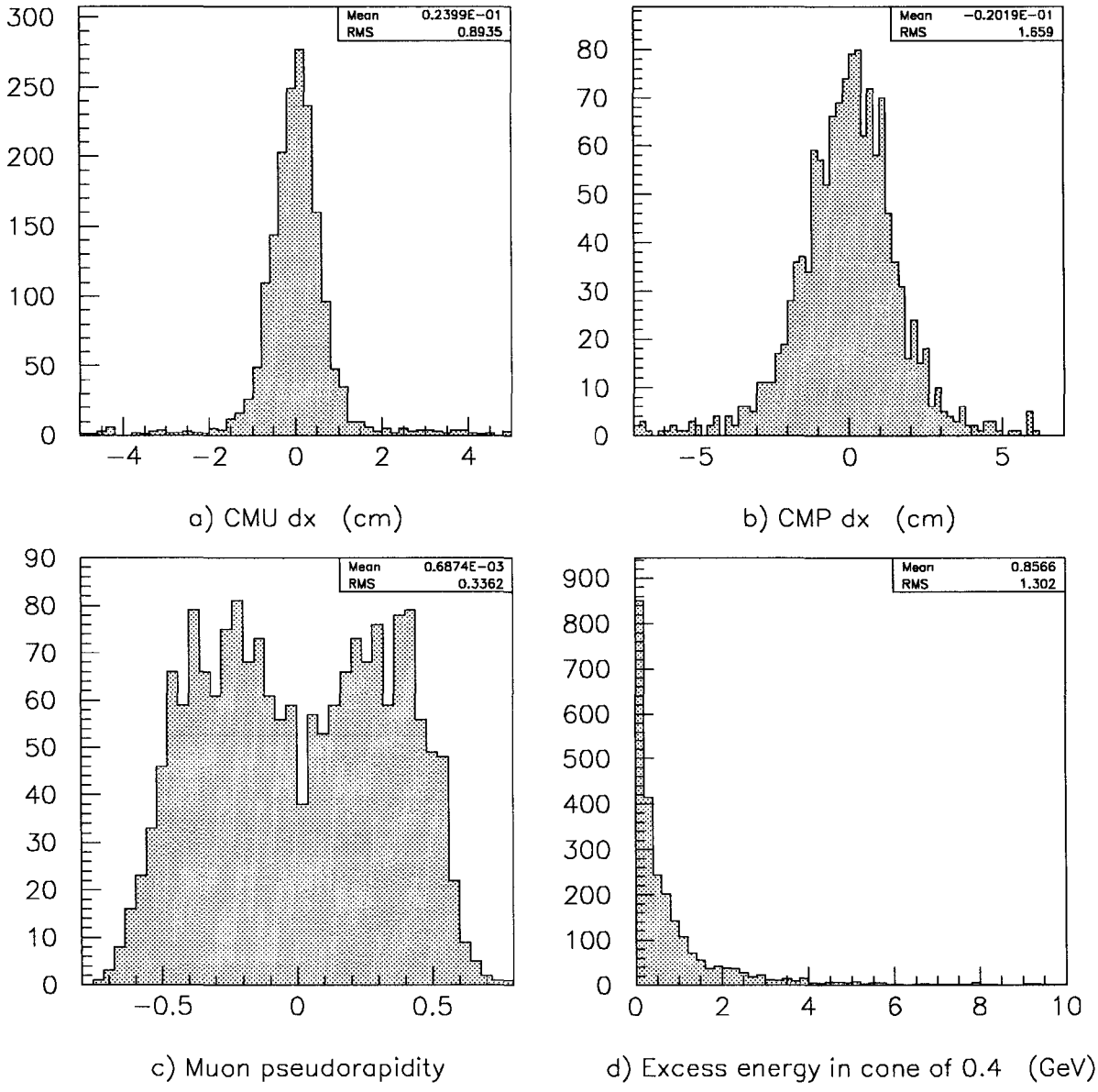


**Figure 4.3**: Muon variables. Figure (a) and (b) show the matching cuts for the CMU and CMP detectors. Figures (c) and (d) show the muon $\eta$ and excess energy in a cone of $\Delta R$ of 0.4 about the muon. These are from the high-$P_T$ muon sample.

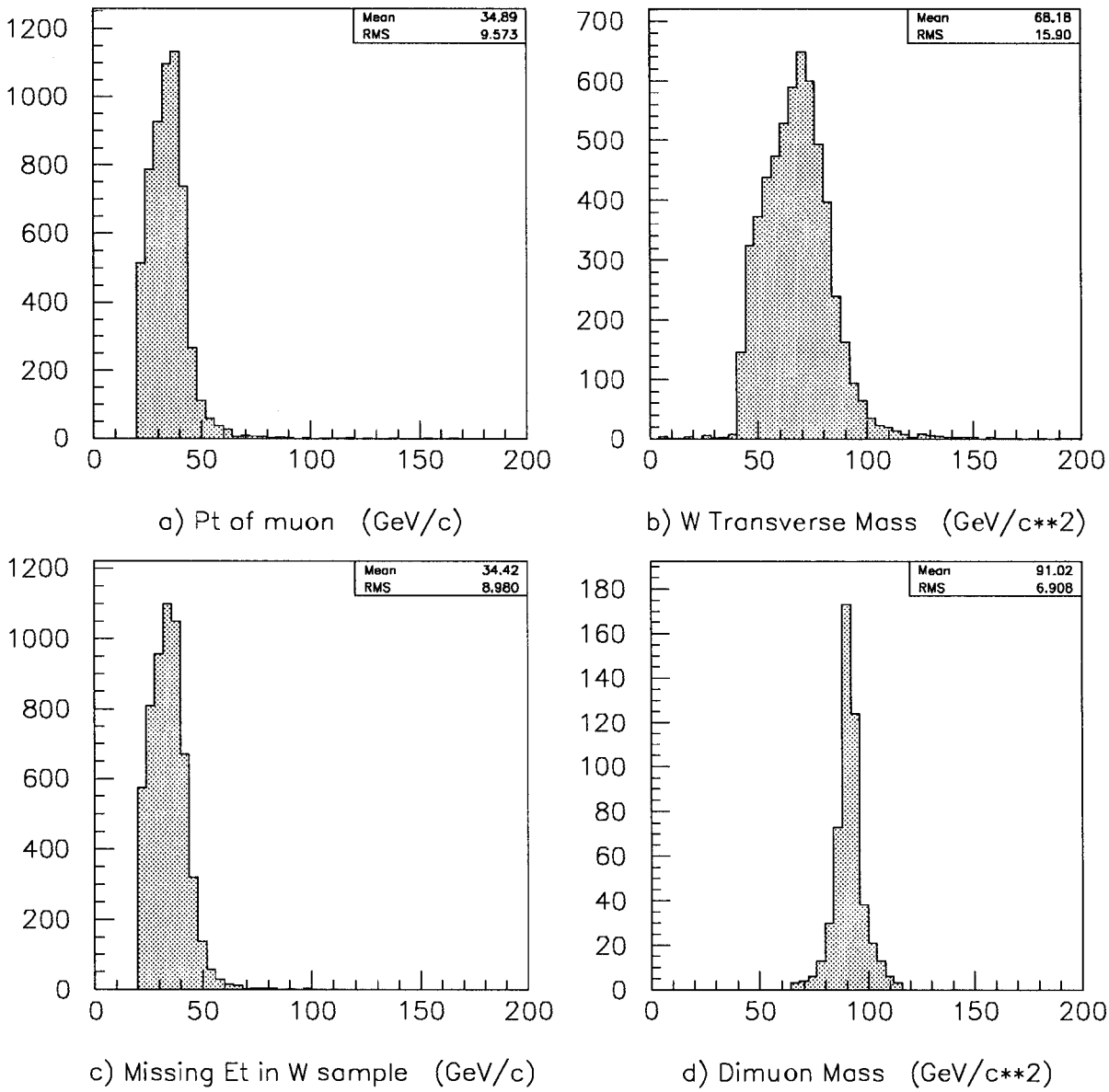


**Figure 4.4**: Figures (a)-(c) show the muon and neutrino $P_T$ as well as the $W$ transverse mass. Figure (d) shows the $Z$ peak (dimuon mass) in the $Z$ sample.

- The separation between the photon and any muon from the $W$ or $Z$ has to satisfy $\Delta R > 0.7$. This is useful for eliminating events with photons that are the result of brehmsstrahlung from the muons (see diagrams 2.1d and 2.4c, for example).

- The excess transverse energy in a cone of $\Delta R = 0.4$ centered on the photon, $ET4 = E_T^{cone} - E_T^{cluster}$, divided by the $E_T$ of the cluster has to be less than 0.15. This variable will be referred to as $ISO4 = ET4/E_T^{cluster}$.

- The summed transverse momentum of all CTC tracks in a cone of $\Delta R = 0.4$ about the photon direction, $\Sigma PT4$, has to be less than 2 $GeV/c$. The tracks used in this summation have to be reconstructed in three dimensions and originate within 10 cm of the event vertex.

- No charged tracks originating from the collision could point to the CEM cluster. The tracks have to be reconstructed in 3 dimensions. This will be referred to as the $N3D$ cut.

- $L_{shr}$, the $\chi^2$ comparison of the observed lateral shower profile to electron test-beam lateral shower profiles,

$$L_{shr} = 0.14 \cdot \Sigma_i \frac{E_i^{meas} - E_i^{pred}}{\sqrt{0.14 \cdot E^2 + (\Delta E_i^{pred})^2}} \tag{4.5}$$

had to be less than 0.50. In the above equation the summation is over the CEM towers in the EM cluster (excluding the seed tower). $E_i^{meas}$ is the measured energy in tower $i$, $E_i^{pred}$ is the predicted energy in tower $i$ predicted from the seed tower

energy, the impact point from the CES shower centroid, and the event vertex using parameterized shower profiles from test-beam data, $E$ is the EM energy of the cluster, and $\Delta E_i^{pred}$ is the uncertainty in $E_i^{pred}$ associated with a 1 cm uncertainty in the impact point measurement. All energies are in $GeV$.

- The ratio of hadronic energy to electromagnetic energy his required to be $HAD/EM < 0.055 + 0.00045 * E$, where $E$ is the total energy of the CEM cluster. The energy dependent term is a correction for energy leakage from the electromagnetic calorimeter into the hadronic calorimeter.

- Shower profile $\chi^2$ from the CES chambers (both the strip chambers and the wire chambers, $\chi^2_{strip}$ and $\chi^2_{wire}$) have to be less than 20 when fitted to electron test-beam data.

- No $2^{nd}$ CES clusters with energy above 1 $GeV$ can exist within the CEM cluster. This helps eliminate multiple photon background events such as $\pi^0$ or $\eta^0$ decays.

Figures 4.5a-f show electron testbeam distributions of $L_{shr}$, $\chi^2_{strip}$, $\chi^2_{wire}$, $HAD/EM$, $ET4/E_T$ and the second highest $E_T$ energy cluster in the CES strip chambers, respectively. As can be seen from the testbeam distributions the photon cuts listed above are very efficient for photons from $W\gamma$ and $Z\gamma$ events.

After both the inclusive $W/Z$ cuts and photon selection cuts are made there remain 7 $W\gamma$ and 4 $Z\gamma$ candidates. Figures 4.8-4.10 show the progression of photon cuts being made on the inclusive $W$ sample, and Figures 4.11-4.13 show the same progression of cuts being made on the inclusive $Z$ sample. To illustrate the effect of each photon cut,

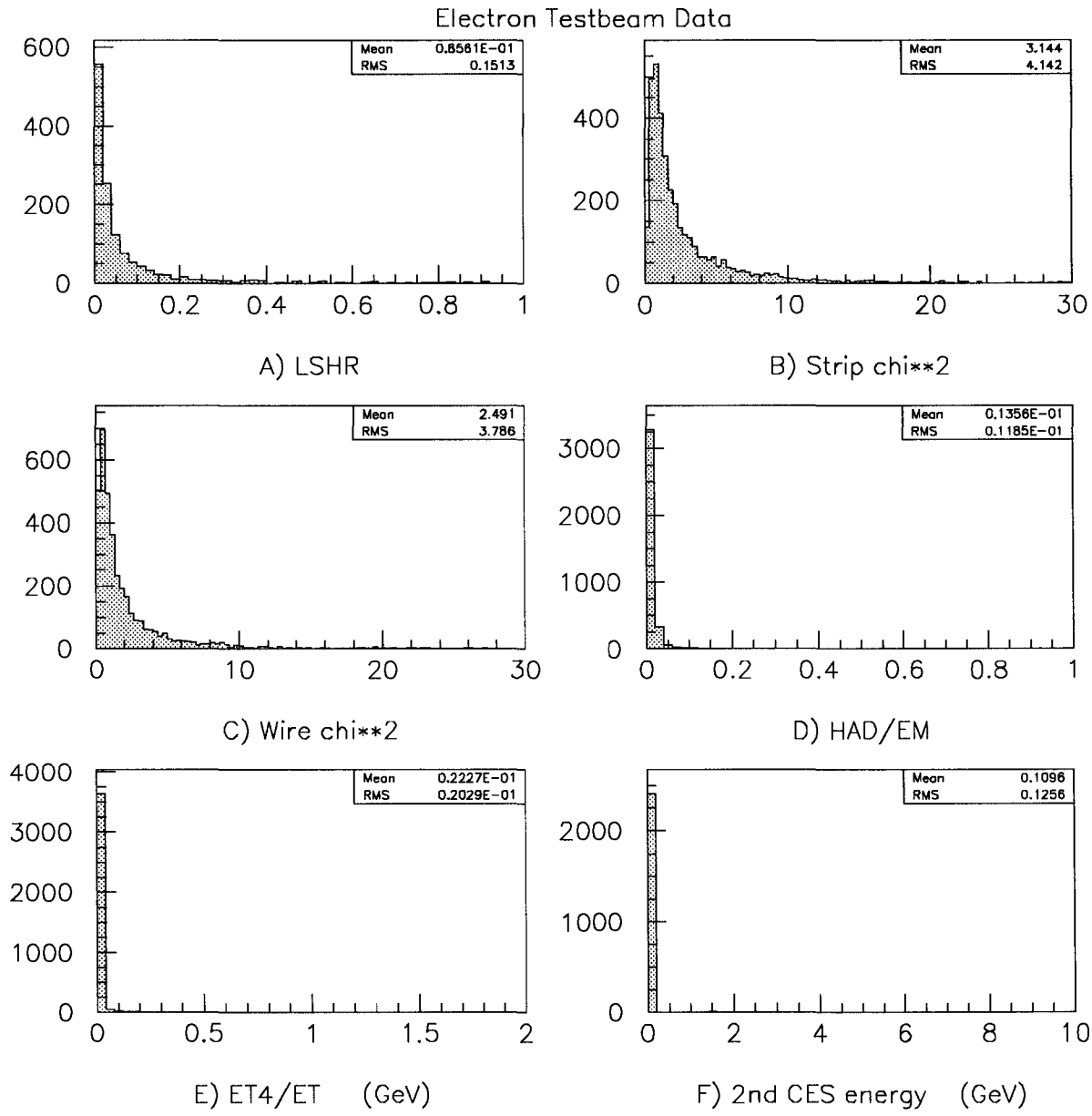


**Figure 4.5**: 10 *GeV* electron testbeam data. Photons have similar distributions, which is the reason for designing photon cuts around these electron data.

Table 4.2 lists the number of events that survive each cut in the $W$, $Z$ and background sample. The background sample will be discussed in Chapter 7 and is shown here to demonstrate the power of various cuts on the background compared to the signal. Notice that the isolation cuts have the largest impact on all samples.

An example of what one of the $Z\gamma$ events looks like is shown in Figures 4.6 and 4.7. These are two different views of the same event. Figure 4.6 shows the view of the CDF detector as seen by looking down the beam line. The circle which shows all the tracks is the CTC, and just outside of the CTC is the calorimeter. The section outside the calorimeter is the CMU, and the box surrounding all of these is the CMP. Figure 4.7 shows a 'lego' plot of the calorimetry. The calorimeters, which are cyclindrical in shape, are unrolled in $\eta$-$\phi$ space. Individual calorimeter towers are observable on this diagram as rectangles, and the relative energy deposition between the towers can be determined from this diagram by comparing the heights of the blocks (representing energy) on the diagram. This particular event has a very large $E_T$ photon candidate, as can be seen on the lego plot. This event will be discussed further in Chapter 9.

The final 7 $W\gamma$ events and 4 $Z\gamma$ events are listed in Tables 4.3 and 4.4 along with several kinematic properties of those events. In Table 4.3 $M_{CT}^{W}$ is defined as the *transverse cluster mass* (also known as the minimum invariant mass),

$$M_{CT}^{W} \equiv \sqrt{[(M_{\mu\gamma}^2 + |\vec{\mathbf{P}}_{\mathbf{T}}^{\gamma} + \vec{\mathbf{P}}_{\mathbf{T}}^{\mu}|^2)^{\frac{1}{2}} + |\vec{\mathbf{P}}_{\mathbf{T}}^{\nu_\mu}|]^2 - |\vec{\mathbf{P}}_{\mathbf{T}}^{\gamma} + \vec{\mathbf{P}}_{\mathbf{T}}^{\mu} + \vec{\mathbf{P}}_{\mathbf{T}}^{\nu_\mu}|^2} \qquad (4.6)$$

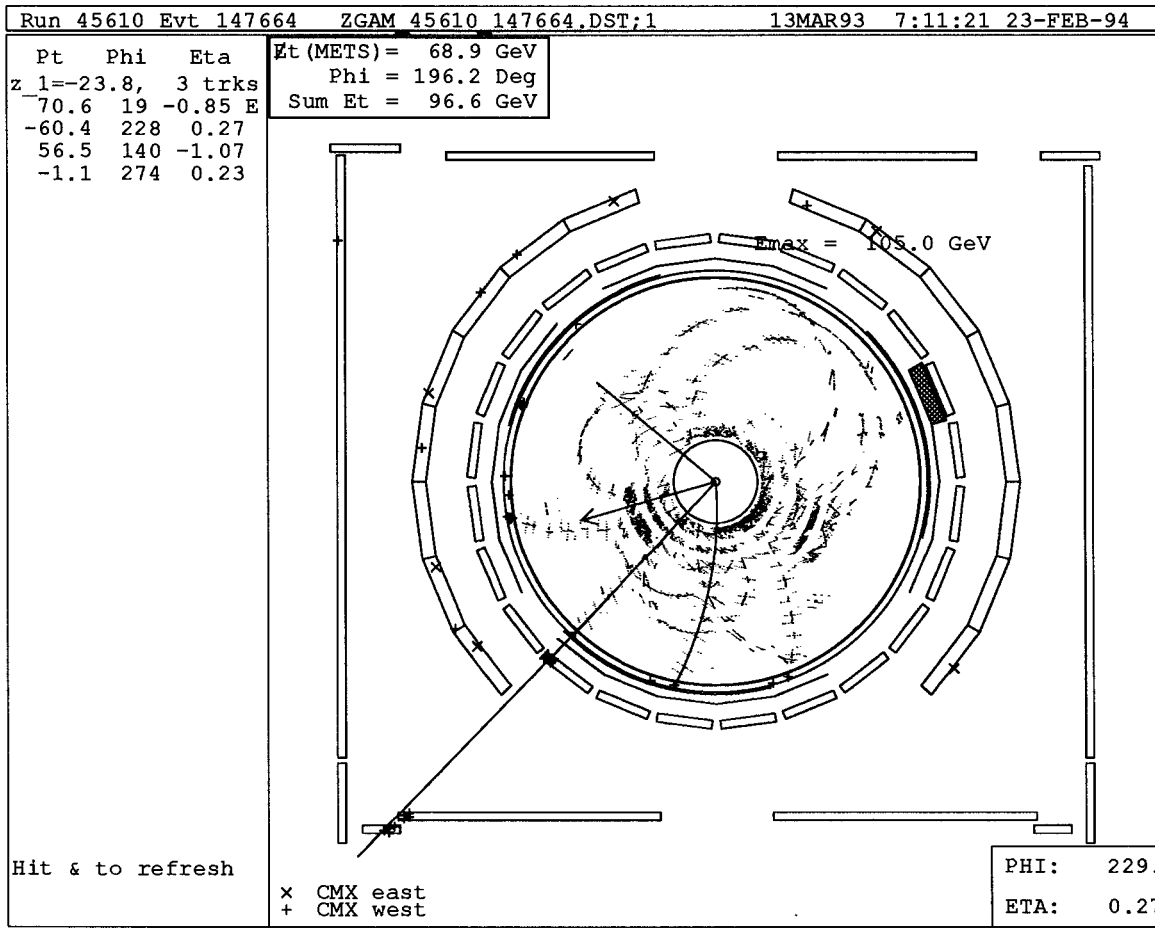


**Figure 4.6**: Event display of a $Z\gamma$ candidate as seen in a beam's eye view. The box surrounding the CTC, calorimeters and CMU detector is the CMP.

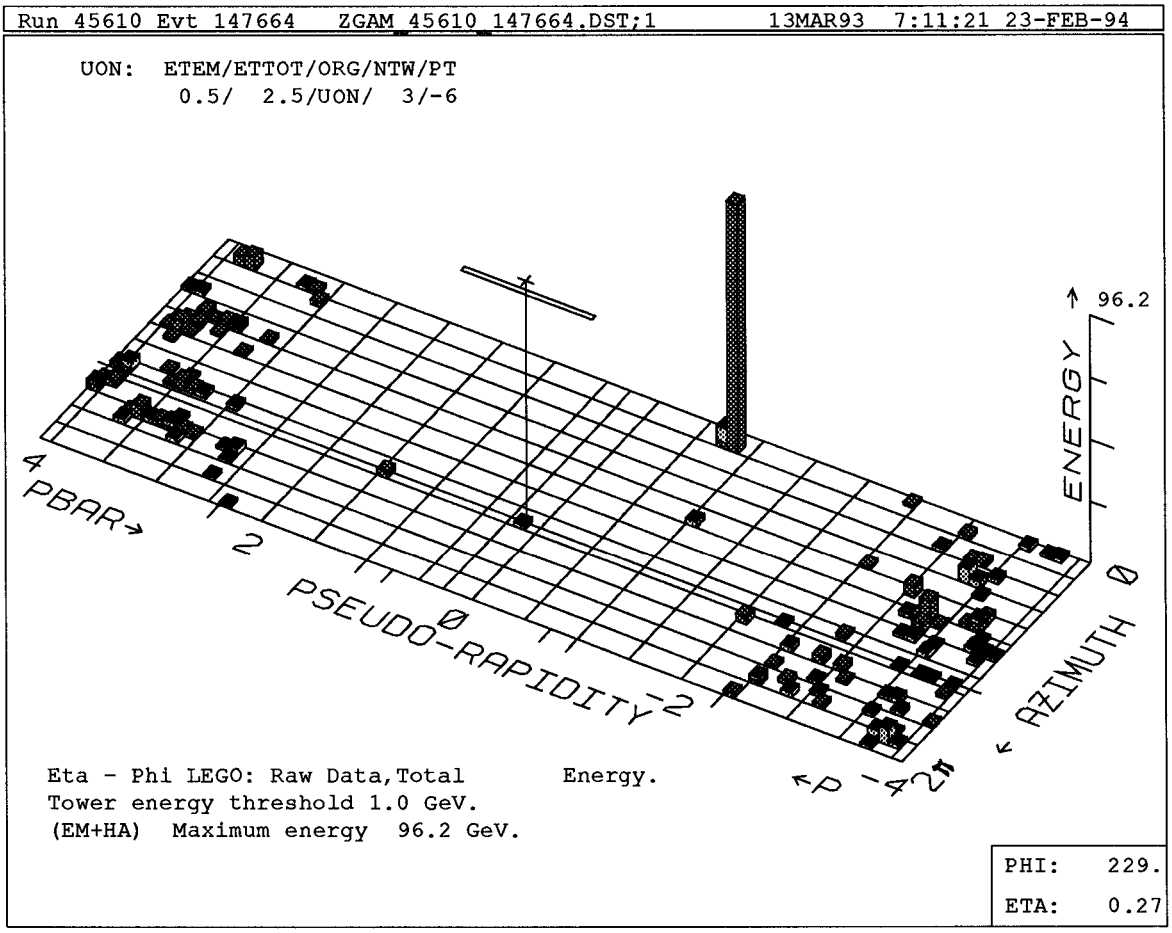


**Figure 4.7**: Event display of the same $Z\gamma$ candidate as seen in the so-called calorimeter 'lego' plot. The cylindrically shaped calorimeter is rolled out in $\eta$-$\phi$ space. Note that this event has a very high $E_T$ photon candidate (the large spike) of about 64 $GeV$.

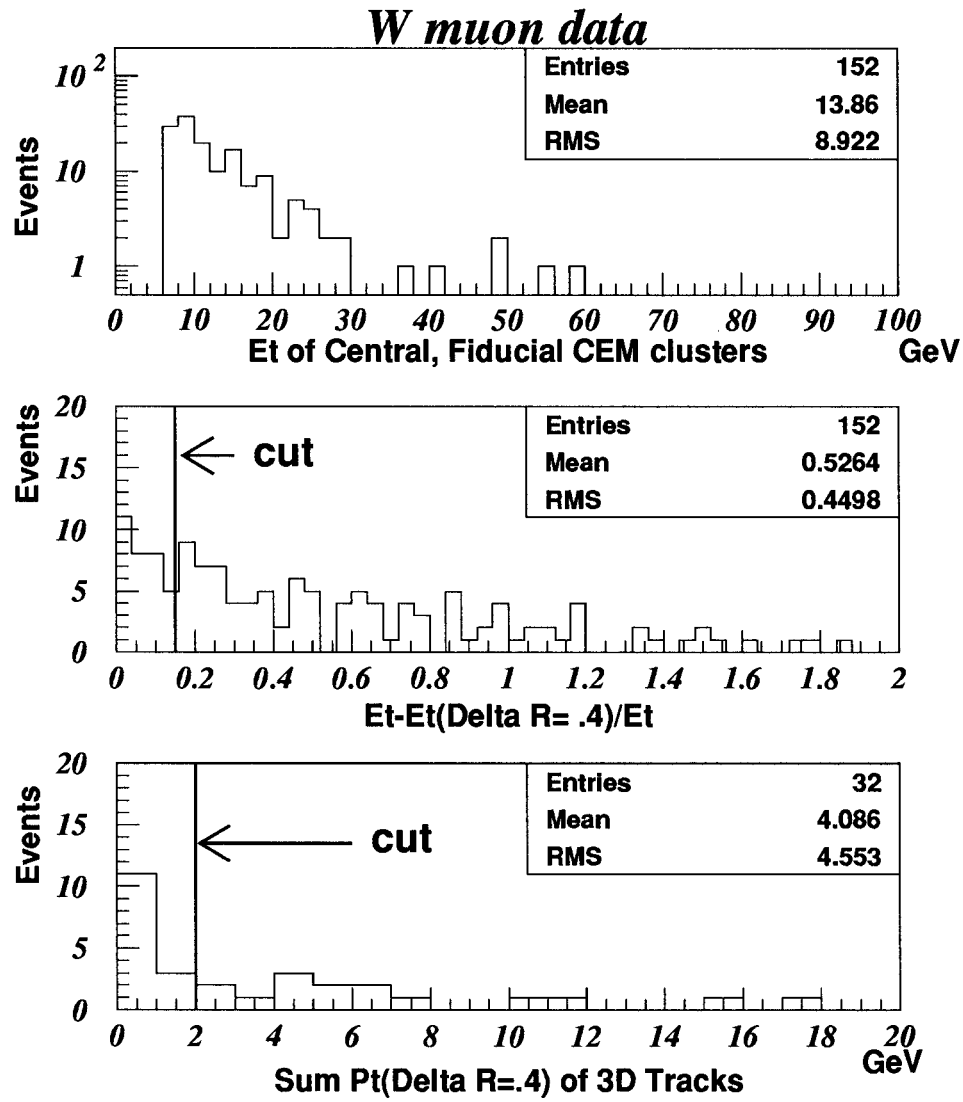


**Figure 4.8**: $E_T$ of electromagnetic clusters, and effect of isolation cuts on those clusters in the muon $W$ sample. Well isolated events are selected (i.e. to the left of the cut lines). Photon selection criteria are based on electron testbeam data as well as background studies.

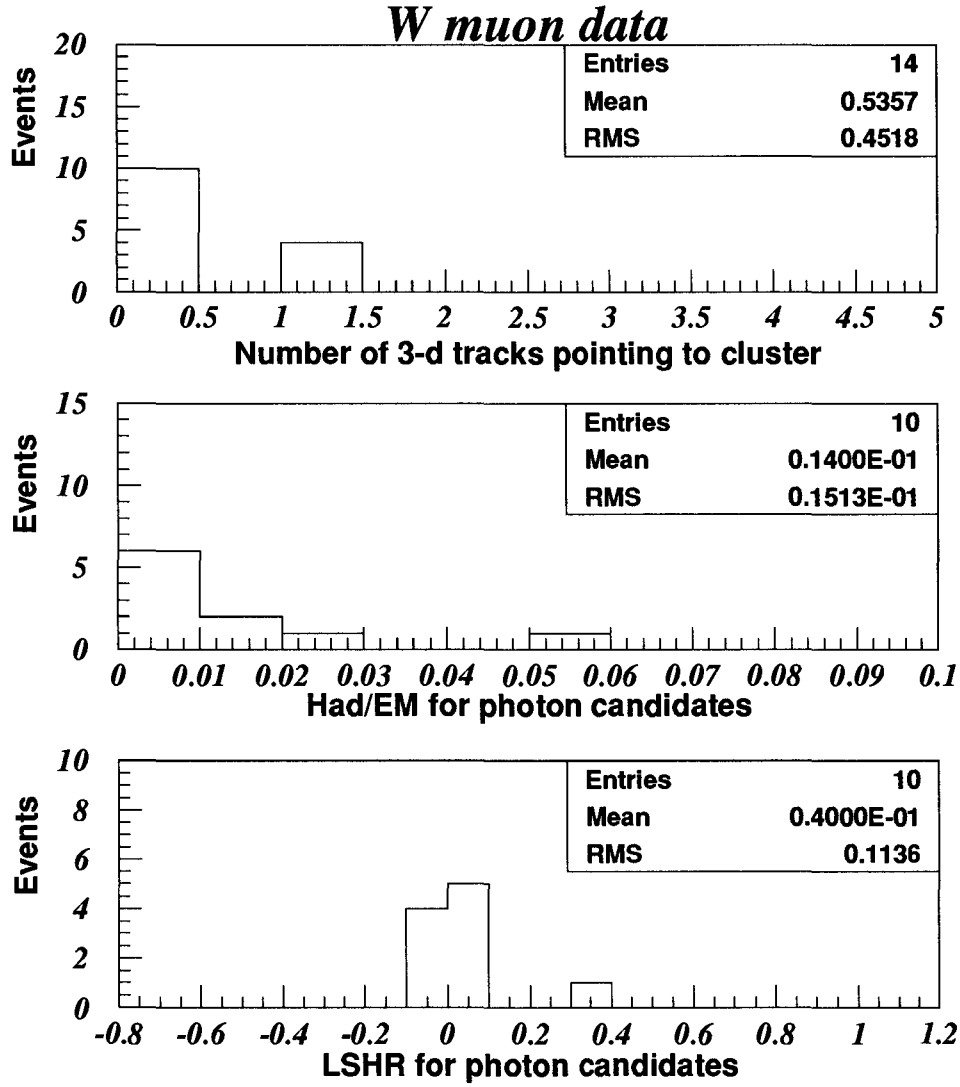


**Figure 4.9**: Additional photon cut variables in the muon $W$ sample. The variable $L_{shr}$ is defined by Eq. 4.5.

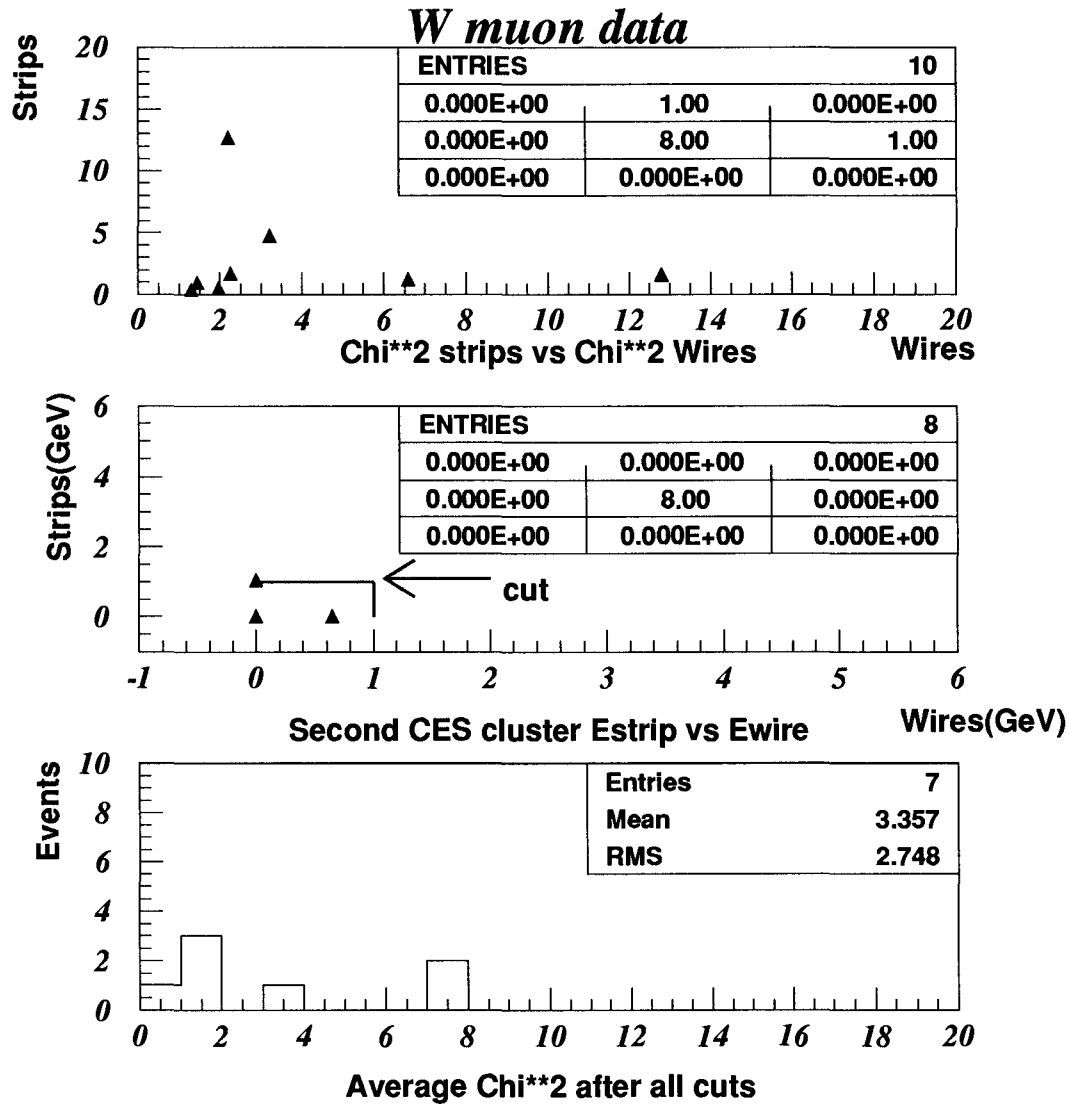


**Figure 4.10**: Photon $\chi^2$ and second cluster energies in the muon $W$ sample

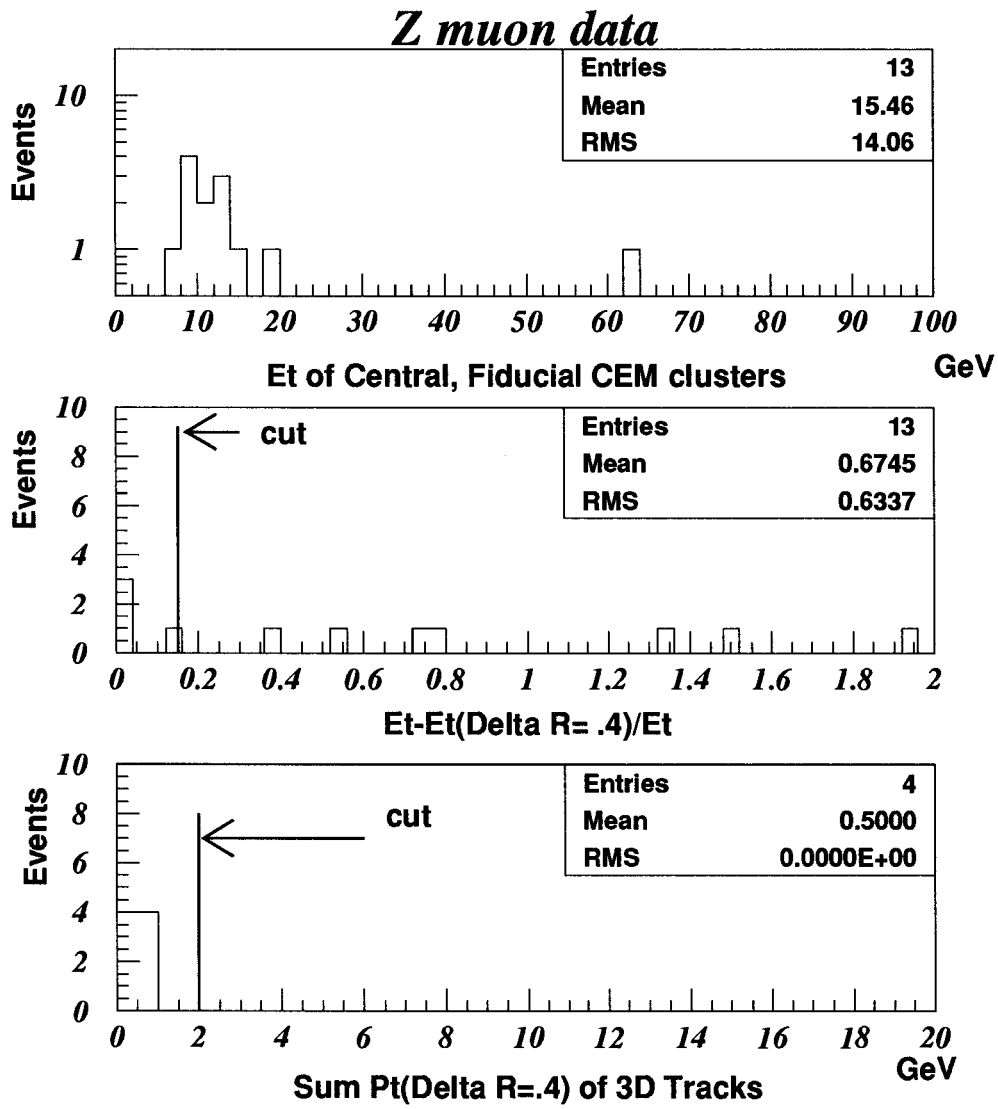


**Figure 4.11**: $E_T$ of electromagnetic clusters, and effect of isolation cuts on those clusters in the muon $Z$ sample. Well isolated events are selected (i.e. to the left of the cut lines).

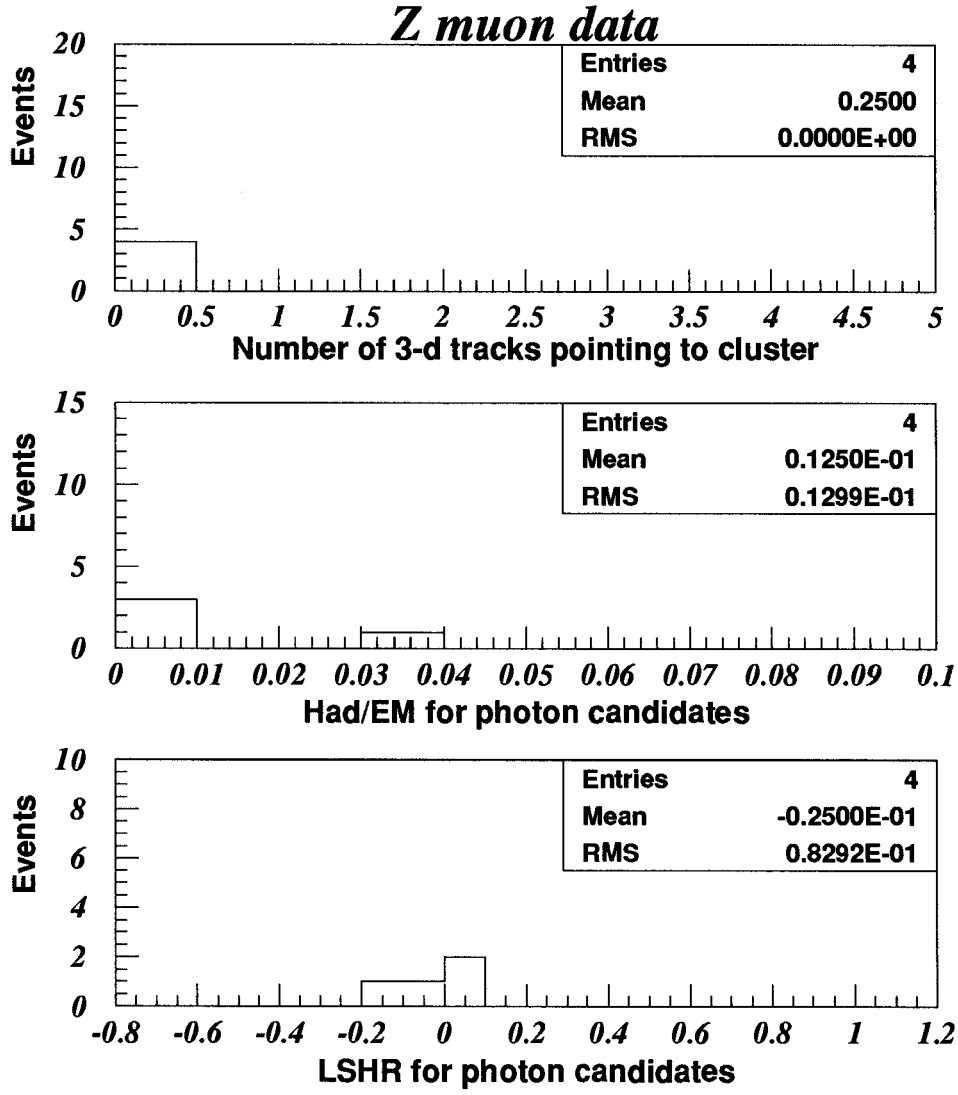


**Figure 4.12**: Additional photon cut variables in the muon $Z$ sample. The variable $L_{shr}$ is defined by Eq. 4.5.

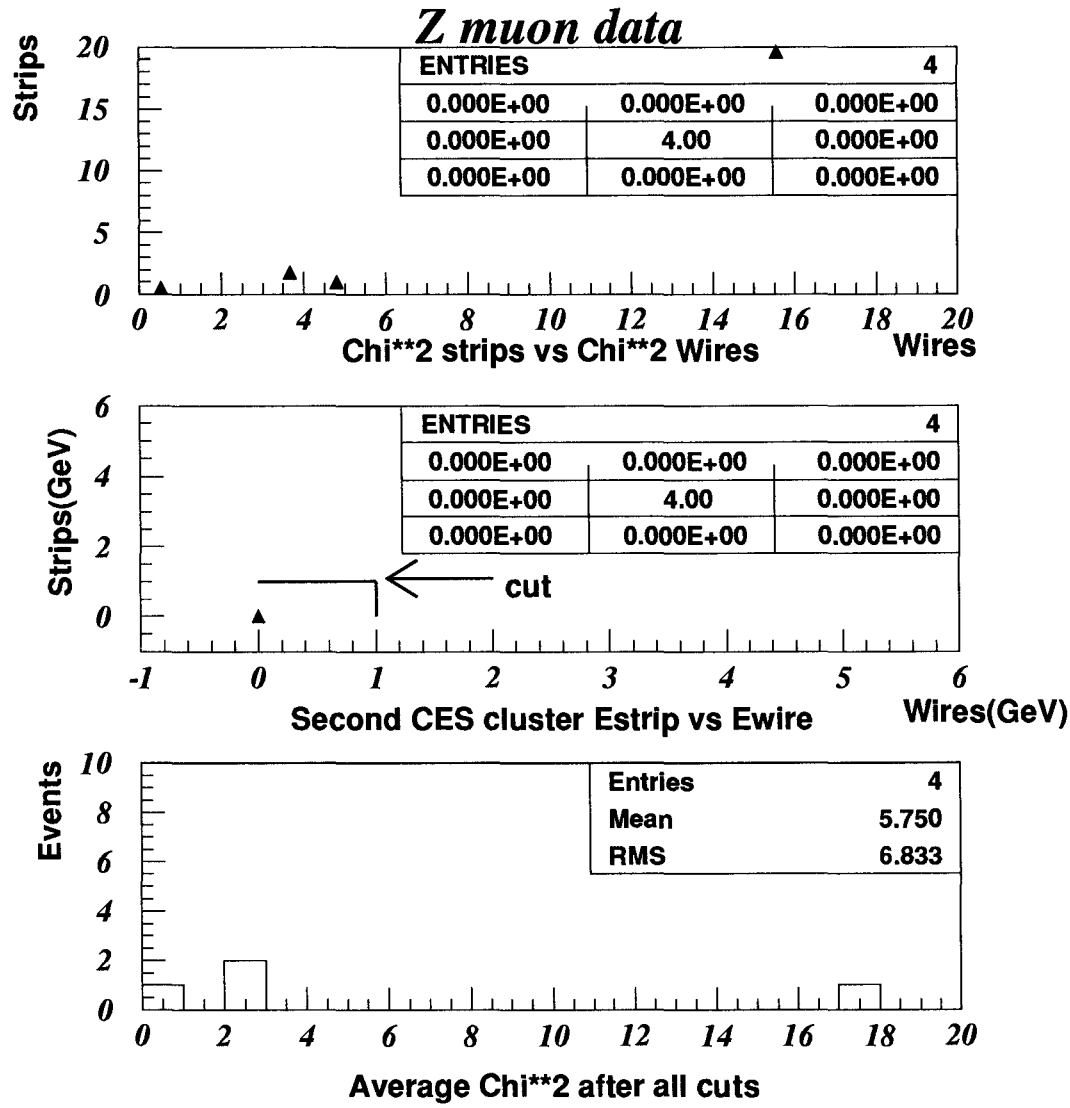


**Figure 4.13**: Photon $\chi^2$ and second cluster energies in the muon $Z$ sample

| | $W\gamma$ | $Z\gamma$ | Background |
|---|---|---|---|
| Inclusive $W/Z$ or Photon-16 Samples | 6105 | 507 | 6062 |
| Fiducial, $E_T^\gamma > 7.0$ GeV, $\Delta R_{\ell\gamma} > 0.7$ Cuts | 152 | 13 | 3067 |
| $ET4/ET < .15$ | 32 | 4 | 704 |
| $\Sigma PT4 < 2.0$ GeV | 14 | 4 | 513 |
| $N3D = 0$ | 10 | 4 | – |
| $Had/EM$ | 10 | 4 | 507 |
| $L_{shr} < 0.5$ | 10 | 4 | 407 |
| $\chi^2_{strip} + \chi^2_{wire}$ | 8 | 4 | 287 |
| no $2^{nd}$ $CES > 1$ GeV | 7 | 4 | 216 |
| no $2^{nd}$ Track ($W\gamma$ only) | 7 | – | – |

**Table 4.2**: Summary of muon $W\gamma$, $Z\gamma$ candidates and events from the jet background sample (discussed in Ch. 7) passing successive photon cuts. The entries in the first row of the first two columns are the number of inclusive $W/Z$ events; the entries in the other rows of the first four columns are the number of $W/Z$ events with fiducial CEM clusters surviving the successive photon cuts. In the last column, the first row is the number of central, fiducial, non-trigger CEM clusters with no 3-D track pointing at it.

The transverse cluster mass is useful in distinguishing between radiative $W + \gamma$ events and actual $W + \gamma$ production events. Events with $M_{CT}^W > 90\ GeV/c^2$ are more likely to be 'production' events, i.e. the result of the three boson vertex [4]. As can be seen from Table 4.3, two of the 7 $W\gamma$ events have $M_{CT}^W$ above 90 $GeV/c^2$, with a third at 89 $GeV/c^2$. This number of events is consistent with the SM expectation of $2.52 \pm 0.27$ events above 90 $GeV/c^2$. One can also relax the muon-photon angular separation requirement to let in more $W\gamma$ candidates. Relaxing the angular separation from $\Delta R > 0.7$ to $\Delta R > 0.4$ is expected to let in more radiative events, in particular muon bremmstrahlung events because in such events the photon tends to be collinear with the muon. If this is the case then one expects most of the events with small separation to also have transverse cluster masses below 90 $GeV/c^2$ because photons that are the result of muon bremmstrahlung

| | Run # Event # | $E_T^\gamma$ (GeV) | $\mu$ Charge | $M_T^W$ (GeV/c$^2$) | $M_{CT}^W$ (GeV/c$^2$) | $\Delta R_{\mu\gamma}$ |
|---|---|---|---|---|---|---|
| 1 | 41449 – 14966 | 8.63 | +1 | 55.2 | 68.9 | 1.19 |
| 2 | 41771 – 89497 | 24.13 | +1 | 62.2 | 99.5 | 3.11 |
| 3 | 43048 – 137910 | 18.47 | −1 | 43.9 | 65.6 | 1.60 |
| 4 | 45069 – 14121 | 8.72 | −1 | 42.4 | 55.3 | 2.56 |
| 5 | 45878 – 99890 | 7.31 | −1 | 73.5 | 89.1 | 2.06 |
| 6 | 46935 – 173074 | 9.06 | +1 | 54.7 | 66.4 | 2.86 |
| 7 | 47814 – 4246 | 11.81 | −1 | 121.1 | 143.1 | 1.17 |

**Table 4.3**: Kinematic Properties of Muon $W\gamma$ Candidates.

| | Run # Event # | $E_T^\gamma$ (GeV) | $M_{\mu^+\mu^-}$ (GeV/c$^2$) | $M_{Z\gamma}$ (GeV/c$^2$) | $\Delta R_{\mu\gamma}$ |
|---|---|---|---|---|---|
| 1 | 42727 – 30958 | 9.32 | 88.5 | 101.1 | 1.80 |
| 2 | 45610 – 147664 | 63.58 | 87.7 | 188.4 | 2.12 |
| 3 | 46170 – 87849 | 12.79 | 91.6 | 110.5 | 1.90 |
| 4 | 46655 – 256640 | 10.80 | 72.8 | 88.7 | 0.98 |

**Table 4.4**: Kinematic Properties of Muon $Z\gamma$ Candidates.

also tend to have low $E_T$. This turns out to be the case, as four more $W\gamma$ candidates lie in the region $0.4 < \Delta R < 0.7$. This is consistent with an expected signal of $6.1 \pm 0.8$ events in the same $\Delta R$ region. Three of the four events have $M_{CT}^W < 75\ GeV/c^2$, which suggests that indeed these events are mostly radiative events.

Figures 4.14-4.16 show the data overlaid on Monte Carlo SM distributions for the photon $E_T$, muon-photon separation and transverse cluster mass. Figure 4.17 shows the muon-photon separation using the $\Delta R > 0.4$ requirement. The estimated background distribution is also shown on the plots. Both the Monte Carlo and background estimates will be discussed in the next few chapters. The shapes of the observed distributions, though statistically limited, agree well with the SM predictions.

In Table 4.4 $M_{\mu^+\mu^-}$ is the dimuon invariant mass and $M_{Z\gamma}$ is the dimuon plus photon invariant mass. The $\Delta R_{\mu\gamma}$ value is taken to be the closest separation between the photon

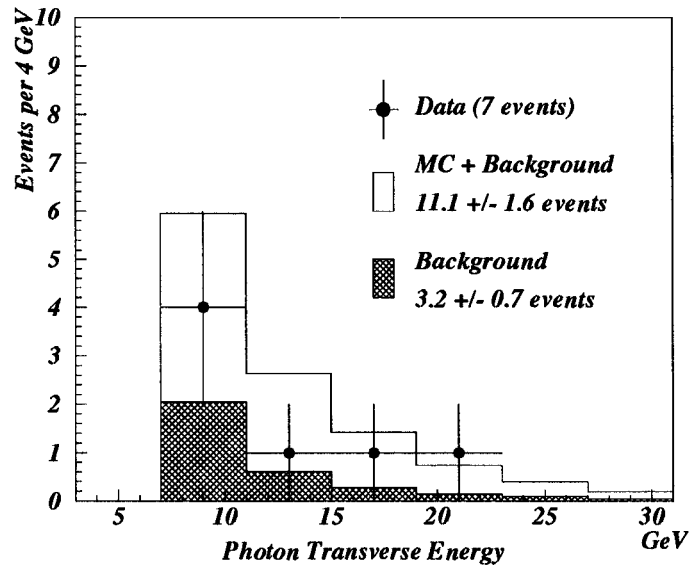


**Figure 4.14**: The photon $E_T$ of the 7 $W\gamma$ events, overlaid on SM Monte Carlo predictions and background estimates.

and one of the muons of the $Z$. Figures 4.18 and 4.19 show the 4 $Z\gamma$ events overlaid on Monte Carlo SM distributions for the photon $E_T$ and dimuon-photon three body mass.

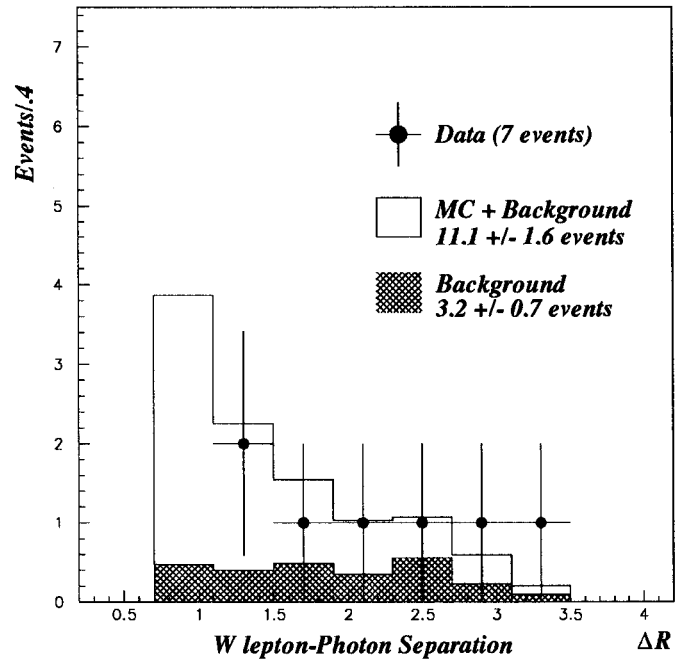


**Figure 4.15**: The muon-photon separation of the 7 $W\gamma$ events, overlaid on SM Monte Carlo predictions and background estimates.

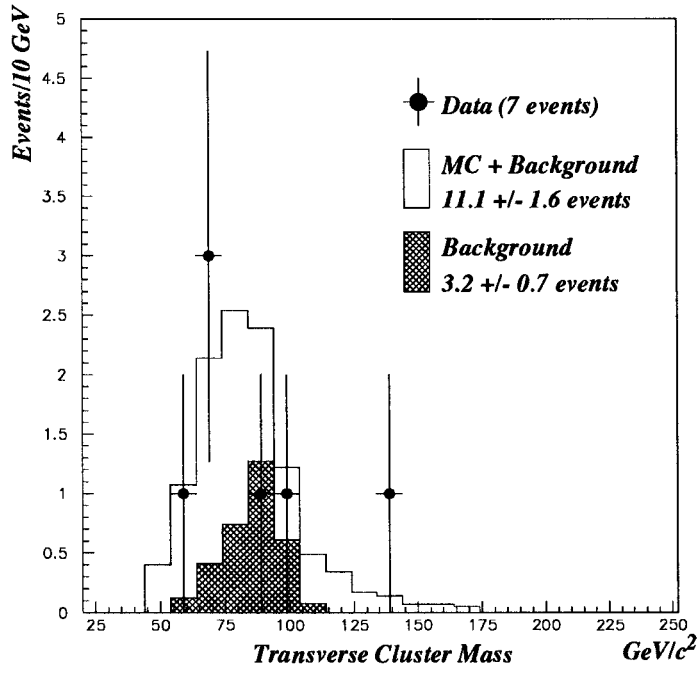


**Figure 4.16**: The transverse cluster mass of the 7 $W\gamma$ events, overlaid on SM Monte Carlo predictions and background estimates. Radiative events are not expected to be above 90 $GeV/c^2$.

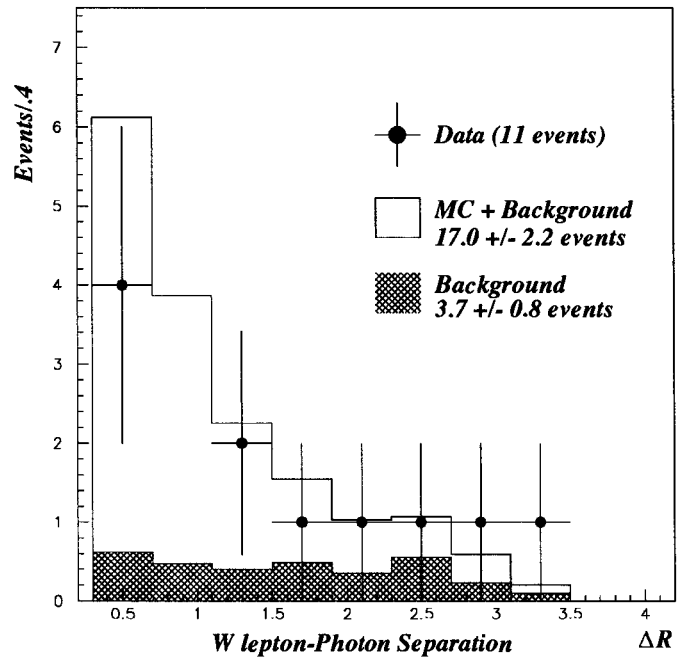


**Figure 4.17**: The muon-photon separation of the 11 $W\gamma$ events after using the requirement $\Delta R > 0.4$, overlaid on SM Monte Carlo predictions and background estimates. Note that three of the four events in the lowest $\Delta R$ bin have low $M_{CT}^{W}$ ($< 75\ GeV/c^2$), suggesting that they are indeed mostly radiative events.

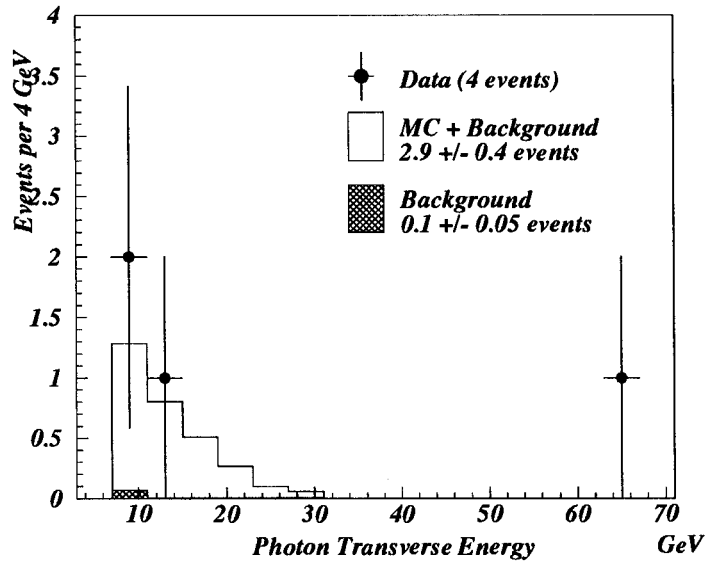


**Figure 4.18**: The photon $E_T$ of the 4 $Z\gamma$ events, overlaid on SM Monte Carlo predictions.

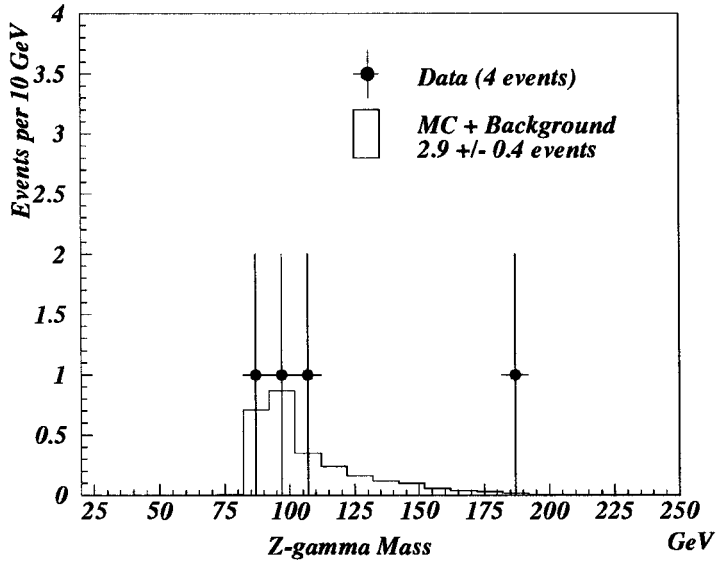


**Figure 4.19**: The 3-body mass (dimuon-photon) of the 4 $Z\gamma$ events, overlaid on SM Monte Carlo predictions.

# Chapter 5

# Efficiencies

In order to measure cross sections, the efficiencies for all muon and photon cuts are needed. A selection cut efficiency for muons or photons is the probability that a particular selection requirement is satisfied by real muons or photons. This chapter discusses the methods used to measure various selection cut efficiencies and summarizes the results.

## 5.1 Muon Efficiencies

Efficiencies for the selection cuts of high-$P_T$ muon $W$ and $Z$ samples are measured using the inclusive muon $Z$ sample. The strategy is to select $Z$ events which have *both* muons passing through muon detectors and possessing $P_T$ at or above 20 $GeV/c$. For events which satisfy these requirements, events which have at least one of the muon candidates passing *all* of the muon criteria listed in the previous chapter are then selected. No other requirements are made on the second muon candidate. For events which pass these

selections, a tight dimuon invariant mass requirement of $75 < M_{\mu\mu} < 105\ GeV$ is made. This mass cut assures us of a very pure sample of $Z$ events and that there are in fact two high-$P_T$ muons present in each event.

To measure individual muon cut efficiencies, a specific cut is made on the second muon. Making each cut individually removes various correlations between the cut in question and others. The actual efficiency, $\epsilon_c$, for a selection cut, $c$, is determined using the following algorithm: first the ratio of the number of second leg muons which pass cut $c$, $N_c$, to the total number of $Z$ events in the sample, $N_Z$, is calculated. This ratio is called $R_c = N_c/N_Z$. One has to be careful to distinguish between muons passing through different detectors. In this case, events must be separated based on whether the second muon went through the CMU, CMP, both the CMU and CMP, or the CMX. This is done in order to get efficiencies for the CMU and CMP detectors (the CMX is not used). For the sample used, $N_Z$ is 416. Of these, 65 events have second leg muons passing through the CMU only, 33 through the CMP only, and 216 through the CMU and CMP. The remaining 102 events have second leg muons in the CMX and are discarded.

There are three possible outcomes to consider for each individual cut from the above selections. These outcomes are

1. Both muons satisfy the cut.

2. The muon with the highest $P_T$ passes the cut and the other does not.

3. The muon with the lower $P_T$ passes the cut and the other does not.

These three outcomes are assigned probabilities based on the total number of $Z$ events from the inclusive $Z$ sample , $N_{total}$, and the efficiency $\epsilon_c$. Assuming that $\epsilon_c$ is independent of muon $P_T$, a reasonable assumption for muons from $Z$ decays, we have

1. $Prob$(both pass) $= N_{total}\epsilon_c^2$

2. $Prob$(highest $P_T$ passes, other fails) $= N_{total}\epsilon_c(1-\epsilon_c)$

3. $Prob$(lower $P_T$ passes, other fails) $= N_{total}(1-\epsilon_c)\epsilon_c$

The ratio $R_c$ defined above can be represented in terms of these probabilities since $N_Z$ is the sum of all events which have at least one of the two muons passing cut $c$:

$$R_c = \frac{N_{total}\epsilon_c^2}{N_{total}\epsilon_c(1-\epsilon_c) + N_{total}(1-\epsilon_c)\epsilon_c + N_{total}\epsilon_c^2} \tag{5.1}$$

Solving for the efficiency $\epsilon_c$ gives

$$\epsilon_c = \frac{2R_c}{(1+R_c)} \tag{5.2}$$

This method is used to measure the efficiencies for the stub-matching requirements, $\epsilon_{cmu\ dx}$ and $\epsilon_{cmp\ dx}$, the minimum ionization requirements, $\epsilon_{em}$ and $\epsilon_{had}$, and the muon isolation requirement, $\epsilon_{iso}$. Table 5.1 summarizes the efficiencies for CMU and CMP selection cuts.

Included in Table 5.1 are three other efficiencies, where $\epsilon_{cos}$ is the (over)efficiency of a cosmic ray removal filter, $\epsilon_{trk}$ is the pattern recognition efficiency of the CTC track

finding algorithm, and $\epsilon_{cmuo}$ is the efficiency for reconstructing muon stubs in the muon detectors.

The cosmic ray efficiency is determined from the inclusive high $P_T$ muon sample. Cosmic rays are identified, for instance, as two charged tracks on opposite sides of the detector ("back-to-back" tracks, which are separated by $180° \pm 2°$ in $\phi$) which normally do not pass near the point where a $p\overline{p}$ interaction took place. Events are removed from the $W$ and $Z$ samples if any of the following are true:

- The impact parameter of the muon with respect to the beamline is more than 5 mm or the muon passes more than 5 cm from the event vertex.
- A track with $P_T > 10\ GeV/c$, which is back-to-back (as defined above) with the muon track, fails track quality requirements. Both tracks must be within $|\eta| < 1.2$, where the CTC tracking is most efficient.
- A track with $P_T > 10\ GeV/c$, which is back-to-back (as defined above) with the muon track, is identified by CTC track reconstruction to be one continuous track. The track must be within $|\eta| < 1.2$, where the CTC tracking is most efficient.

Events which are identified as cosmic rays are hand-scanned to see if they actually are consistent with cosmic rays (based on the criteria listed above) or $p\overline{p}$ interactions. The efficiency used in the analysis is the efficiency of keeping $p\overline{p}$ interactions.

The CTC track-finding efficiency is needed because the knowledge of the existence of a muon depends on tracks in the CTC matching with hits in the muon chambers. The efficiency is determined from the electron $W$ sample where $W$ events can be identified

| | | |
|---|---|---|
| $\epsilon_{cmu\ dx}$ | $0.973 \pm 0.008$ | CTC-CMU Track-Stub Match |
| $\epsilon_{cmp\ dx}$ | $0.998^{+0.002}_{-0.005}$ | CTC-CMP Track-Stub Match |
| $\epsilon_{em}$ | $0.969^{+0.006}_{-0.007}$ | EM Energy in Muon Tower |
| $\epsilon_{had}$ | $0.989^{+0.004}_{-0.005}$ | HAD Energy in Muon Tower |
| $\epsilon_{iso}$ | $0.957^{+0.008}_{-0.009}$ | Muon Isolation |
| $\epsilon_{trk}$ | $0.997 \pm 0.001$ | CTC Tracking |
| $\epsilon_{cmuo}$ | $0.971^{+0.014}_{-0.022}$ | Muon Stub Finding |
| $\epsilon_{cos}$ | $0.998^{+0.001}_{-0.004}$ | Cosmic Ray Filter |
| $\epsilon_{cuts}$ | $0.845^{+0.018}_{-0.025}$ | All Cuts |

**Table 5.1**: Muon Efficiencies for $W$ and $Z$ selection.

using the calorimeter only. The muon stub-finding efficiency is measured from the muon $Z$ sample using a method very similar to the method described above for the muon quality requirements. One change in the above method, though, is that the second muon from the $Z$ decay is not required to form a stub in a muon detector. For events in which both muons leave stubs, a dimuon invariant mass between 75 and 105 $GeV/c^2$ is made. For events in which only one muon made a stub in a muon detector, the muon-2nd track invariant mass must also be between 75 and 105 $GeV/c^2$. This allows us to be confident that the second high-$P_T$ track is a muon. Equation 5.2 is then used to determine the efficiency, based on the probabilities that both muons form stubs, the highest $P_T$ muon forms a stub and the other does not, and the lowest $P_T$ muon forms a stub and the other does not.

The overall muon-finding efficiency, $\epsilon_{cuts} = 84.5\%$, is the product of all the muon efficiencies in the table.

| Data Sample | $\epsilon^{\gamma}_{Had/EM}$ | $\epsilon^{\gamma}_{Lshr}$ | $\epsilon^{\gamma}_{\chi^2_{stp}+\chi^2_{wir}}$ | $\epsilon^{\gamma}_{no\ 2^{nd}\ CES}$ |
|---|---|---|---|---|
| 5 GeV $e$ Test Beam | $98.9 \pm 0.2\%$ | $99.9 \pm 0.1\%$ | $97.3 \pm 0.3\%$ | $98.0 \pm 0.1\%$ |
| 10 GeV $e$ Test Beam | $99.6 \pm 0.1\%$ | $98.8 \pm 0.4\%$ | $96.2 \pm 0.4\%$ | $97.9 \pm 0.1\%$ |
| 18 GeV $e$ Test Beam | $99.1 \pm 0.9\%$ | $100.0\ ^{+0.0}_{-1.7}\%$ | $98.2 \pm 1.8\%$ | $98.2 \pm 1.6\%$ |
| 30 GeV $e$ Test Beam | $98.9 \pm 0.9\%$ | $100.0\ ^{+0.0}_{-1.1}\%$ | $99.2 \pm 0.7\%$ | $98.2 \pm 1.0\%$ |
| 50 GeV $e$ Test Beam | $98.0 \pm 0.3\%$ | $99.9 \pm 0.1\%$ | $99.2 \pm 0.2\%$ | $97.6 \pm 0.2\%$ |

**Table 5.2**: CEM photon efficiency determination for EM shower variables. The statistical uncertainty associated with each quantity is given.

## 5.2 Photon Efficiencies

The efficiencies for some of the photon selection cuts are measured using data taken before Run 1A from electron test-beams of various energies. Electrons and photons have nearly the same response in the calorimeters. The efficiencies for $L_{shr}$, the transverse shower profile $\chi^2$s from the CES, the hadronic to electromagnetic energy ratio, and the second cluster energy cuts are all determined with these samples. Table 5.2 shows the efficiencies of these selection cuts for different $E_T$ test-beam samples. Note there is a slight $E_T$ dependence to the efficiency.

The efficiencies of the two isolation cuts ($\Sigma PT4$ and $ISO4$) and the no 3D track cut ($N3D$) are measured using the inclusive electron and muon $W$ and $Z$ samples. For each event, five cones of size 0.4 in $\Delta R$ are pointed in random directions in the central region of the detector ($|\eta| < 1.1$). The only other requirement on these cones is that they be separated from the lepton(s) by at least 0.7 units in $\Delta R$. This separation is required since it is the same separation between photons and the lepton(s) used in the analysis. It also prevents overlap between the cone and the lepton. Within each cone the $ET4$ and

| Data Sample | $\epsilon_{\Sigma PT4<2.0 \cdot N3D}$ | |
|---|---|---|
| $W_e$ Random Cones | $90.8 \pm 0.2\%$ | |
| $W_\mu$ Random Cones | $90.8 \pm 0.4\%$ | |

**Table 5.3**: CEM $\Sigma PT4 \cdot N3D$ photon efficiencies.

$\Sigma PT4$ values centered on the cone axis, as well as the number of 3-dimensional tracks, are measured. The efficiencies of the $\Sigma PT4$ and $N3D$ track cuts are taken to be the ratio of the number of cones which contain summed track $P_T$ less than 2 $GeV$ or no tracks, respectively, to the total number of cones used. The $ISO4 = ET4/E_T$ efficiency is determined in a slightly different manner due to its dependence on the $E_T$ of the energy cluster. First, the number of cones containing $X < ET4 < (X + 0.25\ GeV)$ are counted, where $X$ ranges from 0 to 10 $GeV$. This forms energy bins of width 0.25 $GeV$ from 0 to 10 $GeV$. From this distribution the efficiency for $ET4 < X$ is the number of all cones containing $ET4$ less than $X$ divided by the total number of cones. The efficiency for $ISO4 = ET4/E_T < 0.15$ can then be calculated directly. For example, for a photon with $E_T = 10\ GeV$ the requirement for passing $ET4/E_T < 0.15$ is that $ET4 < 1.5\ GeV$. The $ISO4$ efficiency is just the efficiency of $ET4 < 1.5\ GeV$.

The $\Sigma PT4$ times $N3D$ cut efficiency results are shown in Table 5.3 and the $E_T$-dependent efficiency results for $ISO4$ are shown in Table 5.4.

The results for all other photon efficiencies are summarized in Table 5.5. Included in Table 5.5 are the photon survival probability $\mathcal{P}^{\gamma}_{\overline{conv}}$ and the photon vs electron shower development factor $\mathcal{S}^{cem}_{e\to\gamma}$, defined below. The photon survival probability is the probability that a photon will pass through all the material associated with the central detector

| $E_T Bin(GeV)$ | $\epsilon_{ET4/E_T<0.15}$ |
|---|---|
| 7-11 | $89.2 \pm 1.0\%$ |
| 11-15 | $94.2 \pm 1.0\%$ |
| 15-19 | $96.5 \pm 1.0\%$ |
| 19-23 | $97.6 \pm 1.0\%$ |
| 23-27 | $98.3 \pm 1.0\%$ |
| 27-10000 | $99.1 \pm 1.0\%$ |

**Table 5.4**: $E_T$ dependent CEM photon isolation efficiency, $ISO4$.

without converting to a $e^-e^+$ pair. The amount of material corresponds to $6.8 \pm 0.2\%$ of a conversion length, $\chi_o^\gamma$. The survival probability of a photon in one conversion length of material is $\mathcal{P}_{conv}^{\gamma} = e^{-\chi_o^\gamma}$. The photon vs electron shower development correction factor $\mathcal{S}_{e\to\gamma}^{cem}$ is defined as the ratio of the products of photon selection efficiencies to electron selection efficiencies. The efficiencies used in the products are $\epsilon_{Had/EM}$, $\epsilon_{Lshr}$, $\epsilon_{\chi^2_{stp}+\chi^2_{wir}}$ and $\epsilon_{no\ 2^{nd}\ CES}$, and are determined from a CDF detector simulation called QFL. This correction factor accounts for any slight differences in the overall photon efficiency when using electron testbeam data to measure photon cut efficiencies. Note that the QFL photon selection efficiency is slightly higher than the electron selection efficiency, so $\mathcal{S}_{e\to\gamma}^{cem}$ is over 100%.

The overall $E_T$-independent photon selection efficiency used in the analysis is $81.2 \pm 2.3\%$, as shown in Table 5.5. The final photon efficiency used in the analysis combined the $E_T$-independent efficiency with the weighted average $ISO4$ efficiency (weighted using the SM $W\gamma$ photon $E_T$ spectrum; it is assumed that the data are consistent with the SM). The final efficiency results are shown in Table 5.6

| | | |
|---|---|---|
| $\epsilon^{\gamma}_{\Sigma PT4}$ | $95.2 \pm 0.1 \pm 0.8\%$ | Tracking Isolation |
| $\epsilon^{\gamma}_{N3D}$ | $95.6 \pm 0.1 \pm 0.7\%$ | No track @ $EM$ Cluster |
| $\epsilon^{\gamma}_{Had/EM}$ | $99.2 \pm 0.9 \pm 0.8\%$ | $Had/EM$ Cut |
| $\epsilon^{\gamma}_{Lshr}$ | $99.9 \pm 0.1 \pm 0.3\%$ | Lateral Shower Cut |
| $\epsilon^{\gamma}_{\chi^2_{stp}+\chi^2_{wir}}$ | $98.4 \pm 0.1 \pm 0.9\%$ | CES strip/wire $\chi^2$ Cut |
| $\epsilon^{\gamma}_{no\ 2^{nd}\ CES}$ | $97.9 \pm 0.7 \pm 1.0\%$ | No $2^{nd}$ CES Clusters |
| $\mathcal{P}^{\gamma}_{\overline{conv}}$ | $93.4 \pm 0.1 \pm 0.5\%$ | Photon Survival |
| $\mathcal{S}^{cem}_{e\to\gamma}$ | $100.3 \pm 0.6 \pm 1.0\%$ | $\gamma$ *vs.* $e$ Shower Development |
| $\epsilon^{\gamma}_{cem}$ | $81.2 \pm 1.3 \pm 1.9\%$ | Overall Photon Efficiency |

**Table 5.5**: Overall CEM Photon Efficiency Determination. The statistical and sytematic uncertainties associated with each quantity are given.

| Data Sample | | |
|---|---|---|
| $W_e$ Random Cones | $75.2 \pm 2.1\%$ | |
| $W_\mu$ Random Cones | $75.3 \pm 2.1\%$ | |
| $Z_\mu$ Random Cones | $76.8 \pm 1.7\%$ | |

**Table 5.6**: Overall CEM Photon Efficiency- weighted average over $E_T$ bins.

### 5.2.1 Photon Clustering Efficiency

In order to look at the electron testbeam data offline and carry out the efficiency studies of various electron/photon quantities mentioned above, software is used to 'cluster' the raw data collected by the calorimeters. The clustering algorithm is briefly discussed in Appendix B. Certain thresholds are used by the offline reconstruction programs to define which energy clusters are kept and which clusters are not interesting. In order to be kept, at least one calorimeter tower is required to contain at least 3 $GeV$ of energy. At least one adjacent tower is required to contain 2 $GeV$ or more of energy. The $E_T$ of the cluster is required to be above 5 $GeV$. A potential problem with the clustering algorithm is that if it is inefficient, some energy clusters that should be found are actually not found. One needs to be sure that the clustering algorithm is fully efficient in the region of interest, which is at and above a photon $E_T$ of 7 $GeV$, or else potential photon candidates may be lost.

The clustering efficiency is measured from a 16 $GeV$ photon sample, which is used in the background analysis (see Chapter 7), and is checked using QFL Monte Carlo photon samples. In the photon data, the $E_T$ spectrum of photon candidates falls exponentially as the $E_T$ increases. However, for $E_T$ values below 6 $GeV$, the number of events decreases rapidly from what one expects from the rest of the spectrum. Figure 5.1 shows the number of central 'photons' in the data as a function of $E_T$ and the exponential fit to the $E_T$ spectrum. The clustering efficiency is defined as the number of observed 'photons' in the photon data divided by the number of events expected from the fit in each bin. From Monte Carlo data, the efficiency of the clustering algorithm is defined as the ratio of

number of central energy clusters, after using the energy thresholds mentioned above, to the number of central energy clusters after using lower energy thresholds in the clustering algorithm. The lower thresholds are at least one calorimeter tower with energy above 1.5 $GeV$, an adjacent tower with energy of at least 1 $GeV$, and a minimum cluster $E_T > 3$ $GeV$. The ratio from the data should compare favorably with the Monte Carlo efficiency curve if the drop-off in the data is the result of a clustering inefficiency near the $E_T$ threshold. The efficiency curve is shown in Figure 5.2. The data and Monte Carlo are in good agreement with each other, and the clustering using the default energy thresholds becomes fully 'efficient' around an $E_T$ of 6 $GeV$. This is below our photon requirement of 7 $GeV$.

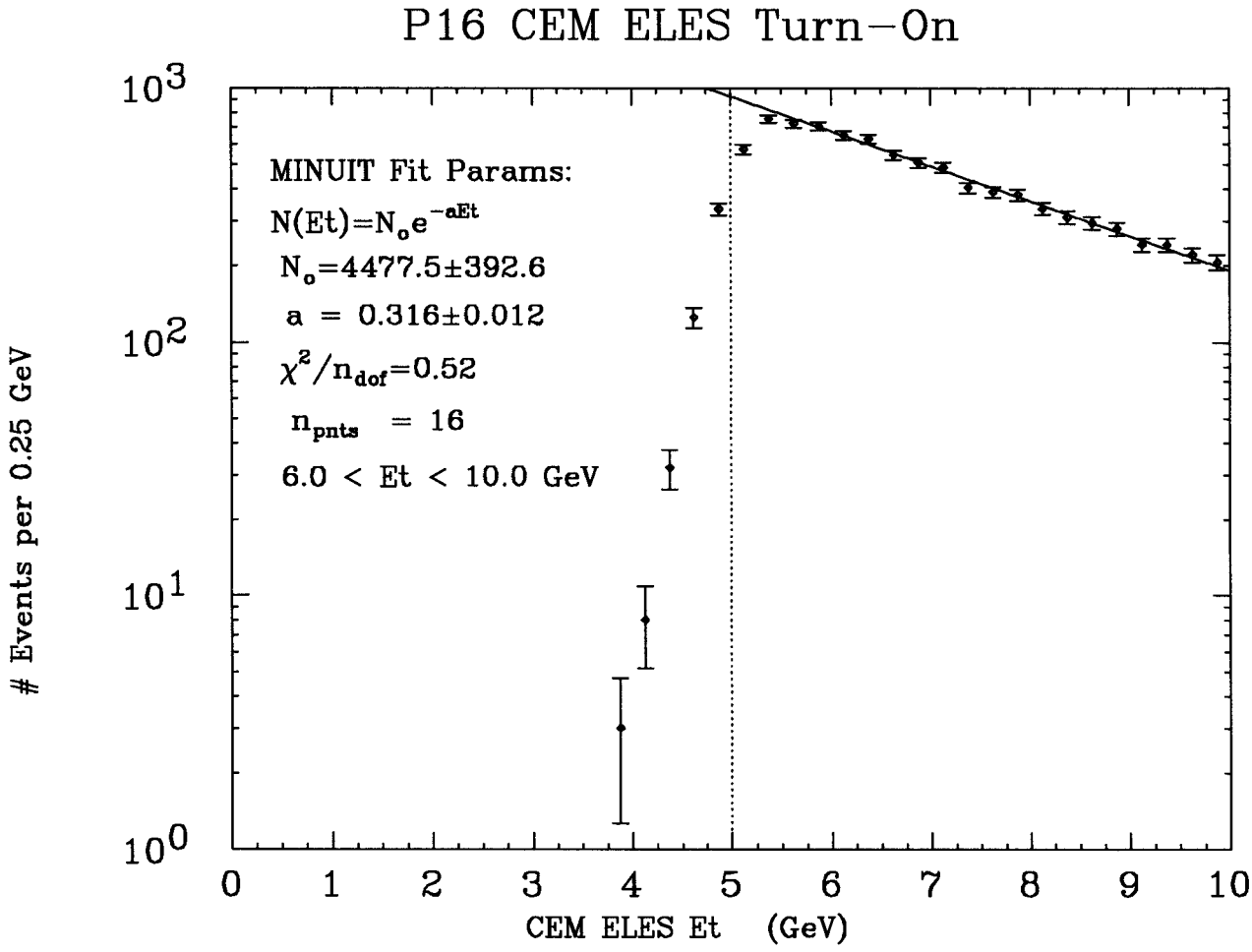


**Figure 5.1**: Number of 'photons' seen in the 16 $GeV$ photon sample as a function of $E_T$. For $E_T$ values above 6 $GeV$, the spectrum fits nicely to an exponential. The dramatic drop in events below 6 $GeV$ is presumably due to inefficiencies in the clustering algorithm since it has an $E_T$ threshold of 5 $GeV$.

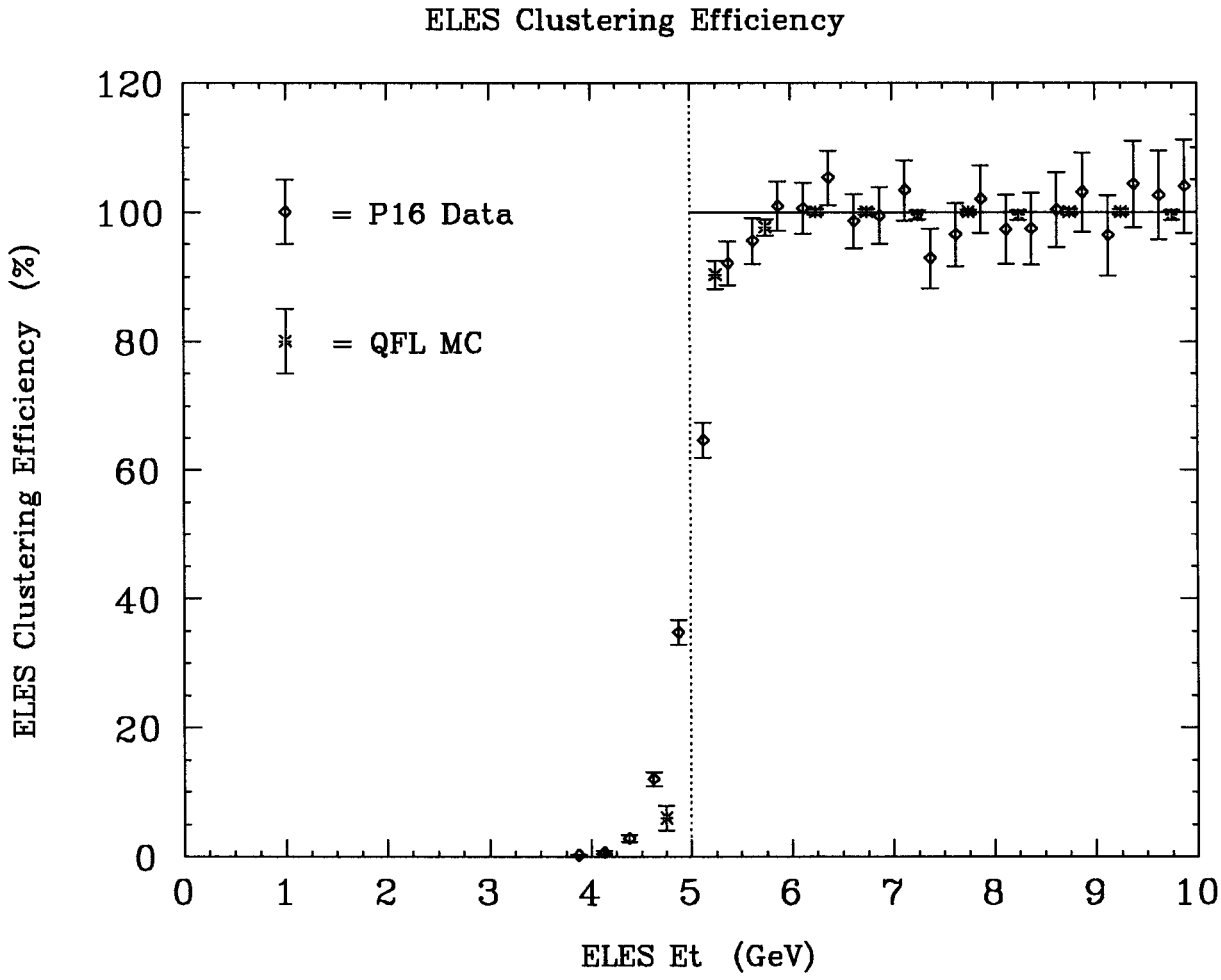


**Figure 5.2**: Clustering efficiency in CEM as a function of cluster $E_T$.

# Chapter 6

# Monte Carlo Studies of $W\gamma$ and $Z\gamma$ Processes

The Standard Model predictions for the production cross sections and event yields for $W\gamma$ and $Z\gamma$ processes are determined using Monte Carlo $W\gamma$ and $Z\gamma$ data samples generated by the Baur Monte Carlos [29, 30] and run through a CDF detector simulation. The acceptance, i.e. the fraction of diboson events we expect to observe based on detector geometry and event kinematics, which is needed for extracting the experimental cross sections for each process is also simultaneously determined.

This chapter discusses the Baur Monte Carlo generator and the detector simulations used to generate the event samples. Also presented are the acceptances, the predicted cross sections, event yields, and the associated systematic uncertainties.

## 6.1 Baur Event Generator

The Baur $W\gamma$ and $Z\gamma$ Monte Carlo event generators perform complete helicity calculations of all the tree-level Feynman diagrams shown in Figures 2.1 and 2.4 and have the ability to simulate the decay of the final state $W/Z$ bosons into the electron, muon or tau channels. The kinematic phase space is done using the VEGAS adaptive multi-dimensional integration code [31]. The default set of structure functions used in this analysis are MRSD$-'$ [33], which are found to best match the $W$ decay asymmetry at CDF [35]. The Monte Carlos include all parton-parton luminosities, and for $W\gamma$, the Cabibbo-Kobayashi-Maskawa quark-mixing matrix elements [34]. Contributions from higher-order QCD processes such as $q + \overline{q} \rightarrow g + V + \gamma$ and $q + g \rightarrow q + V + \gamma$ are approximated by a "K-factor" of $[1 + \frac{8\pi}{9}\alpha_s(M_V^2)] \approx 1.35$ [36], where $V = W$ or $Z$ and $\alpha_s(M_V^2)$ is the strong coupling constant evaluated at $Q^2 = M_V^2$. The analysis of the Baur samples includes $P_T$-boosting of the $W+\gamma$ and $Z+\gamma$ systems according to the measured $P_T$ distributions of the $W$ and $Z$ at CDF.

Typical event samples generated by the Baur Monte Carlo programs have of order 500,000 "weighted" events, where the weight of the event is the probability that kinematic features of that event will occur. These very large samples are generated for specific choices of anomalous couplings. Loose geometrical and kinematic selection requirements are made (with respect to the actual analysis requirements) on the leptons and photons in the generation process. The requirements are a minimum photon $E_T$ and muon

$P_T$ of 1 $GeV$, a minimum lepton-photon separation of $\Delta R_{l\gamma} > 0.3$, and a maximum pseudorapidity for the photon and muon of 6.

## 6.2 Detector Simulations

The four-vector information associated with the final state particles from the Baur Monte Carlos are used as input information for a fast Monte Carlo simulation of the CDF detector [13, 39], which parameterizes details of muon, electron, missing $E_T$ and photon responses in the CDF detector. The detector simulations include all detector resolutions and relevant geometrical information. Note that the use of detector resolutions in the analysis of the Baur generated events is the reason why loose cuts are used in the actual generation procedure; it is conceivable that acceptance biases might arise due to the finite resolutions and vertex smearing, and generating events well below the final sets of kinematic and geometrical cut thresholds avoids these potential biases. The use of the fast Monte Carlo detector simulation provides the final kinematic and geometrical acceptances for $W\gamma$ and $Z\gamma$ events, and the predicted cross section times branching ratio after all analysis cuts. The number of events we expect to observe is calculated by multiplying the cross section by the integrated luminosity of the $W$ and $Z$ samples. About 50K Monte Carlo events pass all the event selection criteria after running the fast Monte Carlo simulation. Appendix D discusses the methodology and details of determining the predicted cross sections after all analysis cuts are made in the detector parameterization

as well as some details about the acceptance calculation, which is discussed in Section 6.3.

Cross-checks are done on the fast Monte Carlo results using the QFL detector simulation (described in Sec. 5.2). The ISAJET Monte Carlo [38] is used to produce the underlying event as well as to produce an event sample in the proper format which can be accessed by QFL. The QFL results are all consistent with the fast detector simulation. All of these results are summarized in Section 6.4.

## 6.3 Acceptances

The total acceptance for $W\gamma$ events can be represented as

$$A_{W\gamma} = A_W \cdot f^{\gamma}_{W\ cem} \cdot A^{\gamma}_{cem} \tag{6.1}$$

In this equation, $A_W$ is the fraction of all muon $W\gamma$ events where the muon is in the CMU and CMP fiducial regions and for which the muon has $P_T > 20\ GeV/c$, $\not\!\!E_T > 20\ GeV$, and $M_T^W > 40\ GeV/c^2$. The variable $f^{\gamma}_{W\ cem}$ is the fraction of all muon $W\gamma$ events in which the photon is confined within the central region of the detector (CEM), and $A^{\gamma}_{cem}$ is the fraction of all central photons which can be detected using the CDF detector. This includes photons that have $E_T > 7\ GeV$ and are separated from the muon by $\Delta R > 0.7$.

The product of these terms gives the total probability that a muon $W\gamma$ event will be detected, based on the geometric features of the CDF detector and basic kinematic properties of these types of events.

For $Z\gamma$ events, a simple-minded expression for the overall acceptance is

$$A_{Z\gamma} = A_Z \cdot f^{\gamma}_{Z\ cem} \cdot A^{\gamma}_{cem} \tag{6.2}$$

The terms in this equation are similar to those in the previous equation for $W\gamma$ events, but the total acceptance for the $Z$, $A_Z$, is more complicated because there are two muons. In general $A_Z$ is the fraction of all muon $Z\gamma$ events in which we are able to detect both muons and for which the muon $P_T > 20\ GeV/c$ and the dimuon invariant mass is $65 < M_{\mu^+\mu^-} < 115\ GeV/c^2$. Further details of the $Z$ acceptance can also be found in Appendix D. The term $f^{\gamma}_{Z\ cem}$ is the fraction of $Z\gamma$ events where the photon is in the central part of the detector, and $A^{\gamma}_{cem}$ is the fraction of central photons that can be detected using the CDF detector. Again, this includes photons that have $E_T > 7\ GeV$ and are separated from both muons by $\Delta R > 0.7$.

Tables 6.1 and 6.2 summarize all the relevant acceptances needed for the $W\gamma$ and $Z\gamma$ analyses. They have been determined by running the fast detector simulation on Baur Monte Carlo data.

| Term | Acceptance value (%) |
|---|---|
| $A_W$ | $11.64 \pm 0.04$ |
| $A^{\gamma}_{W\ cem}$ | $77.02 \pm 0.07$ |
| $f^{\gamma}_{W\ cem}$ | $47.80 \pm 0.02$ |
| $A^{total}_{W\gamma}$ | $4.28 \pm 0.01$ |

**Table 6.1**: Acceptances needed for $W\gamma$ analysis.

| Term | Acceptance value (%) |
|---|---|
| $A_Z$ | $14.45 \pm 0.09$ |
| $A^{\gamma}_{Z\ cem}$ | $76.57 \pm 0.08$ |
| $f^{\gamma}_{Z}$ | $52.52 \pm 0.03$ |
| $A^{total}_{Z\gamma}$ | $5.81 \pm 0.01$ |

**Table 6.2**: Acceptances needed for $Z\gamma$ analysis.

### 6.3.1 Acceptance $\times$ Efficiency

The total acceptances discussed above give the probability of detecting $W\gamma$ or $Z\gamma$ events based on the overall detector geometry and the main kinematic cuts required of these events. In Chapter 5, the efficiencies of the individual selection requirements on the muon(s) and the photon were given. The efficiency of a specific selection requirement gives the probability of a muon or photon passing that requirement. It follows that the product of the total acceptance and all the selection efficiencies is the probability of observing a $W\gamma$ or $Z\gamma$ event using the selection criteria discussed in Chapters 4 and 5. This probability is crucial in the measurement of a cross section.

For $W\gamma$ events, the acceptance $\times$ efficiency term can be written as

$$A_{W\gamma} \cdot \epsilon_{W\gamma} = A^{total}_{W\gamma} \cdot (\epsilon_{zvx} \cdot T \cdot \epsilon^{\mu} \cdot \epsilon^{\gamma}) \tag{6.3}$$

| Sample | $A \cdot \epsilon$ (%) |
|---|---|
| $W\gamma$ | $2.3 \pm 0.1$ |
| $Z\gamma$ | $3.0 \pm 0.1$ |

**Table 6.3**: Acceptance $\times$ efficiency values.

where $\epsilon_{zvx}$ is the probability of the events being within 60 cm of the center of the detector (along the beamline), $T$ is the product of the muon trigger efficiencies for each of the three levels, $\epsilon^{\mu}$ is the overall muon detection efficiency (see Table 5.1), and $\epsilon^{\gamma}$ is the overall photon detection efficiency (see Table 5.6).

Similarly for $Z\gamma$ events, the acceptance $\times$ efficiency term can be written as

$$A_{Z\gamma} \cdot \epsilon_{Z\gamma} = A_{Z\gamma}^{total} \cdot (\epsilon_{zvx} \cdot T \cdot \epsilon^{\mu_1} \cdot \epsilon^{\mu_2} \cdot \epsilon^{\gamma}) \tag{6.4}$$

The difference here is that there is a second muon term, $\epsilon^{\mu_2}$. This efficiency consists of the product of the minimum ionizing efficiencies and the track-finding efficiency. Table 6.3 lists the acceptance $\times$ efficiency products for both $W\gamma$ and $Z\gamma$ processes..

## 6.4 Standard Model Event and $\sigma * BR$ Predictions

The fast detector simulation program is run on the Baur generated $W\gamma$ and $Z\gamma$ event samples. All of the selection criteria for both muons and photons, as described in Chapter 4, are made on the Baur samples, and the number of events left over after selection cuts gives predictions for both the production cross section times branching ratio after all analysis cuts and the number of events the SM predicts we should see at CDF. The

| $W\gamma$ | $\sigma \cdot BR(W\gamma \to \mu\nu_\mu\gamma)$ $(pb)$ | $N_{SM}^{W\gamma}$ (Fast MC) | $N_{SM}^{W\gamma}$ (QFL) |
|---|---|---|---|
| | $18.5 \pm 0.1 \pm 2.8$ | $7.9 \pm 0.7 \pm 1.4$ | $8.6 \pm 0.8$ |
| $Z\gamma$ | $\sigma \cdot BR(Z\gamma \to \mu^+\mu^-\gamma)$ $(pb)$ | $N_{SM}^{Z\gamma}$ (Fast MC) | $N_{SM}^{Z\gamma}$ (QFL) |
| | $4.8 \pm 0.02 \pm 0.6$ | $2.8 \pm 0.2 \pm 0.3$ | $3.0 \pm 0.3$ |

**Table 6.4**: The SM predicted cross section times branching ratio and number of events for $W\gamma$ and $Z\gamma$ processes, as obtained from the fast Monte Carlo CDF detector simulation. The number of predicted events from the QFL detector simulation is also shown. The number of events has been scaled to the total integrated luminosity of the $W$ and $Z$ samples, $18.6 \pm 0.7$ $pb^{-1}$.

predicted number of events is obtained by scaling the fast Monte Carlo result by the total integrated luminosity of the inclusive $W$ and $Z$ muon samples in the data. The Monte Carlo results are shown in Table 6.4. The first uncertainty listed is the statistical uncertainty and the second is the systematic uncertainty (described in Sec. 6.5). Also shown in Table 6.4 is the predicted number of events, with the statistical uncertainties, after using the QFL detector simulation on Baur data samples. The QFL results provide a cross-check to the fast Monte Carlo results. The following section will describe how the systematic uncertainty is obtained for the Baur + fast Monte Carlo predictions.

## 6.5 Systematic Uncertainties on Monte Carlo Predictions

Several studies were done to determine the systematic uncertainty on the predicted cross sections and number of events listed in the previous section. The contributions to the systematic uncertainties include the difference in number of predicted events using the

fast Monte Carlo simulation and QFL, the choice of structure functions, the choice of the $Q^2$ of the interaction, and the $P_T$ boost of the diboson system. The results from each contribution are summarized in Table 6.5.

### 6.5.1 Effect of Structure Functions

To evaluate the uncertainty in the Monte Carlo predictions due to structure function choice, five different sets of structure functions are used. The five sets are HMRS-B [40], MRS S0′ [41], MRS D0′ [33], CTEQ 2pM [42] and the default MRS D−′. Baur $W\gamma$ and $Z\gamma$ samples are generated for each set of structure functions. The $W\gamma$ and $Z\gamma$ fast Monte Carlo simulations are run on each sample and the SM predictions for the number of events and cross section times branching ratio are recorded. The systematic error is taken to be the largest difference between the results from any two structure function sets. The largest difference for both the number of $W\gamma$ and $Z\gamma$ events is between HMRSB and MRS S0′. For $W\gamma$ it is 1.0 events, which represents a 13.0% uncertainty in the SM prediction of 7.9 events (based on MRS D−′). For $Z\gamma$ the number of events vary by 0.2 events, which represents an 8.2% uncertainty in the 2.8 events predicted by the SM. The largest difference for the cross section is 2.3 *pb* for $W\gamma$ and 0.6 *pb* for $Z\gamma$.

### 6.5.2 Effect of $Q^2$

The $Q^2$ of the $W\gamma$ and $Z\gamma$ processes refers to the four-momentum of the intermediate $W$ or $Z$ boson in Figures 2.1c,d and 2.4c,d, respectively. The default values used for $Q^2$ are the mass of the $W$ squared $((80.2\ GeV/c^2)^2)$ and mass of the $Z$ squared $((91.1\ GeV/c^2)^2)$

for the $W\gamma$ and $Z\gamma$ Monte Carlos, respectively. Two other values are used, $4M_V^2$ and $M_V^2/4$, where $V = W$ or $Z$, to determine the effect that $Q^2$ have on the theoretical predictions. The results for $W\gamma$ are differences of 0.06 events and 0.2 *pb* for cross sections, while for $Z\gamma$ the differences are 0.03 events and 0.09 *pb*. These are small systematic uncertainties.

### 6.5.3 Effect of $P_T$-Boosting

Currently no experimental measurements of the $P_T$ spectra of the $W+\gamma$ or $Z+\gamma$ systems exist. However, CDF has measured the $P_T$ spectra of the $W$ and $Z$ bosons [43], and the $d\sigma/dP_T(W/Z)$ distributions agree well with theoretical predictions [44]. It is reasonable to make the assumption that the expected shapes of the $P_T$ distributions for $W/Z + \gamma$ are similar to the shape of the $W/Z$ $P_T$ distributions since most of the photons in the diboson event samples have $E_T$ values which are fairly low (i.e. below 10 $GeV/c$).

In order to determine how the predicted cross sections and event yields vary with $P_T$ boosts of the $W\gamma$ or $Z\gamma$ systems, the Monte Carlo $P_T(V_l + \gamma)$ distributions are varied within $\pm 1\sigma$ limits allowed by the fit to the shape of the $d\sigma/dP_T(W/Z)$ distributions. Four $P_T$-boost values are used with the default structure function and $Q^2$ choices to calculate the predicted cross sections and number of events. The $P_T$ boosts are (a) "hard" $(+1\sigma)$, (b) "soft" $(-1\sigma)$, (c) nominal, and (d) no $P_T$ boost at all. The $W\gamma$ cross section varies by 1.6 *pb* and the number of events varies by 0.6. The $Z\gamma$ cross section varies by 0.09 *pb* and the number of events varies by 0.04.

| Effect | $\sigma \cdot BR(W\gamma \rightarrow \mu\nu_\mu\gamma)$ $(pb)$ | $N_{SM}^{W\gamma}$ | $\sigma BR(Z\gamma \rightarrow \mu^+\mu^-\gamma)$ $(pb)$ | $N_{SM}^{Z\gamma}$ |
|---|---|---|---|---|
| $N^{FMC} - N^{QFL}$ | — | 0.7 | — | 0.2 |
| SF | 2.3 $pb$ | 1.0 | 0.6 $pb$ | 0.2 |
| $P_T$-Boost | 1.6 $pb$ | 0.6 | 0.09 $pb$ | 0.04 |
| $Q^2$ | 0.2 $pb$ | 0.06 | 0.09 $pb$ | 0.03 |
| Sum in Quadrature | 2.8 $pb$ | 1.4 | 0.6 $pb$ | 0.3 |

**Table 6.5**: The systematic variations in the SM predicted cross section times branching ratio and number of events for $W\gamma$ and $Z\gamma$ processes, as obtained from the fast Monte Carlo CDF detector simulation.

# Chapter 7

# Background Determination for $W\gamma$ and $Z\gamma$ Processes

The $W\gamma$ and $Z\gamma$ event samples consist of 7 and 4 events, respectively, after all selection cuts are made. However, not all of those events are the result of the processes represented by the Feynman diagrams shown in Chapter 2. Some fraction of the events are due to other processes which mimic $W\gamma$ and $Z\gamma$ events and ultimately pass all of the selection cuts. In order to calculate production cross sections for diboson events, such 'background' events need to be subtracted from the event samples. This chapter discusses the estimation of possible types of background for the diboson event samples.

## 7.1 QCD Backgrounds

The largest background contribution for both $W\gamma$ and $Z\gamma$ events comes from $W$ and $Z$ events which contain jets in the central region of the detector. It is possible for jets to be misidentified as photons, giving the illusion that the $W+$ jets and $Z+$ jets events are really diboson events. For example, a jet may have fragmented into a leading $\pi^0$ or $\eta^0$, which then decay into two photons. If one of the photons goes into a crack in the calorimeter or the two photons are close enough together so that the separate showers in the CES cannot be resolved, the event will pass the single photon selection cuts and will be in the final sample. An estimate of the probability of jets being misidentified as single, isolated photons, $P(j \rightarrow \gamma)$, as a function of photon $E_T$, is needed in order to make an estimate of this type of background in the $W$ and $Z$ samples. The probabilities are determined from an independent sample of jets. The jet-finding algorithm that is used on the data is discussed in detail in Appendix C.

A 16 $GeV$ isolated photon sample which is created by specially designed level 2 and level 3 triggers is used for this study. The events in this sample have photon-like objects which are accepted by the triggers, and jets which have recoiled off of the trigger 'photons'. At level 2, events are kept if there is a central ($|\eta| < 1.19$) EM cluster of energy above 16 $GeV$ which has a ratio of electromagnetic to total $E_T$ of 0.125 or less. At level 3, the events which pass the level 2 requirements are required to be in the fiducial region defined by the CES positions $|x_{wire}| < 17.5$ cm and 14 cm $< |z_{strip}| <$ 217 cm.

The events are also required to have a total excess $E_T$ in a cone of $\Delta R = 0.7$, centered on the energy cluster, of less than 4 $GeV$, not counting the EM cluster itself.

The QCD background analysis starts with recording all central EM energy clusters and central jets *not* associated with the energy cluster or jet that passed the trigger requirements. Jets that are not involved in the trigger decision are called 'extra jets'. If the objects which actually triggered the event are kept in the analysis a large bias would exist due to fact that photon-like objects are pre-selected. A jet cone size of 0.7 in $\Delta R$ is used in the study. Because any overlap between the jets used in the background analysis and trigger jets is to be avoided, an additional separation cut of $\Delta R \geq 1.4$ is required between the jets which triggered the event and the extra jets, as well as between the energy cluster associated with the trigger jet and the extra, central EM energy clusters in the event. For all CEM clusters which pass these requirements, all of the photon selection cuts described in Chapter 4 are applied. These 'tight' energy clusters are used in the final background estimation. Table 7.1 shows the number of tight CEM clusters and extra jets which pass these selections. Note that four $E_T$ bins are used in this analysis; 7-11, 11-15, 15-19, and $\geq 19$ $GeV$. One can also refer back to Table 4.2 to see how many CEM clusters in the 16 $GeV$ photon sample survive each individual photon cut.

The 16 $GeV$ photon data contains an excess of prompt, non-leading photons compared to QCD jet data because of the trigger requirements. It is expected that for prompt, single photon+jet events, the jet recoiling against the photon is predominantly a quark jet, at least in the low-$E_T$ region [48]. Photons which are the result of quark bremmstrahlung

| $E_T$ Bin (GeV) | Tight CEM | Extra Jets |
|---|---|---|
| 7-11 | 90 | 70795 |
| 11-15 | 45 | 37416 |
| 15-19 | 27 | 27104 |
| 19+ | 54 | 66744 |
| 7+ | 216 | 202059 |

**Table 7.1**: Total number of tight CEM clusters and extra jets per $E_T$ bin in the 16 $GeV$ photon (P16) sample.

| $E_T$ Bin (GeV) | Num. of $\gamma \pm$ (stat) $\pm$ (sys) | Num. of background $\pm$ (stat) $\pm$ (sys) |
|---|---|---|
| 7-11 | $33.8 \pm 14.9 \pm 13.5$ | $56.2 \pm 15.6 \pm 13.5$ |
| 11-15 | $30.2 \pm 9.1 \pm 5.7$ | $14.8 \pm 8.2 \pm 5.8$ |
| 15-19 | $18.2 \pm 6.8 \pm 3.4$ | $8.8 \pm 6.1 \pm 3.4$ |
| 19+ | $44.8 \pm 12.8 \pm 15.9$ | $9.2 \pm 11.3 \pm 15.9$ |
| 7+ | $127.0 \pm 22.7 \pm 38.7$ | $89.0 \pm 21.8 \pm 38.7$ |

**Table 7.2**: Number of real photons and background in the background analysis sample after all photon cuts, per $E_T$ bin.

can then result. Also, there are diphoton events in which one photon passes the trigger requirements and the other passes the analysis requirements.

In order to make an estimate of how often $\pi^0$ and $\eta^0$ particles are misidentified as single photons we must remove the number of single, prompt photons from the total number of tight CEM clusters. The photon subtraction is accomplished using an algorithm [59] which is summarized in Appendix E. The method uses the average of the CES strip and wire $\chi^2$ values and the CEM cluster $E_T$. It provides estimates for the number of single photons and photon background candidates, as well as statistical and systematic errors on those estimates. Table 7.2 shows these estimates for the photon jet sample.

| $E_T$ Bin (GeV) | Ratio $\pm$ (stat) $\pm$ (sys) | # $W$ Jets | # $Z$ Jets |
|---|---|---|---|
| 7-11 | 0.00079 $\pm$ 0.00021 $\pm$ 0.00019 | 1857 | 86 |
| 11-15 | 0.00040 $\pm$ 0.00024 $\pm$ 0.00015 | 685 | 31 |
| 15-19 | 0.00032 $\pm$ 0.00022 $\pm$ 0.00013 | 288 | 28 |
| 19+ | 0.00014 $\pm$ 0.00017 $\pm$ 0.00024 | 412 | 35 |
| 7+ | 0.00062 $\pm$ 0.00011 $\pm$ 0.00020 | 3242 | 180 |

**Table 7.3**: Ratios of $N_i^{back}$ to $N_i^{XJ}$ using the $W\gamma/Z\gamma$ photon cuts, and number of jets in the inclusive $W$ and $Z$ samples.

The probability of misidentifying a jet as a photon, as a function of "photon" $E_T$, is defined as the estimated number of *background* events in some $E_T$ bin $i$, $N_i^{back}$, from Table 7.2 divided by the total number of extra jets in bin $i$, $N_i^{XJ}$, from Table 7.1,

$$P_i\ (j \rightarrow \gamma) = \frac{N_i^{back}}{N_i^{XJ}} \tag{7.1}$$

The ratios for each of the four $E_T$ bins are shown in Table 7.3 and the distribution is plotted in Figure 7.1. Also listed are the number of jets in the inclusive $W$ and $Z$ samples.

These ratios are multiplied by the number of jets in $E_T$ bin $i$ from the inclusive $W$ and $Z$ samples to get the number of QCD background events in bin $i$. Summing all four bins together gives the total QCD background for the $W\gamma$ and $Z\gamma$ samples. The results are shown in Table 7.4.

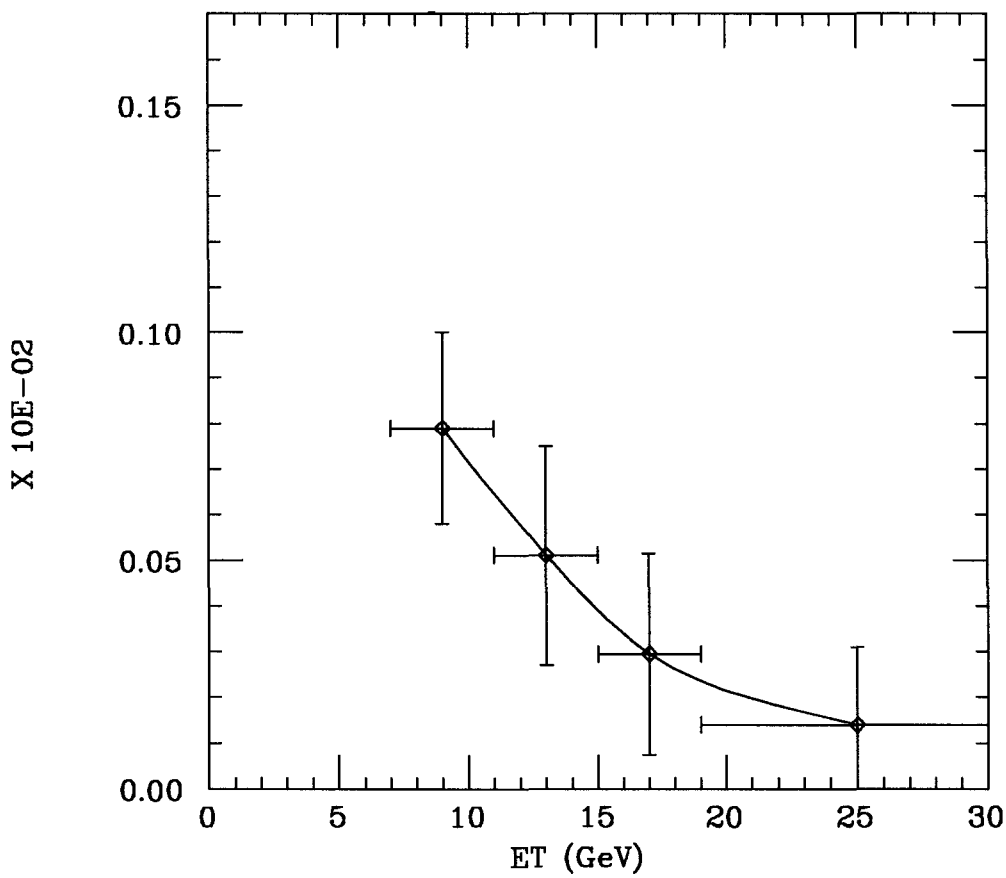


**Figure 7.1**: Plot of $P(j \rightarrow \gamma)$ (after the photon subtraction) as a function of $E_T$ in the 16 $GeV$ photon sample.

| $E_T$ Bin (GeV) | $W\gamma$ QCD $\pm$ (stat) $\pm$ (sys) | $Z\gamma$ QCD $\pm$ (stat) $\pm$ (sys) |
|---|---|---|
| 7-11 | $1.5 \pm 0.4 \pm 0.3$ | $0.07 \pm 0.02 \pm 0.02$ |
| 11-15 | $0.2 \pm 0.2 \pm 0.1$ | $0.01 \pm 0.01 \pm 0.01$ |
| 15-19 | $0.1 \pm 0.04 \pm 0.04$ | $0.01 \pm 0.01 \pm 0.01$ |
| 19+ | $0.1 \pm 0.04 \pm 0.04$ | $0.01 \pm 0.001 \pm 0.01$ |
| 7+ | $1.9 \pm 0.5 \pm 0.4$ | $0.10 \pm 0.03 \pm 0.04$ |

**Table 7.4**: QCD background in $W\gamma$ and $Z\gamma$ samples for each $E_T$ bin.

## 7.2 Tests of QCD Background Estimates

Several studies were done to make sure the QCD background estimates are reliable. One study dealt with seeing how the background estimates change when the photon cuts are varied. The photon cuts are designed to try and maximize the number of true diboson events and minimize the number of background events in the final sample. If the cuts are made less stringent, background events which were once forced out of the sample now enter the sample. The increased number of background events increases the size of the sample. A reliable background estimate should be able to predict the increase. The $W\gamma/Z\gamma$ signal in each $E_T$ bin, however, remains virtually the same as cuts are loosened. For instance, loosening the $ISO4$ and $\Sigma PT4$ cuts by a factor of 2 causes the predicted signal to increase by about 5%. Doing the same thing on the 16 $GeV$ photon sample increases the QCD background estimate by a factor of about 2-2.5. Figure 7.2 shows the $W\gamma$ signal results from three cases: A) the standard photon selection described in Ch. 4, B) isolation cuts loosened to $ISO4 < 0.5$, $Lshr < 1.5$, and no $\Sigma P_T$, and C) *only* the $ISO4$ and $\Sigma PT4$ cuts, without $Had/EM$, $Lshr$, or CES $\chi^2$ cuts. This particular study used the electron sample since it contains larger statistics. The QCD background

is determined for each case using the method described above, and includes the photon subtraction. As can be seen in Figure 7.2, the size of the signal in each $E_T$ bin for each set of cuts agrees well with the others within the statistical uncertainties. A similar example is discussed in Ch. 4. After relaxing the minimum separation of the muon and photon in the $W$ sample from $\Delta R > 0.7$ to 0.4, one expects more events to enter the sample. The new events are a mix of $W\gamma$ (mainly muon bremmstrahlung events) and background events. A total of 4 events are observed, which is consistent with the Monte Carlo plus background prediction of $6.1 \pm 0.8$ events. These studies suggest that the QCD background allowed into the diboson samples by loosening photon selection cuts is accounted for by the background estimation method.

The QCD photon background analysis is based on the assumption that the probability of jets being misidentified as photons in some $E_T$ bin $i$ is the same in the 16 $GeV$ photon sample as in the inclusive $W$ and $Z$ samples. That is,

$$P_i^V(j \to \gamma) = P_i^{P16}(j \to \gamma) \tag{7.2}$$

where $V = W$ or $Z$. To test this assumption the probabilities obtained from the photon jet sample are compared to the following ratio in the combined muon and electron $W$ samples (for added statistics):

$$P_i^W(j \to \gamma) = \frac{N_i^{observed} - N_i^{SM}}{N_i^{W\ jets}} \tag{7.3}$$

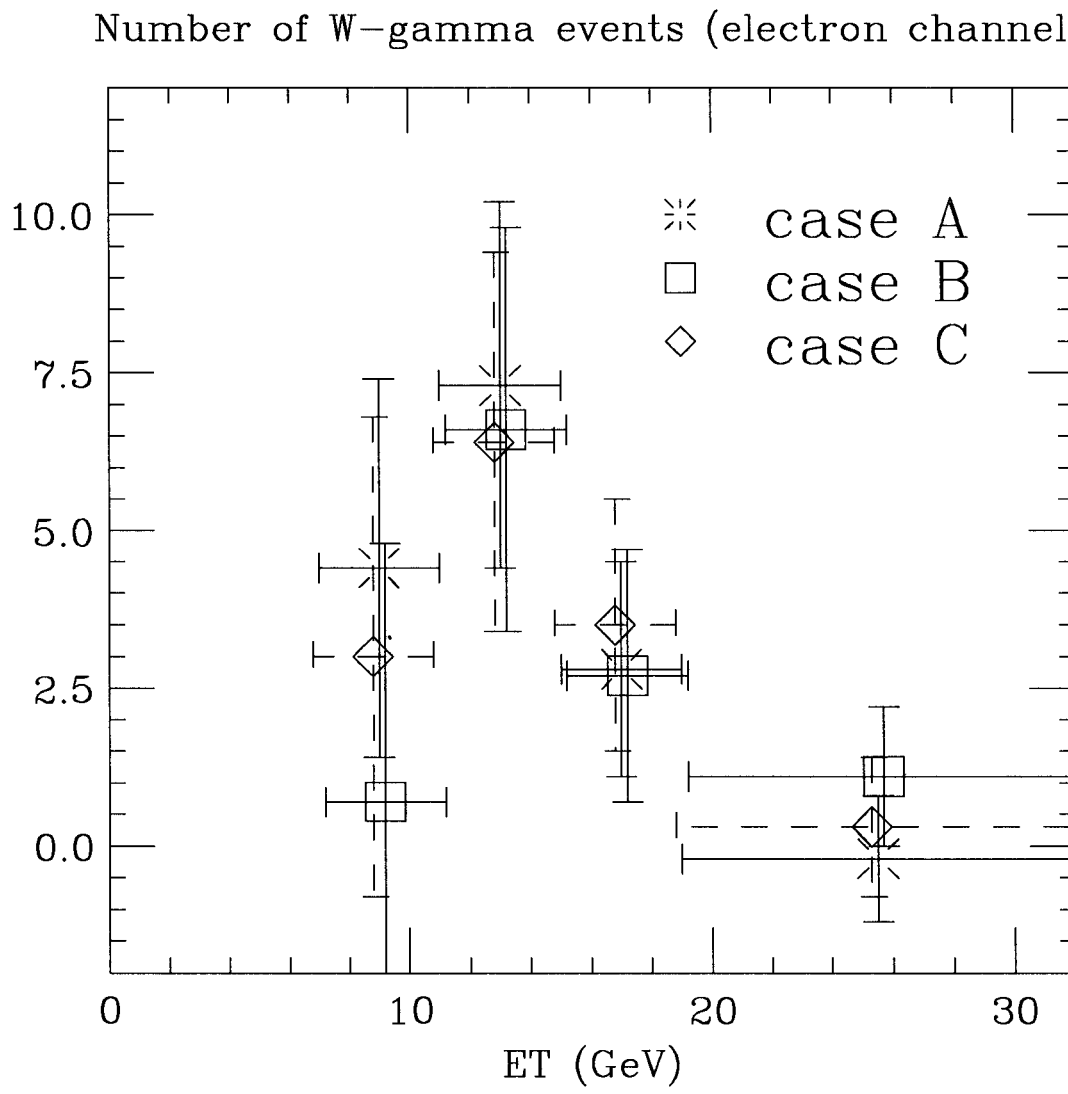


**Figure 7.2**: Comparison of the number of $W\gamma$ events (signal) in the electron channel. Case A uses the standard set of photon selections, case B uses loosened isolation cuts, and case C uses only isolation cuts. They are all consistent with each other within statistical uncertainties.

where $N_i^{observed}$ is the combined number of events in the muon and electron $W\gamma$ sample in the $E_T$ bin $i$, $N_i^{SM}$ is the SM prediction for the number of electron $W\gamma$ events in the $E_T$ bin $i$, and $N_i^{W\ jets}$ is the combined number of jets in the inclusive $W$ samples in the $E_T$ bin $i$. It is *assumed* that subtracting off the SM number of $W\gamma$ events removes the real photon contribution from the samples and leaves just the number of background events in the samples. Figure 7.3a shows a comparison of $P_i^W(j \rightarrow \gamma)$, as defined above in Equation (7.3), to $P_i^{P16}(j \rightarrow \gamma)$. Note that the values of $P_i^{P16}(j \rightarrow \gamma)$ are determined *without* using the background subtraction. Figure 7.3b, on the other hand, uses the photon subtraction method in obtaining $P_i^{P16}(j \rightarrow \gamma)$, and compares it to the same ratio $P_i^W(j \rightarrow \gamma)$ as in Figure 7.3a. As can be seen, the two sets of photon subtracted ratios (Fig. 7.3b) agree better with each other within errors. This result supports the assumption that the fragmentation probabilities between the inclusive $W$ and background samples are consistent with each other, though there are large statistical errors. It also supports the method used to estimate the QCD backgrounds, i.e. using the photon subtraction is appropriate.

## 7.3 Monte Carlo Estimates of QCD Backgrounds

The QCD background estimates using the 16 $GeV$ photon sample were checked using the VECBOS $W+$ jet Monte Carlo program [49]. We generated VECBOS $W$ + 0, 1, and 2 jets samples which were then fragmented with the HERWIG Monte Carlo [50]. QFL was used as the CDF detector simulation in order to make analysis cuts on the Monte

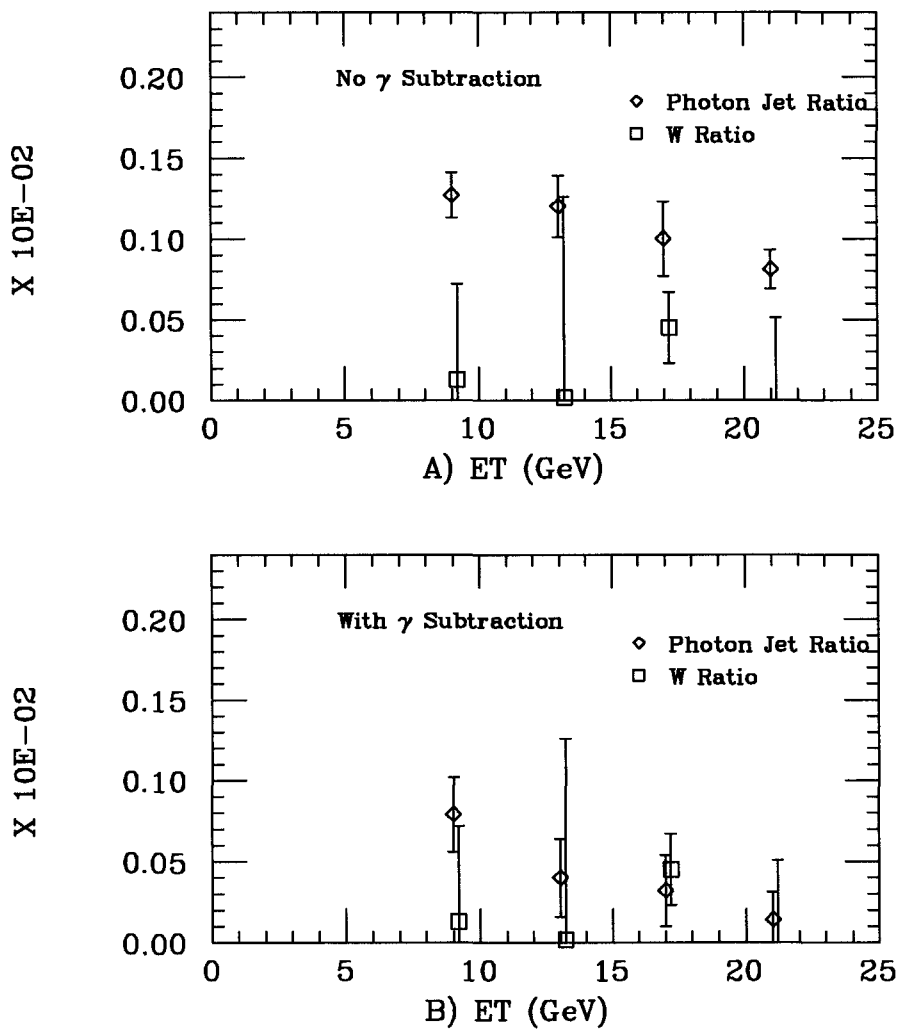


**Figure 7.3**: Comparison of background probabilities between the combined electron and muon $W$ samples and 16 $GeV$ photon sample. Figure A uses no photon subtraction in the photon-jet ratios, while Figure B does use photon subtraction.

Carlo jets samples. A predicted background of $1.7 \pm 1.0$ events is found for the $W\gamma$ sample. This is in good agreement with the estimate from the 16 $GeV$ photon data of $1.9 \pm 0.8$ events. A check of the $Z\gamma$ QCD background result is calculated by scaling the VECBOS $W$ + jet result by the ratio of number of jets in the inclusive $Z$ sample (180 jets) to the total number of jets in the inclusive $W$ sample (3242 jets), or 0.056. This gives $0.10 \pm 0.10$, also in very good agreement with the 16 $GeV$ photon result. Note that the VECBOS results are estimates of the 'direct' QCD background, and does not include contributions from $Z+$ jet events or $W \rightarrow \tau+$ jet events (where $\tau \rightarrow \mu$) which pass $W\gamma$ requirements. The Monte Carlo was used as a check to make sure the background results from the data were reasonable.

A second Monte Carlo was used as a check of the VECBOS results. The Ellis-Kleiss-Stirling (EKS) Monte Carlo [51] was used to generate $W+$ 0, 1, and 2 jets in the electron decay channel. HERWIG fragmentation and the QFL detector simulation were again used. The electron result was $4.6 \pm 0.5$ events. In order to obtain an estimate for the muon channel, this result was scaled by the difference in integrated luminosity between the electron and muon samples (19.3 $pb^{-1}$ for electrons vs 18.6 $pb^{-1}$ for muons) and the ratio of the QCD backgrounds obtained from the 16 $GeV$ photon data ($4.6 \pm 1.9$ events for electrons vs $1.9 \pm 0.8$ events for muons). The EKS-projected QCD background in the muon channel is $1.9 \pm 1.1$ events. Although we did not explicitly generate $W+$ jets samples where the $W$ decays into muons, this result from the EKS Monte Carlo supports the QCD background results from both VECBOS and the 16 $GeV$ photon sample.

## 7.4 Systematic Uncertainties on QCD Background

The systematic uncertainties assigned to the QCD background estimates consist of the systematic uncertainties given by the photon subtraction algorithm, the difference between the background estimates from the 16 $GeV$ photon sample and the VECBOS/HERWIG plus QFL Monte Carlo prediction, and the difference between estimates obtained from the 16 $GeV$ photon data resulting from different bin sizes in $E_T$ (the default binning consists of 4 $GeV$ steps). All of these contributions are added together in quadrature to get the total systematic uncertainty on the QCD background.

To study the variation of the QCD background estimates with $E_T$ bin size, bin sizes of 1, 2, 3, 4, and 5 $GeV$ are used as well as one single bin above 7 $GeV$. Figure 7.4 shows the QCD background estimates for each bin size for the $W$ sample, and Fig. 7.5 shows the same for the $Z$ sample. The systematic uncertainty is chosen to be the maximum difference between any two estimates, which is 0.4 events for the $W$ sample and 0.03 events for the $Z$ sample. The difference between the VECBOS Monte Carlo and photon jet estimates is 0.2 events for the $W$ sample and 0.01 events for the $Z$ sample. The systematic uncertainty from the photon subtraction algorithm is 0.4 events for the $W$ sample and 0.02 events for the $Z$ sample. Added in quadrature these give a total systematic uncertainty on the QCD background of 0.6 events for the $W\gamma$ sample and 0.04 events for the $Z\gamma$ sample. Table 7.5 summarizes each contribution. Thus the final QCD background for $W\gamma$ is $1.9 \pm 0.5(stat) \pm 0.6(syst)$ events, and, for $Z\gamma$, $0.10 \pm 0.03(stat) \pm 0.04(syst)$ events.

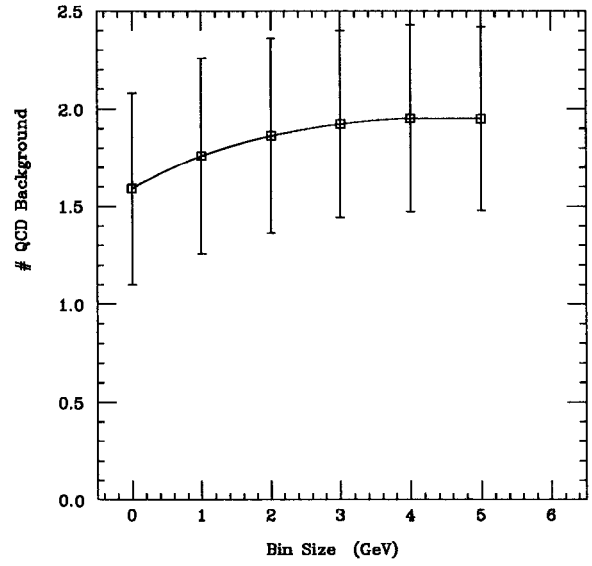


**Figure 7.4**: QCD background predictions in the $W$ sample as a function of bin size. The 0 $GeV$ bin size corresponds to a single bin above 7 $GeV$. The systematic uncertainty associated with this study is the largest difference in predicted background between any two bin sizes.

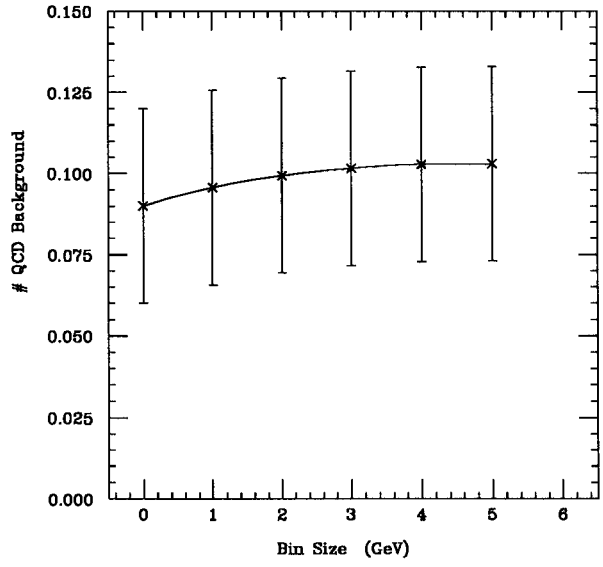


**Figure 7.5**: QCD background predictions in the $Z$ sample as a function of bin size. The 0 $GeV$ bin size corresponds to a single bin above 7 $GeV$. The systematic uncertainty associated with this study is the largest difference in predicted background between any two bin sizes.

| Contribution | # Events ($W$ sample) | # Events ($Z$ sample) |
|---|---|---|
| Bin size | 0.4 | 0.03 |
| Data - MC | 0.2 | 0.01 |
| Photon subtraction | 0.4 | 0.02 |
| Added in quadrature | 0.6 | 0.04 |

**Table 7.5**: List of contributions to the QCD background systematic uncertainty.

## 7.5 Additional Backgrounds in $W\gamma$ and $Z\gamma$ Samples

The jet background is not the only background in the diboson samples. The following sections describe other backgrounds and their estimates for both the $W\gamma$ and $Z\gamma$ samples.

### 7.5.1 Other Backgrounds to $W\gamma$

An additional, significant background for $W$ decays in the muon channel occurs when one of the muons from a $Z \rightarrow \mu^+\mu^-$ event goes outside of the central region ($|\eta| > 1.1$). The tracking efficiency, as was previously shown, starts to fall off in that pseudorapidity region, and what is really a $Z$ decay looks like a $W$ decay. If that event also has a photon in it (i.e. it is a $Z\gamma$ event), the event would appear in the detector as a $W\gamma$ candidate.

To reduce the $Z\gamma$ background to $W\gamma$ samples, events are rejected if they contain additional, isolated tracks with $P_T > 10\ GeV$ and an opposite charge sign to the $W$ decay muon, and also a pair-mass (between the track and the muon) of $40 < M_{\mu-track} < 140\ GeV/c^2$. Tracks that are within $\Delta R < 0.7$ of a hadronic jet ($EM$ fraction less than 0.85) are not considered because $W\gamma+$ jet events are not vetoed in this analysis. The $Z\gamma$ background is estimated by running the $W\gamma$ fast Monte Carlo program on a

sample of Baur generated $Z\gamma$ events. The final result after using the no-track algorithm is $1.14 \pm 0.06(stat) \pm 0.2(syst)$ events. The 15% systematic uncertainty of 0.2 events is added to the one-legged $Z\gamma$ background due to choice of structure functions, $Q^2$ and $P_T$-boosting.

Tau leptons can be produced from $W$ and $Z$ decays, and the $\tau$ can then decay into a muon. Due to this decay channel, there is a non-zero background from events of the type $W\gamma \rightarrow \tau\nu_\tau\gamma$ where the $\tau$ then decays into a muon, thus faking a muon $W\gamma$ event. It is also conceivable to have $Z\gamma$ events where the $Z$ decays into two $\tau$ leptons, and then the $\tau$ leptons decay in such a way that one muon is detected, thus faking a muon $W\gamma$ event. All of these contributions are simulated using the Baur event generators and the fast Monte Carlo. The total contribution of $\tau + \gamma$ to the background is $0.15 \pm 0.01(stat) \pm 0.02(syst)$ events. Again, the systematic uncertainty of 0.02 events is added because of differences in results after varying structure functions, $Q^2$, and $P_T$-boosting. Any contribution of $W \rightarrow \tau\nu_\tau +$ jet, where the $\tau$ decays into a muon and the jet is misidentified as a photon, is already included in the total QCD background and is not considered separately.

### 7.5.2 Other Backgrounds to $Z\gamma$

The process $Z \rightarrow \tau^+\tau^-\gamma$, where the $\tau$ leptons decay into muons, is estimated using Baur-generated samples and the fast Monte Carlo detector simulation. This background is found to be very small, $0.001 \pm 0.0001$, and is negligible. The process $Z \rightarrow \tau^+\tau^- +$ jet, where the jet is misidentified as a photon, is included in the QCD background estimate

| Contribution | # Events ($W\gamma$ sample) | # Events ($Z\gamma$ sample) |
|---|---|---|
| QCD | $1.9 \pm 0.5(stat) \pm 0.6(syst)$ | $0.1 \pm 0.03(stat) \pm 0.04(syst)$ |
| One-legged $Z\gamma$ | $1.1 \pm 0.06(stat) \pm 0.2(syst)$ | — |
| $\tau$ Decays | $0.2 \pm 0.01(stat) \pm 0.02(syst)$ | $0.001 \pm 0.0001(stat)$ |
| Total Background | $3.2 \pm 0.5(stat) \pm 0.6(syst)$ | $0.1 \pm 0.03(stat) \pm 0.04(syst)$ |

**Table 7.6**: Summary of the *total* background for $W\gamma$ and $Z\gamma$.

for the $Z\gamma$ channel. The total background for $Z\gamma$, then, is just the QCD background estimate given above.

## 7.6 Summary of Backgrounds for $W\gamma$ and $Z\gamma$

For $W\gamma$ processes in which the $W$ decays to a muon and neutrino, several separate processes can mimick the signal in the detector. The processes which contribute to these 'background' events include QCD events in which jets are misidentified as single, prompt photons, one-legged $Z\gamma$ events, and events which include $\tau$ leptons which then decay into muons. These contributions to the total background were studied and the results are summarized in Table 7.6.

For $Z\gamma$ processes, the only significant background is the result of QCD processes. The $\tau$ contribution is negligible. The total $Z\gamma$ background is also listed in Table 7.6.

# Chapter 8

# Experimental Results

This chapter presents the experimental results in the muon channel for the cross sections times branching ratios, ratios of cross sections, and limits on anomalous couplings for $W\gamma$ and $Z\gamma$ processes. The limits on anomalous couplings are used to extract limits on electromagnetic moments of the $W$ and $Z$ bosons and form factor energy scales.

## 8.1 Results for $\sigma \cdot BR(W\gamma \rightarrow \mu\nu_\mu\gamma)$ and $\sigma \cdot BR(Z\gamma \rightarrow \mu^+\mu^-\gamma)$

The final muon $W\gamma$ and $Z\gamma$ event samples, for photon $E_T > 7\ GeV$ and muon-photon angular separation $\Delta R > 0.7$, have 7 and 4 events, respectively. From Chapter 7 the total background estimate for the $W\gamma$ sample is $3.2 \pm 0.5\ (stat) \pm 0.6\ (syst)$ events, and for the $Z\gamma$ sample the background is $0.1 \pm 0.03\ (stat) \pm 0.04\ (syst)$ events. Subtracting the background estimates from the total number of events in the diboson samples gives

| Channel | $N_{obs}$ | $\Sigma N_{bkgnd}$ | $N_{signal}$ | $N_{pred}^{SM}$ |
|---|---|---|---|---|
| $\mu\ W\gamma$ | 7 | $3.2 \pm 0.5 \pm 0.6$ | $3.8 \pm 2.6 \pm 0.6$ | $7.9 \pm 0.7 \pm 1.2$ |
| $\mu\ Z\gamma$ | 4 | $0.1 \pm 0.03 \pm 0.04$ | $3.9 \pm 2.0 \pm 0.04$ | $2.8 \pm 0.2 \pm 0.3$ |

**Table 8.1**: Summary of $W\gamma$ and $Z\gamma$ signals, both experimental and SM predicted, for a photon $E_T$ threshold of 7 $GeV$. The first uncertainty is statistical and the second is systematic.

an estimate of the diboson signal. Table 8.1 shows the number of background and signal events as well as the SM signal prediction for both samples. The uncertainties listed in Table 8.1 are statistical and systematic uncertainties, respectively. The statistical uncertainty for the signal estimate is the background statistical uncertainty and the square root of the total number of events in the sample, $\sqrt{N_{obs}}$, added in quadrature. The systematic uncertainty listed for the number of signal events is just the background systematic uncertainty.

The number of signal events, combined with the integrated luminosity of $18.6 \pm 0.7\ pb^{-1}$ and the overall acceptance $\times$ efficiency for $W\gamma$ and $Z\gamma$ processes, can be used to calculate the experimental cross section times branching ratios of the processes with the equations

$$\sigma \cdot BR(W\gamma \rightarrow \mu\nu_\mu\gamma) = \frac{N_{\mu,observed}^{W\gamma} - \Sigma N_{\mu,background}^{W\gamma}}{A_{W\gamma} \cdot \epsilon_{W\gamma} \cdot \int L_\mu dt} \tag{8.1}$$

$$\sigma \cdot BR(Z\gamma \rightarrow \mu^+\mu^-\gamma) = \frac{N_{\mu,observed}^{Z\gamma} - \Sigma N_{\mu,background}^{Z\gamma}}{A_{Z\gamma} \cdot \epsilon_{Z\gamma} \cdot \int L_\mu dt} \tag{8.2}$$

The term $A_{V\gamma} \cdot \epsilon_{V\gamma}$ is the product of all efficiencies and acceptances for a given channel (see Table 6.3) and $\int L_\mu dt$ is the integrated luminosity for the muon data samples. The

| Channel | $\sigma \cdot B_{expt}$ $(pb)$ | $\sigma \cdot B_{pred}^{SM}$ $(pb)$ |
|---|---|---|
| $\mu$ $W\gamma$ | $9.0 \pm 6.3 \pm 1.0$ | $18.5 \pm 0.1 \pm 2.8$ |
| $\mu$ $Z\gamma$ | $6.6 \pm 3.4 \pm 0.4$ | $4.8 \pm 0.02 \pm 0.6$ |

**Table 8.2**: Summary of $\sigma \cdot BR(W+\gamma)$ and $\sigma \cdot BR(Z+\gamma)$ results for the muon sample, using a photon $E_T$ threshold of 7 $GeV$. The first uncertainty on the experimental value is the statistical uncertainty. The second is the systematic uncertainty obtained from background estimates and the integrated luminosity.

measured cross section times branching ratios for the muon channel are $9.0 \pm 6.3$ $(stat) \pm$ 1.0 $(syst)$ $pb$ for $W\gamma$ and $6.6 \pm 3.4$ $(stat) \pm 0.4$ $(syst)$ $pb$ for $Z\gamma$. The experimental and Standard Model predictions for the $W\gamma$ and $Z\gamma$ cross section $\times$ branching ratios in the muon channel are summarized in Table 8.2.

The $W\gamma$ cross section is about $1.5\sigma$ lower, and the $Z\gamma$ cross section about $0.5\sigma$ higher, than the Standard Model. Within the limited statistics, they are both consistent with the Standard Model.

The measured cross section $\times$ branching ratio for $W + \gamma$ and $Z + \gamma$ processes is sensitive to where the minimum photon $E_T$ selection cut is placed because the number of photons in the low $E_T$ region (as photon $E_T \rightarrow 0$) is expected to be much greater than the number of photons with higher $E_T$ values (for instance $E_T > 10\ GeV$). In the Run 1A data we require the minimum photon $E_T$ to be at least 7 $GeV$. The 1988-89 CDF analysis used a minimum photon $E_T$ of 5 $GeV$ [13]. The cross section $\times$ branching ratios for two other minimum photon $E_T$ values, 11 $GeV$ and 15 $GeV$, have been calculated using the Run 1A data. In order to do this the backgrounds and acceptances had to be remeasured for each $E_T$ threshold. The same methods that are used for the 7 $GeV$ measurement are

| Channel | $N_{obs}$ $(E_T^\gamma > 11\ GeV)$ | $\Sigma N_{bkgnd}$ | $N_{signal}$ |
|---|---|---|---|
| $\mu\ W\gamma$ | 3 | $1.9 \pm 0.7 \pm 0.4$ | $1.1 \pm 1.9 \pm 0.4$ |
| $\mu\ Z\gamma$ | 2 | $0.04 \pm 0.02 \pm 0.01$ | $2.0 \pm 1.4 \pm 0.01$ |

**Table 8.3**: Summary of $W\gamma$ and $Z\gamma$ backgrounds and signals for the muon sample. These numbers are based on a photon $E_T$ cut of 11 GeV. The uncertainties are statistical and systematic, respectively.

| Channel | $A_{V\gamma}$ (%) | $A_{V\gamma} \cdot \epsilon_{V\gamma}$ (%) |
|---|---|---|
| $\mu\ W\gamma$ | $3.59 \pm 0.01$ | $2.27 \pm 0.10$ |
| $\mu\ Z\gamma$ | $5.14 \pm 0.12$ | $2.73 \pm 0.12$ |

**Table 8.4**: Summary of $W\gamma$ and $Z\gamma$ acceptances and the product of those acceptances and the overall event selection efficiencies for a photon $E_T$ thresholds of 11 GeV.

used for the 11 and 15 $GeV$ measurements. Tables 8.3 and 8.5 list the number of diboson events remaining after the higher photon $E_T$ cut as well as the background and signal estimates. The total $W\gamma$ and $Z\gamma$ acceptances for each $E_T$ threshold are listed in Tables 8.4 and 8.6. Also listed are the final values for $A_{V\gamma} \cdot \epsilon_{V\gamma}$, where $V = W$ or $Z$.

The $\sigma \cdot BR$ results for minimum photon $E_T$ values of 5, 7, 11 and 15 $GeV$ are listed in Tables 8.7 ($W\gamma$) and 8.8 ($Z\gamma$). Note that the results from the 1988-89 CDF analysis (5 $GeV$) have corrections applied to them in order to compare to the 1992-93 results. The 1988-89 experimental $\sigma \cdot BR$ values have been increased by a factor of 1.1 to account for a

| Channel | $N_{obs}$ $(E_T^\gamma > 15\ GeV)$ | $\Sigma N_{bkgnd}$ | $N_{signal}$ |
|---|---|---|---|
| $\mu\ W\gamma$ | 2 | $1.0 \pm 0.4 \pm 0.4$ | $1.0 \pm 1.5 \pm 0.4$ |
| $\mu\ Z\gamma$ | 1 | $0.02 \pm 0.01 \pm 0.01$ | $1.0 \pm 1.0 \pm 0.01$ |

**Table 8.5**: Summary of $W\gamma$ and $Z\gamma$ backgrounds and signals for the muon sample. These numbers are based on a photon $E_T$ cut of 15 GeV. The uncertainties are statistical and systematic, respectively.

| Channel | $A_{V\gamma}$ (%) | $A_{V\gamma} \cdot \epsilon_{V\gamma}$ (%) |
|---|---|---|
| $\mu\ W\gamma$ | $2.69 \pm 0.01$ | $1.51 \pm 0.06$ |
| $\mu\ Z\gamma$ | $4.19 \pm 0.02$ | $2.26 \pm 0.10$ |

**Table 8.6**: Summary of $W\gamma$ and $Z\gamma$ acceptances and the product of those acceptances and the overall event selection efficiencies for a photon $E_T$ thresholds of 15 GeV.

change in luminosity normalization. The 1988-89 theoretical values are also recomputed using MRS D$-'$ structure functions, since they were originally calculated using HMRSB structure functions.

The uncertainties associated with the values given in Tables 8.7 and 8.8 are the total statistical and systematic uncertainties added in quadrature. Note that the experimental uncertainties are dominated by statistics. For instance, for the 15 $GeV$ measurements, the $W\gamma$ result is based on 2 events and the $Z\gamma$ result is based on 1 event. The theoretical uncertainties are dominated by the systematic effects discussed in Section 6.5, and the magnitude of these systematic uncertainties is taken to be 15%. Figure 8.1 compares the experimental $\sigma \cdot BR$ results to SM expectations as a function of the photon $E_T$ threshold. The smooth (dashed) line in Figure 8.1 is the SM prediction (uncertainty) over the given $E_T$ range. The experimental results are consistent with the SM to within $1.5\sigma$.

## 8.2 Cross Section Ratios

In Chapter 2, cross section ratios are mentioned as another test of the SM. The main benefit of using ratios is that all common efficiencies, acceptances and, most importantly their uncertainties, cancel. For instance, the integrated luminosity used in calculating

| $E_T$ Cut $(GeV)$ | $\sigma \cdot BR(W\gamma)_{expt}$ $(pb)$ | $\sigma \cdot BR(W\gamma)_{SM}$ $(pb)$ |
|---|---|---|
| 5 | $28.5 \pm 25.1$ | $24.7 \pm 3.7$ |
| 7 | $9.0 \pm 6.3$ | $18.6 \pm 2.8$ |
| 11 | $4.8 \pm 8.6$ | $11.6 \pm 1.7$ |
| 15 | $6.8 \pm 10.3$ | $7.7 \pm 1.2$ |

**Table 8.7**: Summary of $\sigma \cdot BR$ results as a function of photon $E_T$ for $W\gamma$ processes. Both experimental and SM results are shown. The large uncertainties on some of the experimental values are dominated by statistics. The uncertainties on the theory predictions are dominated by systematic effects.

| $E_T$ Cut $(GeV)$ | $\sigma \cdot BR(Z\gamma)_{expt}$ $(pb)$ | $\sigma \cdot BR(Z\gamma)_{SM}$ $(pb)$ |
|---|---|---|
| 5 | $18.7 \pm 13.9$ | $6.1 \pm 0.9$ |
| 7 | $6.6 \pm 3.5$ | $4.8 \pm 0.6$ |
| 11 | $3.8 \pm 2.7$ | $3.2 \pm 0.5$ |
| 15 | $2.3 \pm 2.4$ | $2.2 \pm 0.3$ |

**Table 8.8**: Summary of $\sigma \cdot BR$ results as a function of photon $E_T$ for $Z\gamma$ processes. Both experimental and SM results are shown. The large uncertainties on some of the experimental values are dominated by statistics. The uncertainties on the theory predictions are dominated by systematic effects.

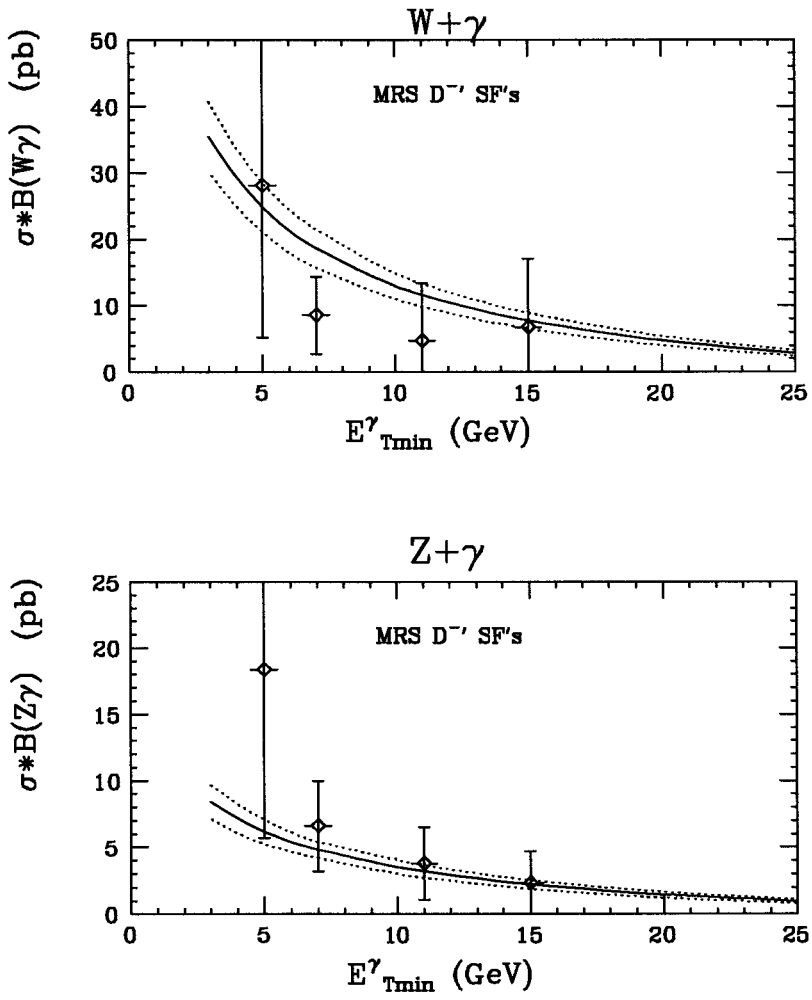


**Figure 8.1**: $\sigma \cdot BR$ for $W\gamma$ and $Z\gamma$ processes as a function of the minimum photon $E_T$. The 5 $GeV$ result is from data collected in the 1988-89 CDF run. That run had about 4 times less data and thus larger statistical uncertainties than the three Run 1A points at 7, 11, and 15 $GeV$.

the cross sections has a 3.5% systematic uncertainty. Ratios of cross sections cancel the luminosity and its uncertainty. The photon selection is the same for the $W$ and $Z$ samples, and a ratio of $\sigma \cdot BR(W\gamma)$ to $\sigma \cdot BR(Z\gamma)$ results in the cancellation of all the photon efficiencies, acceptances and their uncertainties.

The following cross section ratios have been calculated in the muon channel:

- $\sigma \cdot BR(W\gamma)/\sigma \cdot BR(W)$
- $\sigma \cdot BR(Z\gamma)/\sigma \cdot BR(Z)$
- $\sigma \cdot BR(W\gamma)/\sigma \cdot BR(Z\gamma)$

These ratios have been calculated as a function of minimum photon $E_T$ using the results from the previous section. The inclusive $W$ and $Z$ cross sections shown above, $\sigma \cdot BR(W)$ for $W \rightarrow \mu\nu_\mu$ and $\sigma \cdot BR(Z)$ for $Z \rightarrow \mu^+\mu^-$, are measured to be $2.44 \pm 0.03(stat) \pm 0.15(syst)\ nb$ [46] and $0.20 \pm 0.01(stat) \pm 0.01(syst)\ nb$, respectively [46]. The experimental and SM cross section ratio results are listed in Tables 8.9-8.11 for the three photon $E_T$ thresholds of 7, 11, and 15 $GeV$. The SM $W\gamma$ and $Z\gamma$ predictions use Baur Monte Carlo cross section times branching ratios, and the inclusive $W$ and $Z$ cross section predictions are from Stirling [19]. Figures 8.2a-c show the cross section ratios listed above for minimum photon $E_T$ thresholds of 5, 7, 11 and 15 $GeV$. The 5 $GeV$ points are results from the 1988-89 analysis.

Note that in Fig. 8.2a-c there are several other theoretical curves for cross section ratios that are slightly different than the ratios defined above. They are referred to as $RadW/W$ in Fig. 8.2a, $RadZ/Z$ in Fig. 8.2b, and $W\gamma/RadZ$ and $RadW/Z\gamma$ in Fig. 8.2c.

| Ratio | Data | SM Prediction |
|---|---|---|
| $\mu$ $W\gamma/W$ | $0.4^{+0.3}_{-0.3}\%$ | $0.77 \pm 0.01\%$ |
| $\mu$ $Z\gamma/Z$ | $3.3^{+1.7}_{-1.7}\%$ | $2.18 \pm 0.01\%$ |
| $\mu$ $W\gamma/Z\gamma$ | $1.4^{+1.8}_{-1.0}$ | $3.88^{+0.02}_{-0.02}$ |

**Table 8.9**: Summary of $W\gamma$ and $Z\gamma$ cross section ratios for 7 GeV photon threshold.

| Ratio | Data | SM Prediction |
|---|---|---|
| $\mu$ $W\gamma/W$ | $0.2^{+0.3}_{-0.3}\%$ | $0.48 \pm 0.003\%$ |
| $\mu$ $Z\gamma/Z$ | $1.9^{+1.4}_{-1.4}\%$ | $1.45 \pm 0.01\%$ |
| $\mu$ $W\gamma/Z\gamma$ | $1.3^{+2.6}_{-2.5}$ | $3.64^{+0.02}_{-0.02}$ |

**Table 8.10**: Summary of $W\gamma$ and $Z\gamma$ cross section ratios for 11 GeV photon threshold.

| Ratio | Data | SM Prediction |
|---|---|---|
| $\mu$ $W\gamma/W$ | $0.3^{+0.4}_{-0.4}\%$ | $0.32 \pm 0.002\%$ |
| $\mu$ $Z\gamma/Z$ | $1.2^{+1.2}_{-1.2}\%$ | $1.01 \pm 0.01\%$ |
| $\mu$ $W\gamma/Z\gamma$ | $2.9^{+3.5}_{-5.5}$ | $3.48^{+0.02}_{-0.02}$ |

**Table 8.11**: Summary of $W\gamma$ and $Z\gamma$ cross section ratios for 15 GeV photon threshold.

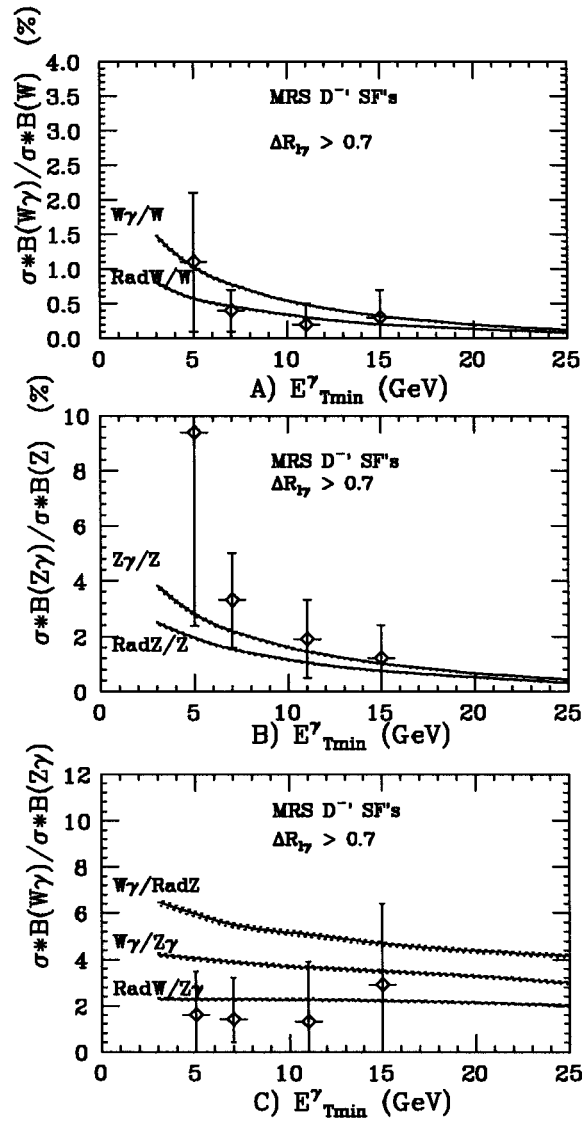


**Figure 8.2**: Cross section ratios as a function of photon $E_T$ threshold. The data points at 5 $GeV$ are the 1988-89 results. In a), the upper curve is the theoretical $W\gamma/W$ and the lower curve is $RadW/W$. In b), the upper curve is the theoretical $Z\gamma/Z$ and the lower curve is $RadZ/Z$. And in c), the middle curve is the theoretical $W\gamma/Z\gamma$, the lower curve is $RadW/Z\gamma$ and the upper curve is $W\gamma/RadZ$.

These cross section ratios involve radiative-only $W\gamma$ decays (*RadW*, see Fig. 2.1c,d) and radiative-only $Z\gamma$ decays (*RadZ*, see Fig. 2.5c). The theoretical cross sections for such decays are calculated using the convention of Berends and Kleiss [53]. By comparing, for example, the cross section ratio $W\gamma/W$ to the ratio $RadW/W$, as is done in Fig. 8.2a, we can see if the data are more consistent with the full SM prediction (which uses all of the diagrams in Fig. 2.1) or the radiative-only prediction for $W\gamma$ production. An analogous comparison is done for $Z\gamma$ processes in Fig. 8.2b. These comparisons provide a cross-check of the kinds of processes that produce $W$ and $Z$ bosons in association with photons. If the $W\gamma/W$ cross section ratio turns out to be consistent with the radiative-only predictions, for instance, then that would mean there is a problem with the SM predictions concerning the $s$-channel production of $W\gamma$ events.

Figure 8.2c is perhaps more enlightening because it uses information from the previous two figures. As can be seen, the ratio of $W\gamma$ to $Z\gamma$ cross sections in the data tend to be lower than the SM prediction (shown as $W\gamma/Z\gamma$ in the figure). This ratio is more consistent with the ratio of the radiative-only $W$ decay cross section to the SM $Z\gamma$ cross section (shown as $RadW/Z\gamma$ on the figure). Using the information from Figs. 8.2a,b we see that this implies the data are more consistent with radiative-only $W\gamma$ decays and SM $Z\gamma$ production. A strong statement cannot be made because of the low statistics. For now these results may just mean that the number of $W\gamma$ events has fluctuated low, and only larger statistics will show if this is a real effect or not. However, a strong statement can be made about the *magnitude* of the cross section ratios between $W\gamma$ and $Z\gamma$. In Sec. 2.2 it is mentioned that the $W\gamma/Z\gamma$ ratio is predicted to be of order 4 in the SM.

This can be compared to the ratio of inclusive $W/Z$ cross sections, which is 10.9. The difference in magnitudes of these ratios is caused by the destructive interference that occurs between the $u$- and $t$-channel diagrams and the $s$-channel diagram in the $W\gamma$ system. No such interference occurs in the $Z\gamma$ system. The $W\gamma$ cross section is therefore suppressed, and the ratio $W\gamma/Z\gamma$ decreases. The experimental ratios are consistent with the SM prediction.

## 8.3 Extraction of Limits on Anomalous Couplings

The presence of anomalous couplings in $W+\gamma$ or $Z+\gamma$ processes results in higher cross sections than predicted by the SM. Physically, non-zero anomalous couplings mean that the gauge bosons are composite particles, consisting of as yet undiscovered particles. In the CDF detector this effect is expected to manifest itself in a pronounced high-$E_T$ tail in the observed photon $E_T$ spectrum. Figure 8.3 shows how the theory predicts higher rates of high $E_T$ photon production in $W\gamma$ events as the values of anomalous couplings increase. At the low $E_T$ end the rates differ very little regardless of the magnitude of the anomalous couplings. A similar effect is seen in the distribution of the muon-photon separation. Figure 8.4 shows this distribution for various values of anomalous couplings.

One of the goals of this analysis is to extract new limits on the values of the anomalous couplings for $WW\gamma$, $ZZ\gamma$ and $Z\gamma\gamma$ processes. In order to do this the sensitivity of the high $E_T$ tail of the photon spectra to anomalous couplings is exploited. The procedure starts with the generation of Monte Carlo events, for all three processes mentioned above,

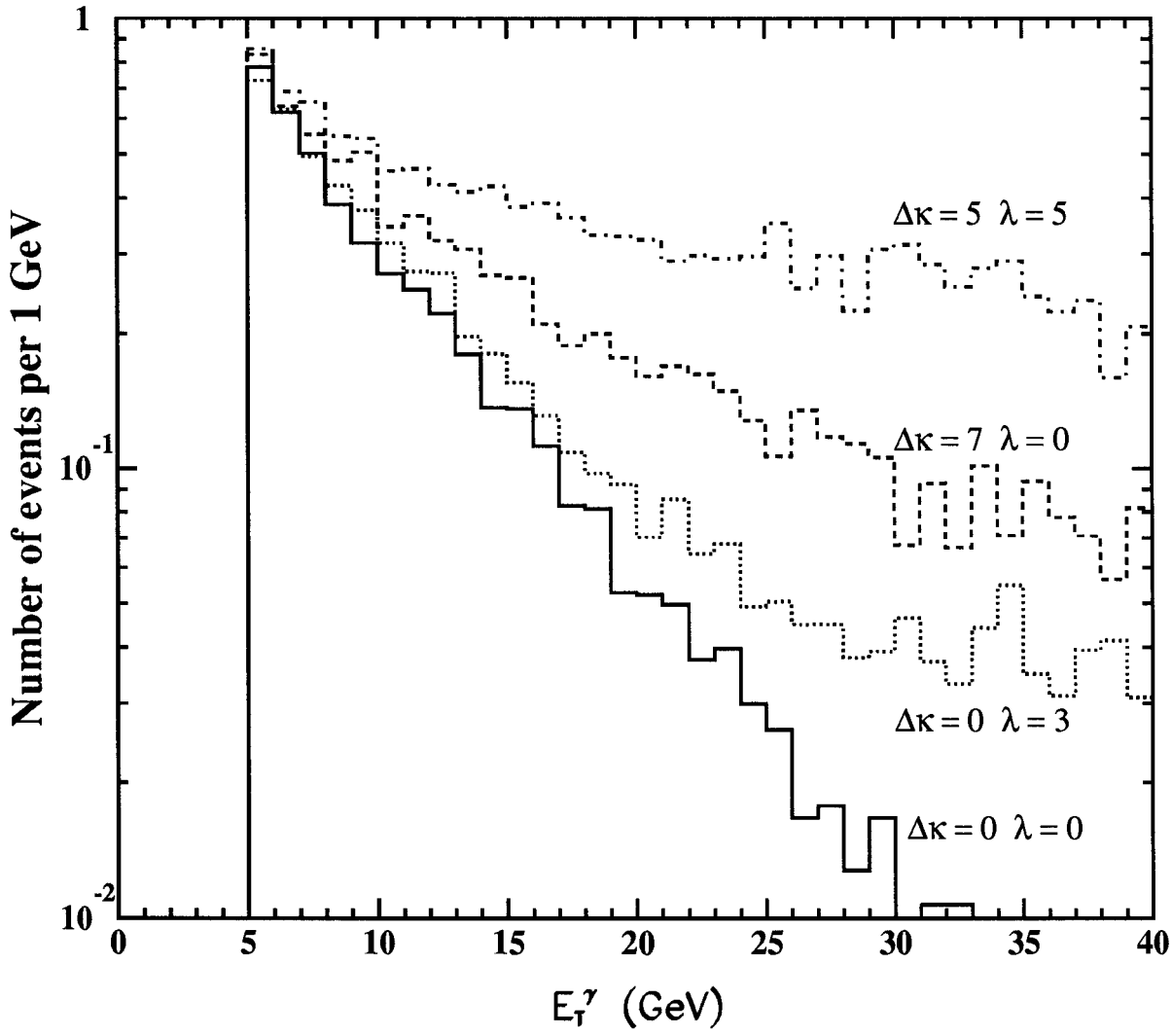


**Figure 8.3**: The photon $E_T$ spectrum for different values of the anomalous couplings $\Delta\kappa, \lambda$. Notice that low $E_T$ end is not affected as much as high $E_T$ end.

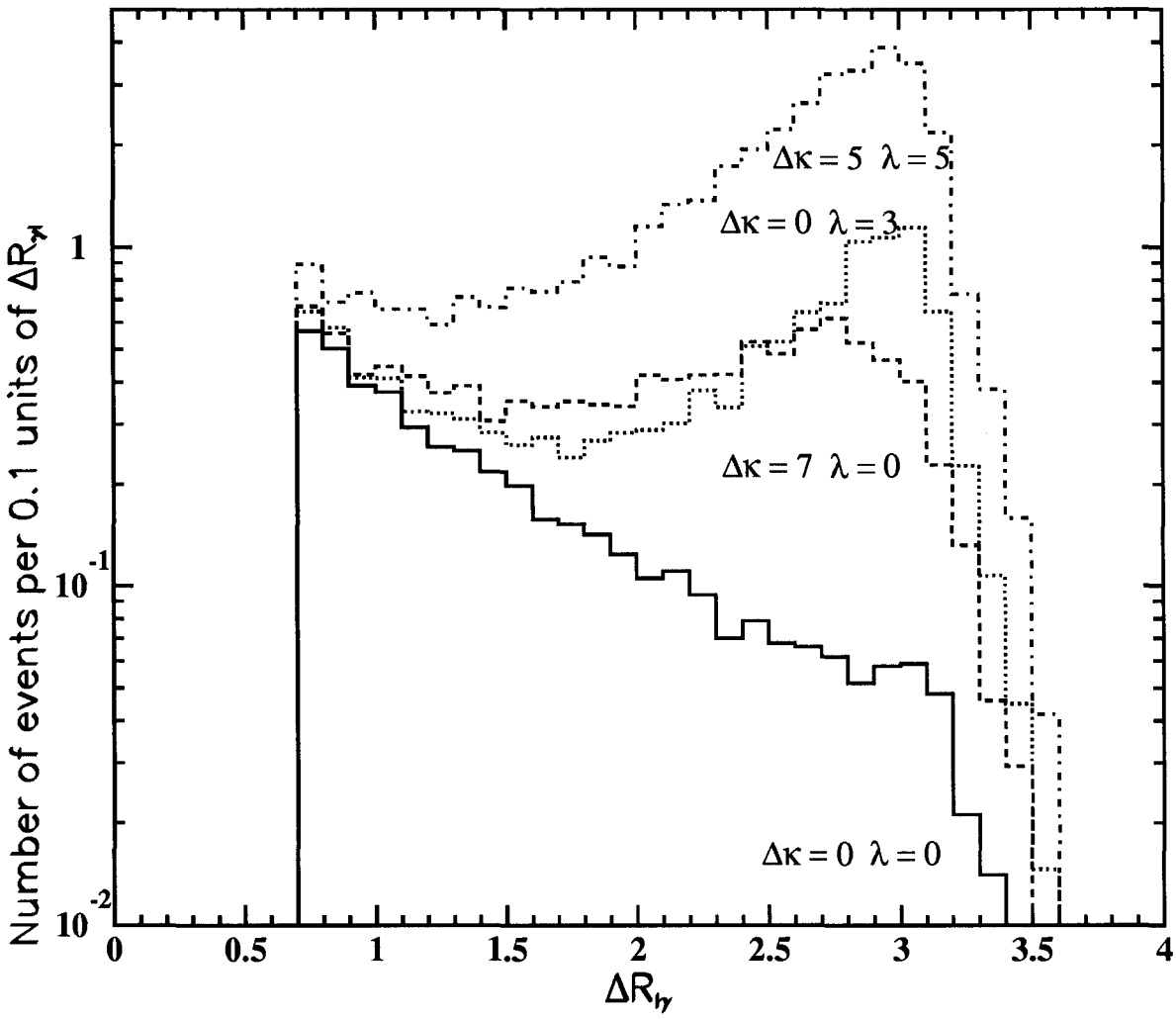


**Figure 8.4**: The muon-photon separation for different values of anomalous couplings. There is a smaller fraction of radiative decays (generally with small $\mu - \gamma$ separation) as anomalous couplings assume larger non-zero values due to enhanced $W\gamma$ production via the 3-boson interactions.

with various non-zero pairs of the anomalous couplings $\Delta\kappa, \lambda$ or $\tilde{\kappa}, \tilde{\lambda}$. Traditionally, limits have been set where only two of these couplings, either the CP conserving or the CP violating pair, are non-zero at a time. For the sake of comparison with previous results, we set limits this way as well. Although there is no *a priori* reason that all four cannot be non-zero at the same time, the consequence of such a choice is that the limits are more conservative than if all of the couplings are allowed to vary at the same time. This is clear from Eq. 2.10, because with all four couplings 'turned on', more events would be predicted with high $E_T$ photons in them than with only two of the four couplings 'turned on'. Tables 8.12 and 8.13 show the generated pairs of anomalous couplings and the number of events expected in four photon $E_T$ bins. The bins used are from 7-11 $GeV$, 11-15 $GeV$, 15-27 $GeV$ and above 27 $GeV$. The fast detector simulation is run on each Monte Carlo sample to get the event yield predictions listed. The tables again reflect how the number of $W\gamma$ and $Z\gamma$ events increases in the high $E_T$ bin as the values of the anomalous couplings deviate from zero, while there is little change in the number of $W\gamma$ and $Z\gamma$ events in the lower $E_T$ bins.

The predicted number of events in each $E_T$ bin $i$, $\mu_i$, can be represented as a function of two anomalous couplings by [13]

$$\mu_i(\Delta\kappa, \lambda) = N_i^{SM} + A_i\Delta\kappa + B_i\lambda + C_i\Delta\kappa^2 + D_i\lambda^2 + E_i\Delta\kappa\lambda \tag{8.3}$$

Note that the example given here is for $CP$-conserving $W\gamma$ anomalous couplings, $\Delta\kappa$ and $\lambda$; similar equations can be written for $\tilde{\kappa}$ and $\tilde{\lambda}$ and all $h_{i0}^V$ pairs, since they are just

| $(\Delta\kappa, \lambda)$ | 7-11 GeV | 11-15 GeV | 15-27 GeV | 27+ GeV |
|---|---|---|---|---|
| 0, 0 | 3.99 | 2.07 | 2.07 | 0.44 |
| 3, 0 | 4.08 | 2.23 | 2.74 | 2.51 |
| $-3$, 0 | 4.19 | 2.60 | 2.90 | 2.35 |
| 0, 2 | 3.95 | 2.19 | 2.43 | 10.45 |
| $0, -2$ | 4.14 | 2.16 | 2.44 | 9.78 |
| 3, 2 | 4.60 | 2.75 | 4.16 | 17.33 |
| $3, -2$ | 4.04 | 2.10 | 1.93 | 7.99 |
| $-3$, 2 | 3.98 | 2.29 | 2.34 | 7.65 |
| $-3, -2$ | 4.61 | 2.97 | 4.37 | 18.28 |
| $(\tilde{\kappa}, \tilde{\lambda})$ | | | | |
| 0, 0 | 3.99 | 2.07 | 2.07 | 0.44 |
| 3, 0 | 4.16 | 2.29 | 2.58 | 2.49 |
| $-3$, 0 | 4.33 | 2.55 | 2.81 | 2.41 |
| 0, 2 | 4.32 | 1.95 | 2.43 | 9.63 |
| $0, -2$ | 4.24 | 2.36 | 2.51 | 10.45 |
| 3, 2 | 4.47 | 2.52 | 3.98 | 17.42 |
| $3, -2$ | 4.08 | 2.08 | 2.18 | 7.61 |
| $-3$, 2 | 4.48 | 2.08 | 2.16 | 7.38 |
| $-3, -2$ | 4.95 | 2.94 | 4.54 | 17.52 |

**Table 8.12**: Summary of the pairs of $(\Delta\kappa, \lambda)$ and $(\tilde{\kappa}, \tilde{\lambda})$ used for generating $W\gamma$ samples along with the predicted number of events for each $E_T$ bin. These samples were used in fitting the photon $E_T$ spectrum to extract limits on anomalous couplings.

| $(h_{30}^Z, h_{40}^Z)$ | 7-11 GeV | 11-15 GeV | 15-27 GeV | 27+ GeV |
|---|---|---|---|---|
| 0.0, 0.0 | 1.24 | 0.81 | 0.86 | 0.23 |
| 7.5, 0.0 | 1.35 | 0.80 | 1.00 | 15.74 |
| −7.5, 0.0 | 1.31 | 0.85 | 0.84 | 15.67 |
| 0.0, 0.9 | 1.29 | 0.79 | 0.94 | 4.16 |
| 0.0, −0.9 | 1.26 | 0.80 | 0.83 | 4.98 |
| 7.5, 0.9 | 1.28 | 0.83 | 0.94 | 6.69 |
| 7.5, −0.9 | 1.28 | 0.78 | 1.02 | 33.14 |
| −7.5, 0.9 | 1.27 | 0.80 | 1.01 | 32.94 |
| −7.5, −0.9 | 1.30 | 0.80 | 0.99 | 6.53 |
| $(h_{30}^\gamma, h_{40}^\gamma)$ | | | | |
| 0.0, 0.0 | 1.24 | 0.81 | 0.86 | 0.23 |
| 7.5, 0.0 | 1.30 | 0.77 | 0.91 | 13.87 |
| −7.5, 0.0 | 1.34 | 0.79 | 0.91 | 13.76 |
| 0.0, 0.9 | 1.27 | 0.80 | 0.85 | 3.86 |
| 0.0, −0.9 | 1.31 | 0.80 | 0.83 | 3.73 |
| 7.5, 0.9 | 1.31 | 0.78 | 0.93 | 5.61 |
| 7.5, −0.9 | 1.31 | 0.76 | 0.94 | 29.31 |
| −7.5, 0.9 | 1.30 | 0.78 | 0.94 | 29.53 |
| −7.5, −0.9 | 1.27 | 0.83 | 0.93 | 5.55 |

**Table 8.13**: Summary of the pairs of $(h_{30}^Z, h_{40}^Z)$ and $(h_{30}^\gamma, h_{40}^\gamma)$ used for generating $ZZ\gamma$ and $Z\gamma\gamma$ samples, respectively, along with the predicted number of events for each $E_T$ bin. These samples were used in fitting the photon $E_T$ spectrum to extract limits on anomalous couplings.

modified versions of Eq. 2.10. This equation represents an elliptical paraboloid surface in event-anomalous coupling space with 5 coefficients. No higher-order terms in $\Delta\kappa$, $\lambda$ are needed, since the invariant amplitudes $M_{\gamma,W}$ containing the anomalous contributions to the $W\gamma$ ($Z\gamma$) processes are linear in their anomalous parameters (see Equations (2.8)-(2.9)). The fast detector simulation results from the various Baur samples generated with known pairs of couplings are used to obtain least square fit values for the 5 coefficients. This is done for each bin $i$.

Because each $E_T$ bin has an equation to find the predicted number of events for *any* pair of anomalous couplings, any number of pairs of anomalous couplings can be run through to find a pair that best matches the observed number of events in the data. A $500 \times 500$ matrix of 250,000 pairs of couplings is scanned for each $E_T$ bin $i$. For each pair of couplings the number of predicted events, $\mu_i$, is calculated, and the expected number of background events, $\overline{x}_i$, from the data in that bin, is added to $\mu_i$. The Poisson probability of the predicted number of diboson events plus the number of background events fluctuating to the number of *observed* events in the data, $N_i$, is then calculated for each bin. The probability of each bin is multiplied together:

$$\mathcal{P} = \prod_i^{nbins} \frac{e^{-(\mu_i(\Delta\kappa,\lambda)+\overline{x}_i)} \cdot (\mu_i(\Delta\kappa,\lambda)+\overline{x}_i)^{N_i}}{(N_i)!}$$

To take systematic uncertainties into account, the uncertainties from both the background and Monte Carlo predictions are added together in quadrature. The sum of $\mu_i$ and the number of background events in bin $i$ are smeared by the systematic uncertain-

ties by a Gaussian distribution $GAU(x, \overline{x}, \sigma_x)$, where $\sigma_x$ is the uncertainty on $\overline{x}$. The (negative) natural logarithm is taken to give a log likelihood

$$-\ln\mathcal{L}(\Delta\kappa, \lambda) = \text{-ln} \int_{-\infty}^{+\infty} \prod_i^{nbins} \left(\frac{e^{-(\mu_i(\Delta\kappa,\lambda)+x_i)} \cdot (\mu_i(\Delta\kappa,\lambda)+x_i)^{N_i}}{(N_i)!}\right) \cdot GAU(x_i, \overline{x_i}, \sigma_{x_i}) dx_i$$

The maximum value of this negative log likelihood, $-\mathcal{L}_{max}$, is determined and the shape of $-\ln\mathcal{L}$ is used to get limits on anomalous couplings at various confidence levels (CL). In order to get the 95% CL limits on $\Delta\kappa$ and $\lambda$, for instance, all pairs of ($\Delta\kappa$, $\lambda$) which produce results that have a log likelihood which differs from $-\mathcal{L}_{max}$ by 3.0 units [54] are recorded. These values form an ellipse in the $(\Delta\kappa, \lambda)$ plane. Similarly, the 68% CL ellipse is found with all pairs of couplings whose log likelihood differs from $-\mathcal{L}_{max}$ by 1.15 units, and the 90% CL ellipse is found when the difference between $-\mathcal{L}_{max}$ and the log likelihood of all pairs of couplings is 2.3 units. Historically, the limits which are quoted are the points on the ellipse which cross the $\Delta\kappa$ and $\lambda$ axes (that is, take the value of one coupling when *all* of the other couplings are set to 0). Figures 8.5a-d show plots of $-$log likelihood for individual values of the four $W\gamma$ anomalous couplings, where all of the other couplings have been set to 0. The horizontal lines going across the $-$log likelihood curves set the various CL limits where they intersect the $-$log likelihood curve. Table 8.14 lists the values of the limits at the 68%, 90% and 95% CL. Figure 8.6a shows the 68%, 90% and 95% CL ellipses in the $\Delta\kappa$-$\lambda$ plane, and Figure 8.6b shows the 68%, 90% and 95% CL ellipses in the $\tilde{\kappa}$-$\tilde{\lambda}$ plane.

The quoted limits on $W$-photon anomalous couplings are in fact *direct* limits taken from the data. In Chapter 2 it is mentioned that limits can be made on the $CP$-violating

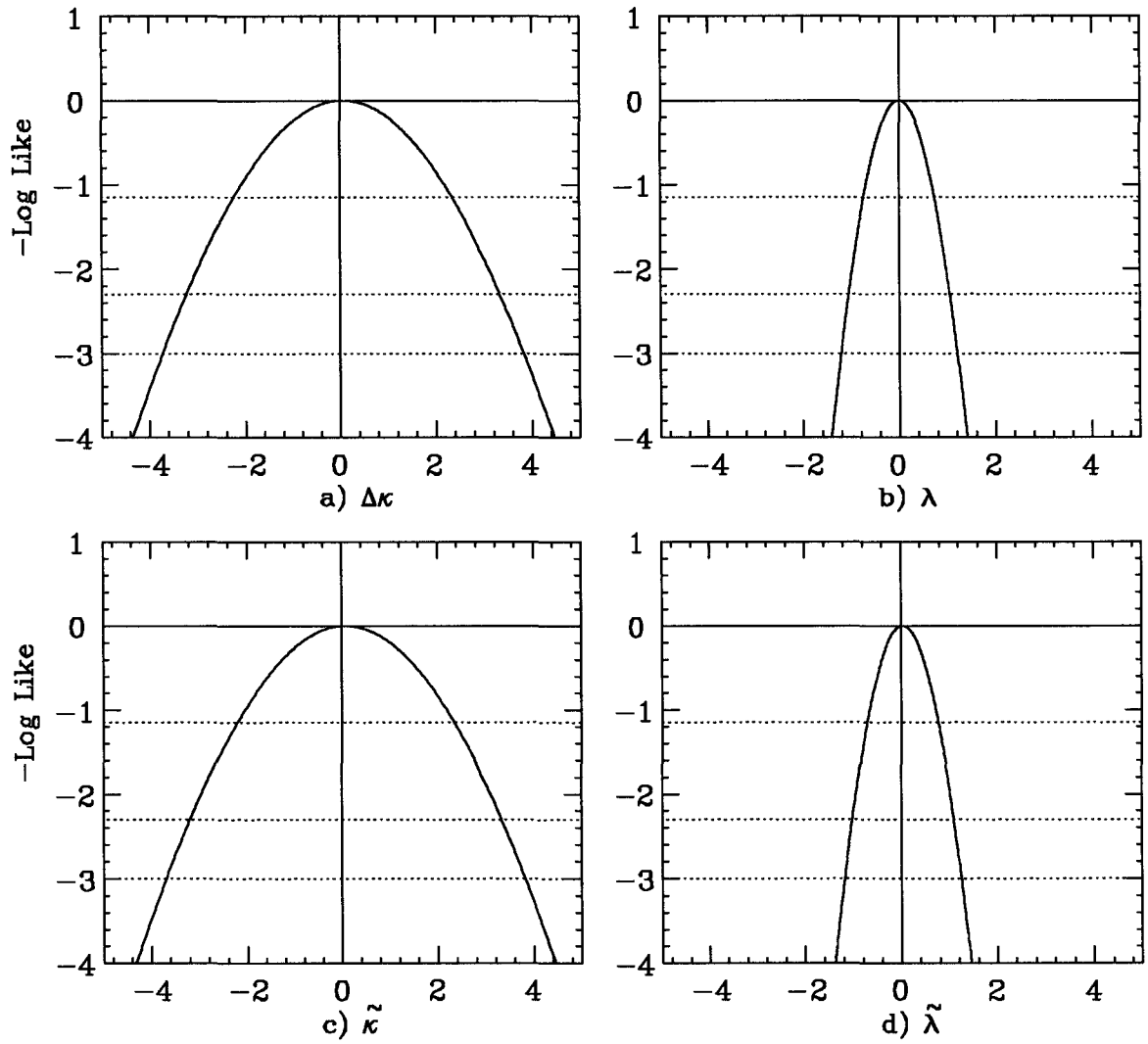


**Figure 8.5**: -Log likelihood versus $\Delta\kappa$, $\lambda$, $\tilde{\kappa}$ and $\tilde{\lambda}$ for 1992-93 muon $W\gamma$ sample. The dashed lines at -log like of -1.15, -2.3 and -3.0 give limits on the couplings at 68%, 90% and 95% CL, respectively.

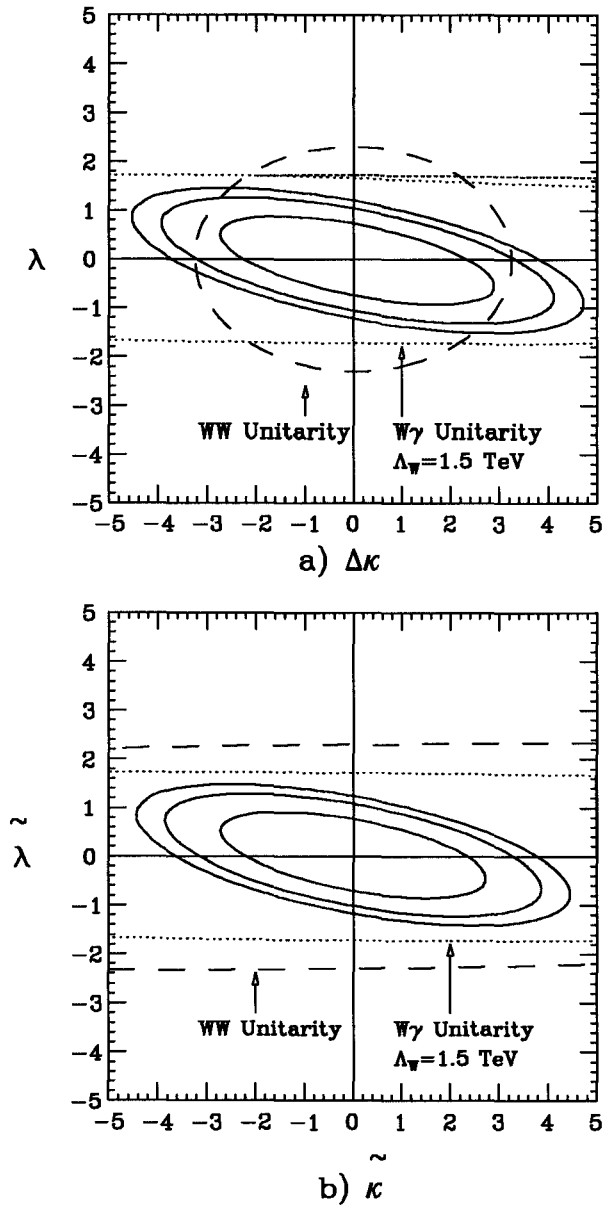


**Figure 8.6**: Contours of 68% (innermost ellipse), 90% and 95% (outermost ellipse) CL values for a) $\lambda$ vs $\Delta\kappa$ ,and b) $\tilde{\lambda}$ vs $\tilde{\kappa}$ for 1992-93 muon $W\gamma$ sample.

| Confidence Level | | |
|---|---|---|
| CP-Conserving | $\Delta\kappa$ | $\lambda$ |
| 68% | $-2.3 < \Delta\kappa < 2.3$ | $-0.7 < \lambda < 0.7$ |
| 90% | $-3.2 < \Delta\kappa < 3.2$ | $-1.0 < \lambda < 1.0$ |
| 95% | $-3.7 < \Delta\kappa < 3.7$ | $-1.2 < \lambda < 1.2$ |
| CP-Violating | $\tilde{\kappa}$ | $\tilde{\lambda}$ |
| 68% | $-2.3 < \tilde{\kappa} < 2.3$ | $-0.8 < \tilde{\lambda} < 0.8$ |
| 90% | $-3.3 < \tilde{\kappa} < 3.3$ | $-1.1 < \tilde{\lambda} < 1.1$ |
| 95% | $-3.8 < \tilde{\kappa} < 3.8$ | $-1.2 < \tilde{\lambda} < 1.2$ |

**Table 8.14**: Limits on CP-conserving and CP-violating anomalous couplings. The limit for a given coupling is taken when all other couplings are set to 0.

couplings, $\tilde{\kappa}$ and $\tilde{\lambda}$, from measurements of the neutron electric dipole moment (EDM). Further study of that method, though, shows that the *indirect* limits are not necessarily all that powerful. The general constraint from the EDM of the neutron for arbitrary $\tilde{\kappa}$ and $\tilde{\lambda}$ can be written as [12]

$$|\tilde{\kappa} \cdot [log(\frac{\Lambda^2}{M_W^2}) + a] + \tilde{\lambda} \cdot b| < c \tag{8.4}$$

where $c$ is the experimental limit of the neutron EDM converted to a dimensionless number, $M_W$ is the $W$ mass, $\Lambda$ is a cutoff of a loop integration, and $a$ and $b$ are numbers that are assumed to be of order 1. The value for $a$ has not been calculated yet, but $b$ has been determined to be $+1$, $+1/3$ and 0 using three different calculations [12]. Negative values of these parameters are not ruled out. If one of the two couplings ($\tilde{\kappa}$ and $\tilde{\lambda}$) are set to zero, the calculation gives finite limits on the non-zero valued coupling. However, this breaks down if both $\tilde{\kappa}$ and $\tilde{\lambda}$ are allowed to be non-zero. In order to get an ellipse of one coupling versus the other, as shown in Figure 8.6a-b, the value of $b$ needs to be known.

Since there is currently no single way of knowing what the parameter $b$ is, all predictive power is lost. This information is summarized in Figure 8.7. The three CL contours for $\tilde{\lambda}$ vs $\tilde{\kappa}$ are shown along with the 95% CL limits from the neutron EDM method. Three bands based on the EDM method are shown corresponding to values of $b = 1, 1/3$ and 0. As can be seen, in order to know where to place a limit on $\tilde{\lambda}$ or $\tilde{\kappa}$ using the neutron EDM method one needs to see where the bands intersect the contours obtained directly from the CDF data. Also note that the neutron EDM does not provide any indirect limits on the $CP$-conserving couplings, $\Delta\kappa$ and $\lambda$.

The algorithm used for extracting the limits on possible anomalous $W$-photon couplings can also be used to extract limits of possible $Z$-photon anomalous couplings, for both $ZZ\gamma$ and $Z\gamma\gamma$ processes. The log likelihood and contour plots for $ZZ\gamma$ and $Z\gamma\gamma$ processes are shown in Figures 8.8-8.11. Tables 8.15-8.11 summarize the limit values. Note that Figures 8.8 and 8.9 have $h_{30}^V(h_{10}^V)$ and $h_{40}^V(h_{20}^V)$ ($V$ is either $Z$ or $\gamma$) as axis labels. The individual contours for these pairs of couplings are indistinguishable, and so they are grouped together for presentation purposes.

The most intriguing feature of the $-$log likelihood plots for $ZZ\gamma$ and $Z\gamma\gamma$ processes is the dip that occurs at $h_{i0} = 0$. The dips are a direct result of the high $E_T$ photon event which is in the $Z\gamma$ final sample and suggest that the SM values of $h_{i0}$ are not the most likely. As shown in Figure 4.18, this one event has a low probability of occuring within the SM. Photons with high $E_T$ are expected if non-zero anomalous couplings exist, and therefore the likelihood dip reflects this expectation. However, the 95% CL limits on the anomalous couplings for $ZZ\gamma$ and $Z\gamma\gamma$ lie further out and are consistent with being

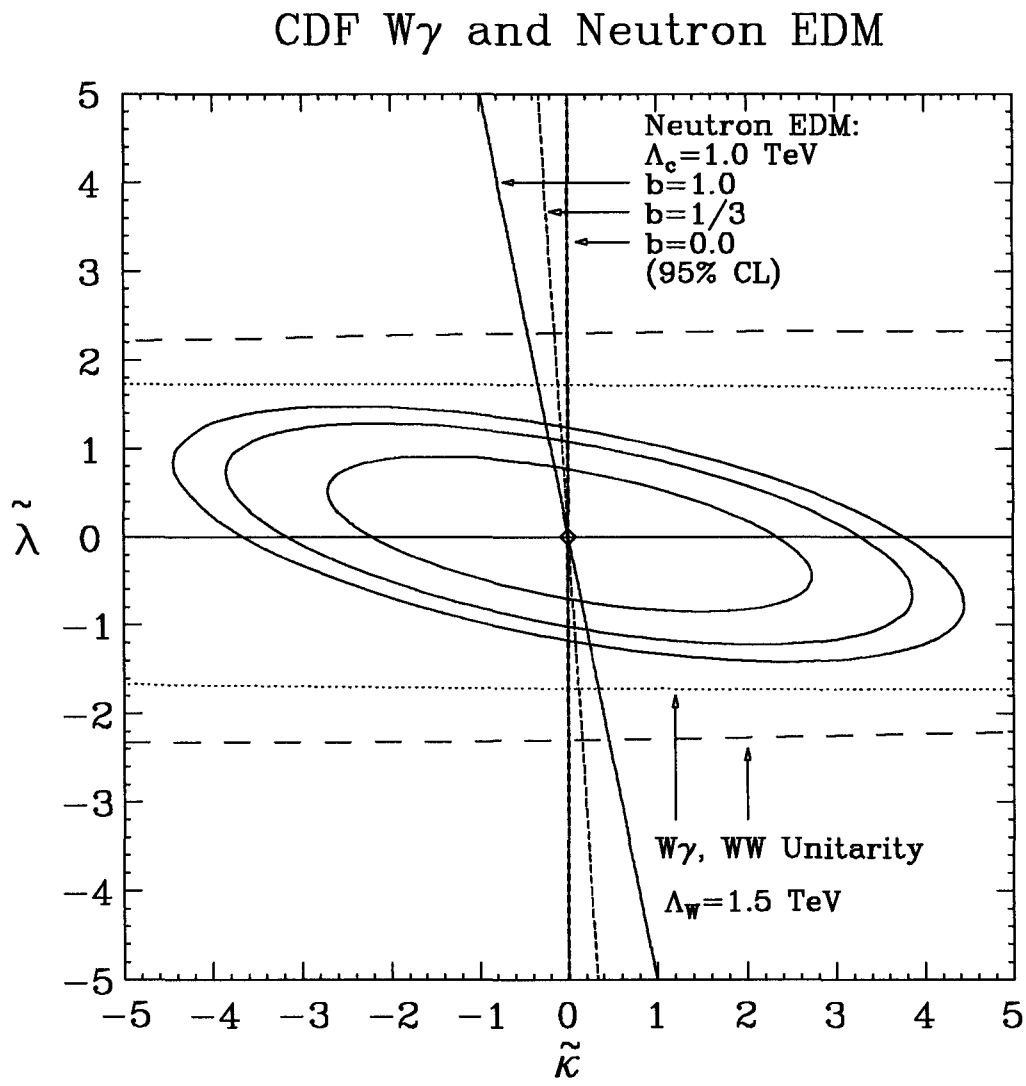


**Figure 8.7**: Comparison of the limit contours from CDF $W$ muon data and three schemes of calculating 95% CL limits from neutron EDM measurements. All predictive power is lost for the EDM method once both couplings are allowed to vary.

| Confidence Level | | |
|---|---|---|
| CP-Conserving | $h_{30}^Z$ | $h_{40}^Z$ |
| 68% | $-3.4 < h_{30}^Z < 3.4$ | $-0.8 < h_{40}^Z < 0.8$ |
| 90% | $-4.2 < h_{30}^Z < 4.2$ | $-1.0 < h_{40}^Z < 1.0$ |
| 95% | $-4.6 < h_{30}^Z < 4.6$ | $-1.1 < h_{40}^Z < 1.1$ |
| CP-Violating | $h_{10}^Z$ | $h_{20}^Z$ |
| 68% | $-3.4 < h_{10}^Z < 3.4$ | $-0.8 < h_{20}^Z < 0.8$ |
| 90% | $-4.2 < h_{10}^Z < 4.2$ | $-1.0 < h_{20}^Z < 1.0$ |
| 95% | $-4.6 < h_{10}^Z < 4.6$ | $-1.1 < h_{20}^Z < 1.1$ |

**Table 8.15**: Limits on $h_{i0}^Z$ anomalous couplings for $ZZ\gamma$ Processes. The limit for a given coupling is taken when all other couplings are set to 0.

| Confidence Level | | |
|---|---|---|
| CP-Conserving | $h_{30}^\gamma$ | $h_{40}^\gamma$ |
| 68% | $-3.6 < h_{30}^\gamma < 3.6$ | $-0.9 < h_{40}^\gamma < 0.9$ |
| 90% | $-4.5 < h_{30}^\gamma < 4.5$ | $-1.1 < h_{40}^\gamma < 1.1$ |
| 95% | $-4.9 < h_{30}^\gamma < 4.9$ | $-1.2 < h_{40}^\gamma < 1.2$ |
| CP-Violating | $h_{10}^\gamma$ | $h_{20}^\gamma$ |
| 68% | $-3.6 < h_{10}^\gamma < 3.6$ | $-0.9 < h_{20}^\gamma < 0.9$ |
| 90% | $-4.5 < h_{10}^\gamma < 4.5$ | $-1.1 < h_{20}^\gamma < 1.1$ |
| 95% | $-4.9 < h_{10}^\gamma < 4.9$ | $-1.2 < h_{20}^\gamma < 1.2$ |

**Table 8.16**: Limits on $h_{i0}^\gamma$ anomalous couplings for $Z\gamma\gamma$ Processes. The limit for a given coupling is taken when all other couplings are set to 0.

zero. The high $E_T$ event, though, is interesting, and greater statistics are needed so that a search for more unlikely events can made. No events of this nature are found in the final electron $Z\gamma$ sample. It is also interesting to note that for dilepton-photon 3-body masses above 150 $GeV/c^2$, the SM predicts about 0.3 $Z\gamma$ events (for combined electron and muon samples) to be observed.

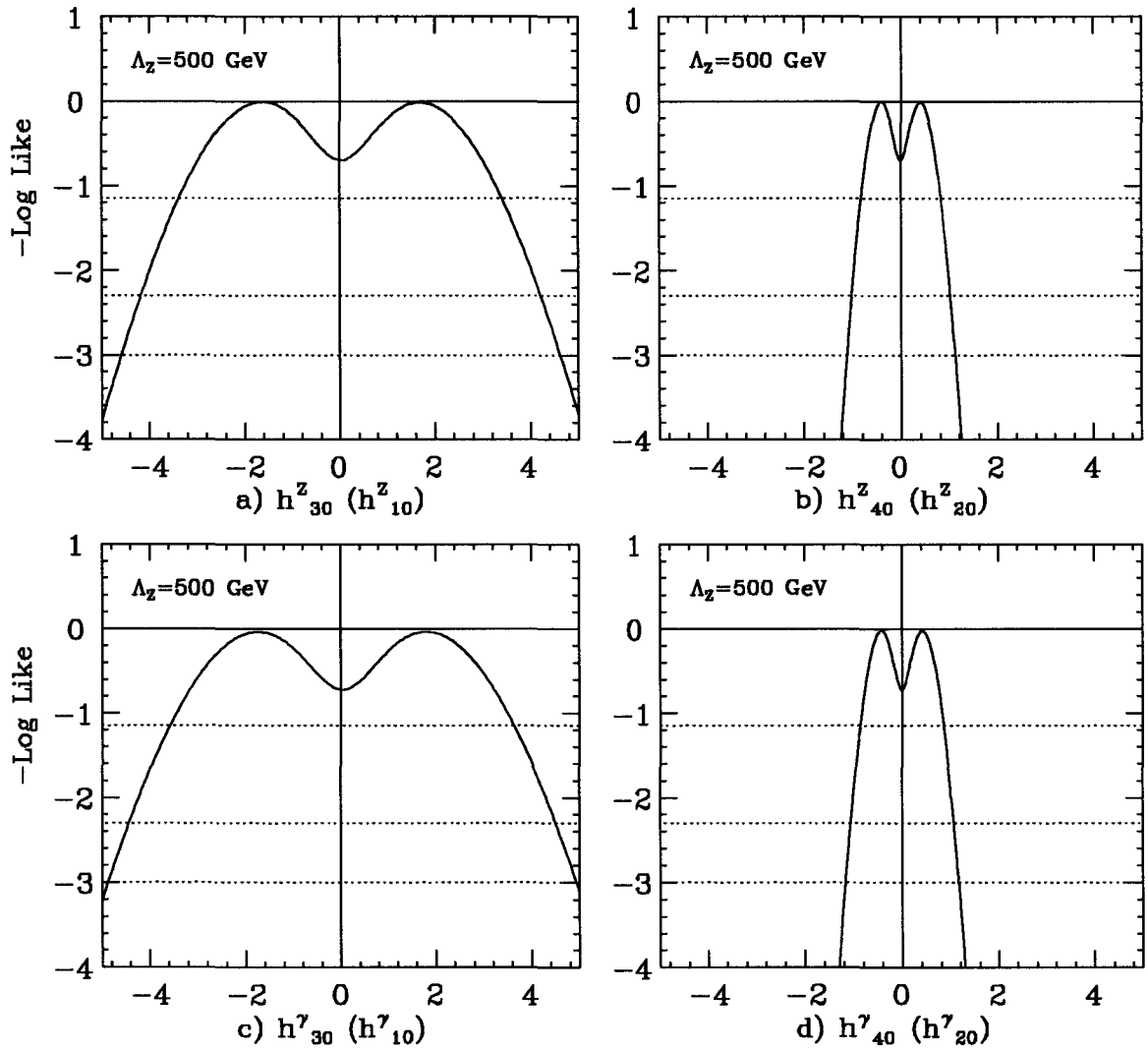


**Figure 8.8**: $ZZ\gamma$ and $Z\gamma\gamma$ -Log likelihood versus anomalous couplings. Figures a) and b) show $h_{30}^{Z}(h_{10}^{Z})$ and $h_{40}^{Z}(h_{20}^{Z})$, and Figures c) and d) show $h_{30}^{\gamma}(h_{10}^{\gamma})$ and $h_{40}^{\gamma}(h_{20}^{\gamma})$. The dashed lines at -log likelihood of -1.15, -2.3 and -3.0 give limits on the parameters at 68%, 90% and 95% CL, respectively.

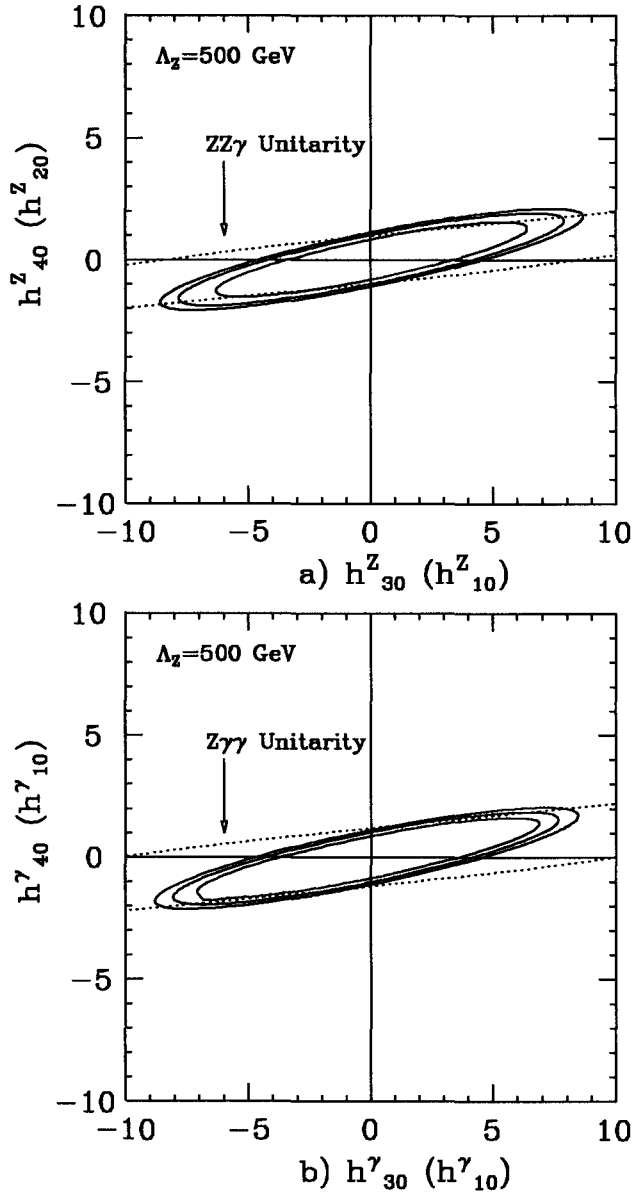


**Figure 8.9**: Contour plots of $h^V_{30}(h^V_{10})$ and $h^V_{40}(h^V_{20})$ for 1992-93 $\mu$ $Z\gamma$ sample. Figure a) is for $ZZ\gamma$ processes, and b) is for $Z\gamma\gamma$ processes.

## 8.4 Limits on EM Moments of $W$ and $Z$ Bosons

In Chapter 2, Equations (2.3)-(2.6) show how the $W\gamma$ anomalous couplings relate to higher order multipole moments of the $W$ boson. Using the contours of the the anomalous couplings, the corresponding contours for the multipole moments can be calculated. For presentation the following dimensionless (scaled) quantities are defined:

$$g_W - 2 = \frac{\mu_W}{\mu_W^0} - 2 = \Delta\kappa + \lambda \tag{8.5}$$

$$q_W^e - 1 = \frac{Q_W^e}{Q_W^{e0}} - 1 = \Delta\kappa - \lambda \tag{8.6}$$

$$d_W = \frac{d_W^e}{d_W^{e0}} = \tilde{\kappa} + \tilde{\lambda} \tag{8.7}$$

$$q_W^m = \frac{Q_W^m}{Q_W^{m0}} = \tilde{\kappa} - \tilde{\lambda} \tag{8.8}$$

The terms $\mu_W^0 = \frac{e\hbar}{2M_W}$, $Q_W^{e0} = -\frac{e\hbar^2}{(M_W c)^2}$, $d_W^{e0} = \frac{e\hbar}{2M_W c}$, and $Q_W^{m0} = -\frac{e\hbar^2}{M_W^2 c}$ are the classical moments of the $W$. The contours and limits on multipole moments of the $W$ boson are shown in Figure 8.10 and Table 8.17. For these and other contour plots shown, note that there are dotted and dashed contours which correspond to unitarity curves for a given form factor scale $\Lambda_{W,Z}$. The $W\gamma$ contours show unitarity curves for $\Lambda_W$ of 1.5 $TeV$, while any $Z\gamma$ contours show unitarity curves for $\Lambda_Z$ of 500 $GeV$. The contours represent values from the constraint equations shown in Sec. 2.3.

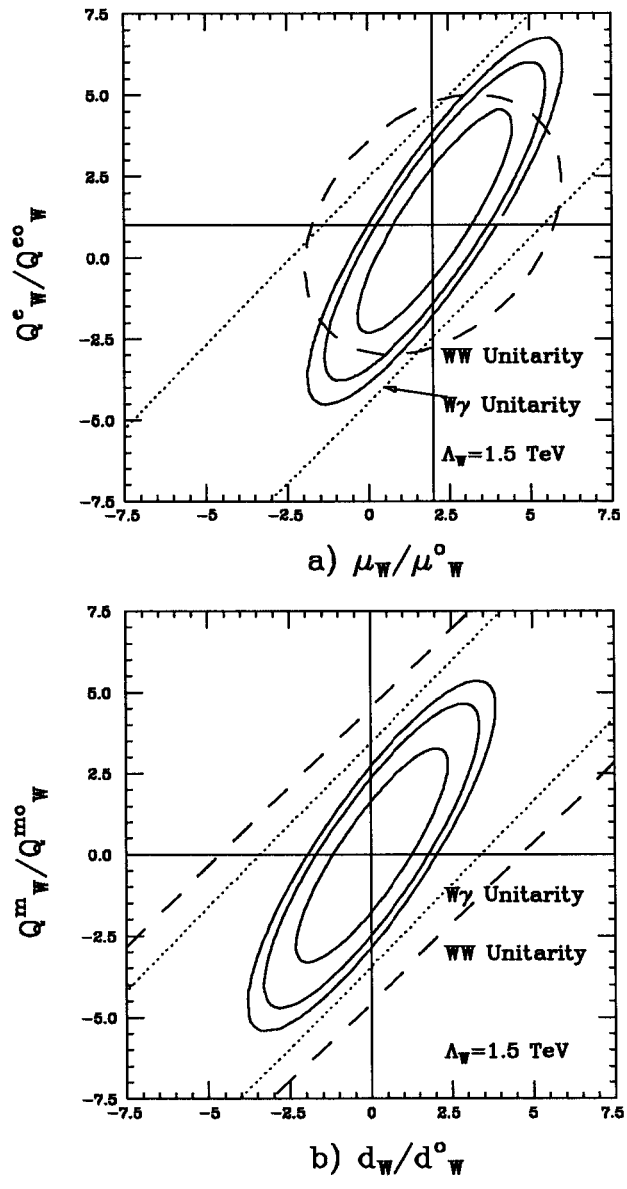


**Figure 8.10**: Contours of the limits of EM moments of the $W$ boson resulting from values of the anomalous couplings. Figure a) is the electric quadrupole vs magnetic dipole CP-conserving moments, and b) is the magnetic quadrupole vs electric dipole CP-violating moments.

| Confidence Level | | |
|---|---|---|
| CP-Conserving | Dipole Moment | Quadrupole Moment |
| 68% | $-1.2 < g_W - 2 < 1.2$ | $-1.7 < q_W^e - 1 < 1.7$ |
| 90% | $-1.7 < g_W - 2 < 1.7$ | $-2.5 < q_W^e - 1 < 2.5$ |
| 95% | $-2.0 < g_W - 2 < 2.0$ | $-2.7 < q_W^e - 1 < 2.7$ |
| CP-Violating | | |
| 68% | $-1.2 < d_W < 1.2$ | $-1.6 < q_W^m < 1.6$ |
| 90% | $-1.7 < d_W < 1.7$ | $-2.5 < q_W^m < 2.5$ |
| 95% | $-2.0 < d_W < 2.0$ | $-2.7 < q_W^m < 2.7$ |

**Table 8.17**: Summary of Limits on $W$ Boson CP-Conserving and CP-Violating $EM$ Moments.

Equations (2.14)-(2.17) relate the various couplings $h_{i0}^Z$ to the transition moments of the $Z$ boson. For presentation it is useful to define the following dimensionless quantities for the $Z$ boson:

$$\delta_{Z_T} \equiv \frac{d_{Z_T}}{d^0_{Z_T}} = \sqrt{2}\frac{k^2}{M_Z^2}(h_{30}^Z - h_{40}^Z) \tag{8.9}$$

$$q^m_{Z_T} \equiv \frac{Q^m_{Z_T}}{Q^{m0}_{Z_T}} = \sqrt{10}(2h_{30}^Z) \tag{8.10}$$

$$g_{Z_T} \equiv \frac{\mu_{Z_T}}{\mu_{Z_T}} = \sqrt{2}\frac{k^2}{M_Z^2}(h_{10}^Z - h_{20}^Z) \tag{8.11}$$

$$q^e_{Z_T} \equiv \frac{Q^e_{Z_T}}{Q^{e0}_{Z_T}} = \sqrt{10}(2h_{10}^Z) \tag{8.12}$$

where $d^0_{Z_T} = -\frac{e\hbar}{2M_Z c}$, $Q^{m0}_{Z_T} = \frac{e\hbar^2}{M_Z^2 c}$, $\mu^0_{Z_T} = -\frac{e\hbar}{2M_Z}$ and $Q^{e0}_{Z_T} = \frac{e\hbar^2}{M_Z^2 c^2}$, which are the classical parameters of the $Z$ boson.

Setting direct experimental limits on $\delta_{Z_T}$ and $g_{Z_T}$, as defined above, is problematic because of the factor $(k^2/M_Z^2)$, where $k$ is the photon energy. The $Z+\gamma$ energy spectrum

| Confidence Level | $\delta^*_{Z_T}$ $(g^*_{Z_T})$ | $q^m_{Z_T}$ $(q^e_{Z_T})$ |
|---|---|---|
| 68% | $-1.0 < \delta^*_{Z_T}(g^*_{Z_T}) < 1.0$ | $-4.3 < q^m_{Z_T}(q^e_{Z_T}) < 4.3$ |
| 90% | $-1.5 < \delta^*_{Z_T}(g^*_{Z_T}) < 1.5$ | $-7.8 < q^m_{Z_T}(q^e_{Z_T}) < 7.8$ |
| 95% | $-1.6 < \delta_{Z^*_T}(g^*_{Z_T}) < 1.6$ | $-9.0 < q^m_{Z_T}(q^e_{Z_T}) < 9.0$ |

**Table 8.18**: Summary of results for CP-Conserving (-Violating) EM *transition* moments of the $Z$ boson.

is continuous, and sharply peaked at the experimental cutoff in $E_T^\gamma$. This makes the two transition moments become rather ill-defined experimentally. Hence, we can define the following variables for these two quantities:

$$\delta^*_{Z_T} \equiv \delta_{Z_T}\left[\frac{M_Z^2}{k^2}\right] = \sqrt{2}(h^Z_{30} - h^Z_{40}) \tag{8.13}$$

$$g^*_{Z_T} \equiv g_{Z_T}\left[\frac{M_Z^2}{k^2}\right] = \sqrt{2}(h^Z_{10} - h^Z_{20}) \tag{8.14}$$

Figure 8.11 shows the 68%, 90% and 95% CL contours for $\delta^*_{Z_T}$ $(q^m_{Z_T})$ versus $g^*_{Z_T}$ $(q^e_{Z_T})$. The corresponding unitarity curves for the $ZZ\gamma$ transition moments are also shown as a dotted contour. Table 8.18 lists the limits on the various transition moments of the $Z$ boson.

## 8.5 Form Factor Scale Sensitivity

Unitarity limits and the form factor scales $\Lambda_W$ and $\Lambda_Z$ are discussed in Chapter 2. With the extraction of limits on anomalous couplings, we can relate them to theoretical bounds that result from unitarity arguments. In essence the experimental sensitivity to the form

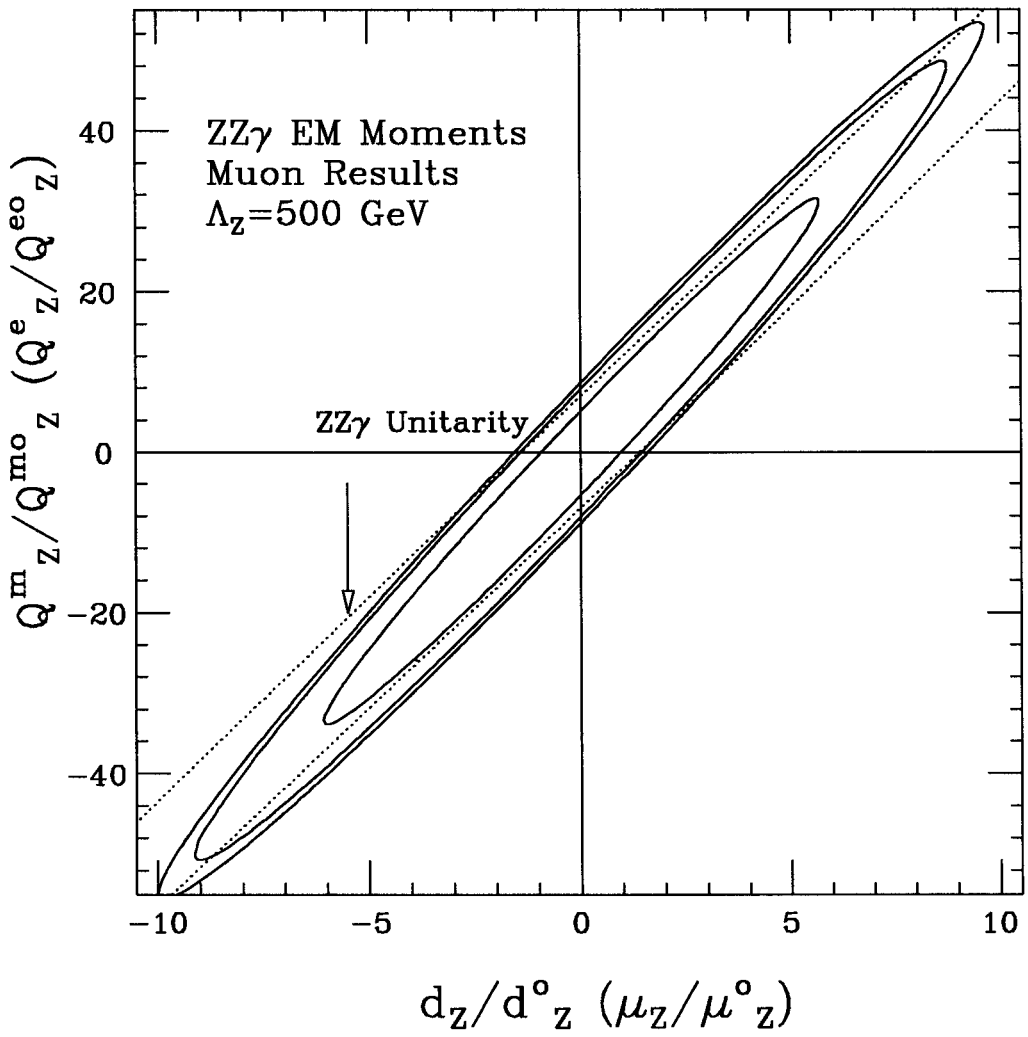


**Figure 8.11**: Contour plots of $Z$ EM transition moments for 1992-93 $\mu$ $Z\gamma$ sample.

factor energy scales can be extracted by comparing the experimental limits to unitarity limits. Figures 8.12a-d show the limits obtained on $W\gamma$ anomalous couplings, as a function of $\Lambda_W$, from data and unitarity. Figures 8.12a,b are for $\Delta\kappa$ and $\lambda$, respectively, and have the experimental 68% and 95% limits plotted along with $W\gamma$ unitarity curve. Figures 8.12c,d show the same experimental limits plotted along with the $W^+W^-$ unitarity curve. For values of $\Lambda_W$ less than the values where the curves intersect, the data provides better limits to the given coupling than does unitarity. This is the limit of the experimental sensitivity to a particular coupling. The regions above the curves are not allowed. Regions below the curves are not ruled out. Figures 8.13a-d show the same curves for $\tilde{\kappa}$ and $\tilde{\lambda}$. Finally, Figures 8.14a-d show limits on $h_{i0}^Z$ and $h_{i0}^\gamma$ along with $ZZ\gamma$ and $Z\gamma\gamma$ unitarity limits. At the 95% CL, for $W\gamma$ processes, unitarity is saturated (i.e. the intersection of the two curves) for values of $\Lambda_W$:

$$\Lambda_W^{\Delta\kappa} \geq 1.4\ TeV$$

$$\Lambda_W^{\lambda} \geq 1.7\ TeV$$

$$\Lambda_W^{\tilde{\kappa}} \geq 7.4\ TeV$$

$$\Lambda_W^{\tilde{\lambda}} \geq 1.4\ TeV$$

The limits quoted are taken for a single anomalous coupling, when all other couplings are set to zero. It is possible to translate the form factor energy scales into distance scales, using Equation (2.28), which corresponds to the sensitivity for probing possible internal structure of the $W$ or $Z$ boson. Below the distance scales are listed in terms of

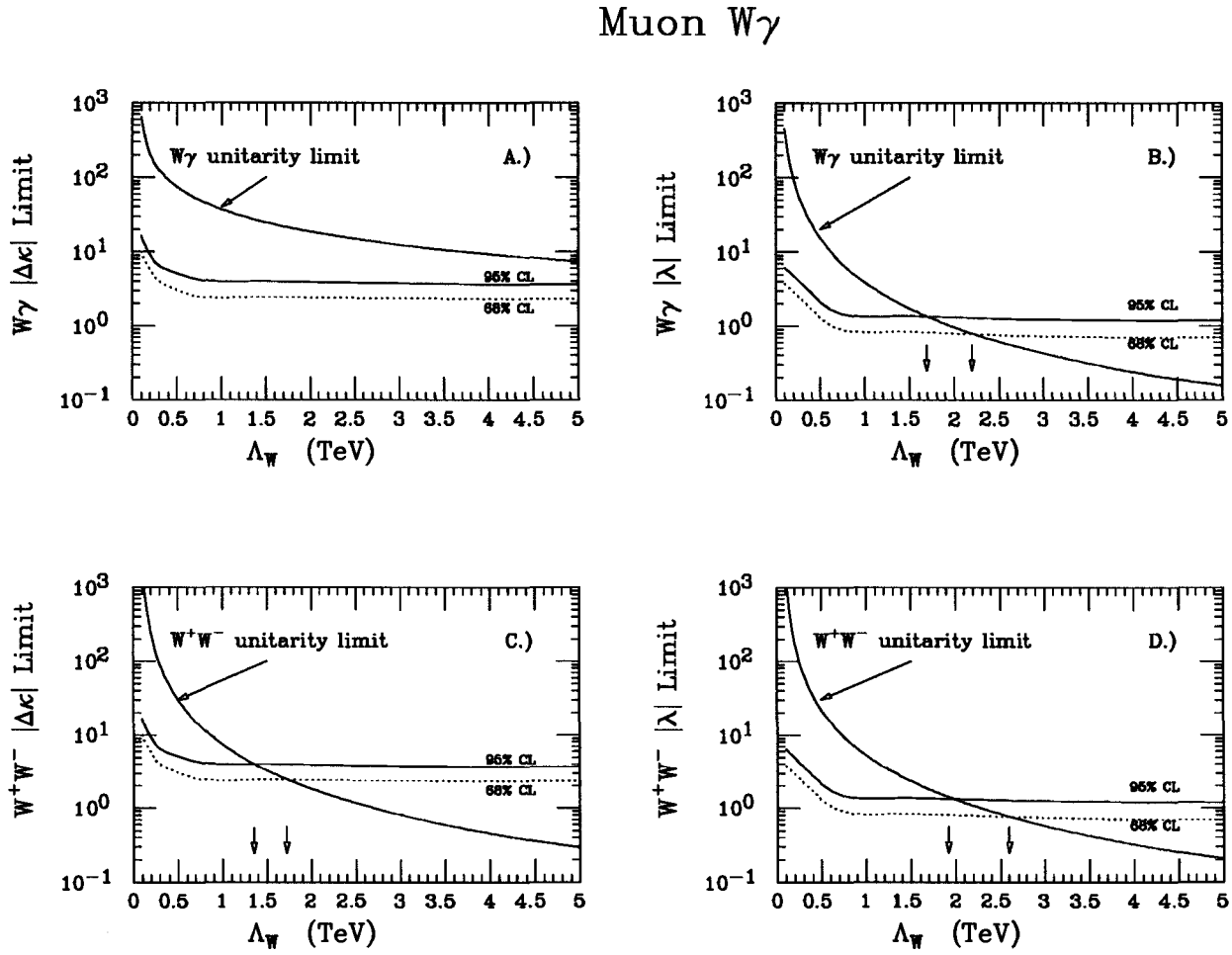


**Figure 8.12**: In a) and b), limits on $\Delta\kappa$ and $\lambda$ as a function of $\Lambda_W$ compared to $W\gamma$ unitarity limits. In c) and d), limits on $\Delta\kappa$ and $\lambda$ as a function of $\Lambda_W$ compared to $W^+W^-$ unitarity limits. The 68% and 95% CL limits from the data are shown. The regions above the curves are not allowed.

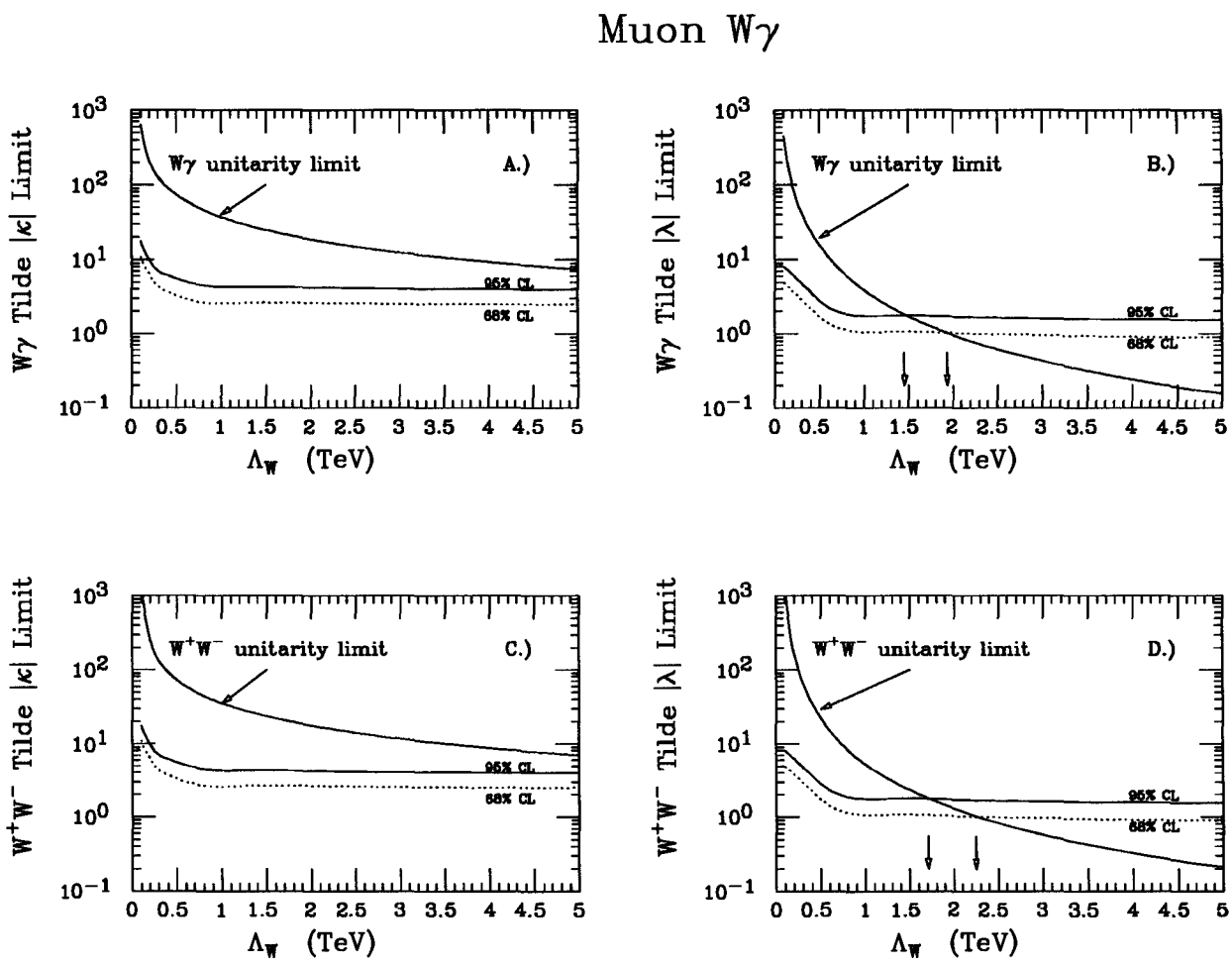


**Figure 8.13**: In a) and b), limits on $\tilde{\kappa}$ and $\tilde{\lambda}$ as a function of $\Lambda_W$ compared to $W\gamma$ unitarity limits. In c) and d), limits on $\tilde{\kappa}$ and $\tilde{\lambda}$ as a function of $\Lambda_W$ compared to $W^+W^-$ unitarity limits. The 68% and 95% CL limits from the data are shown. The regions above the curves are not allowed.

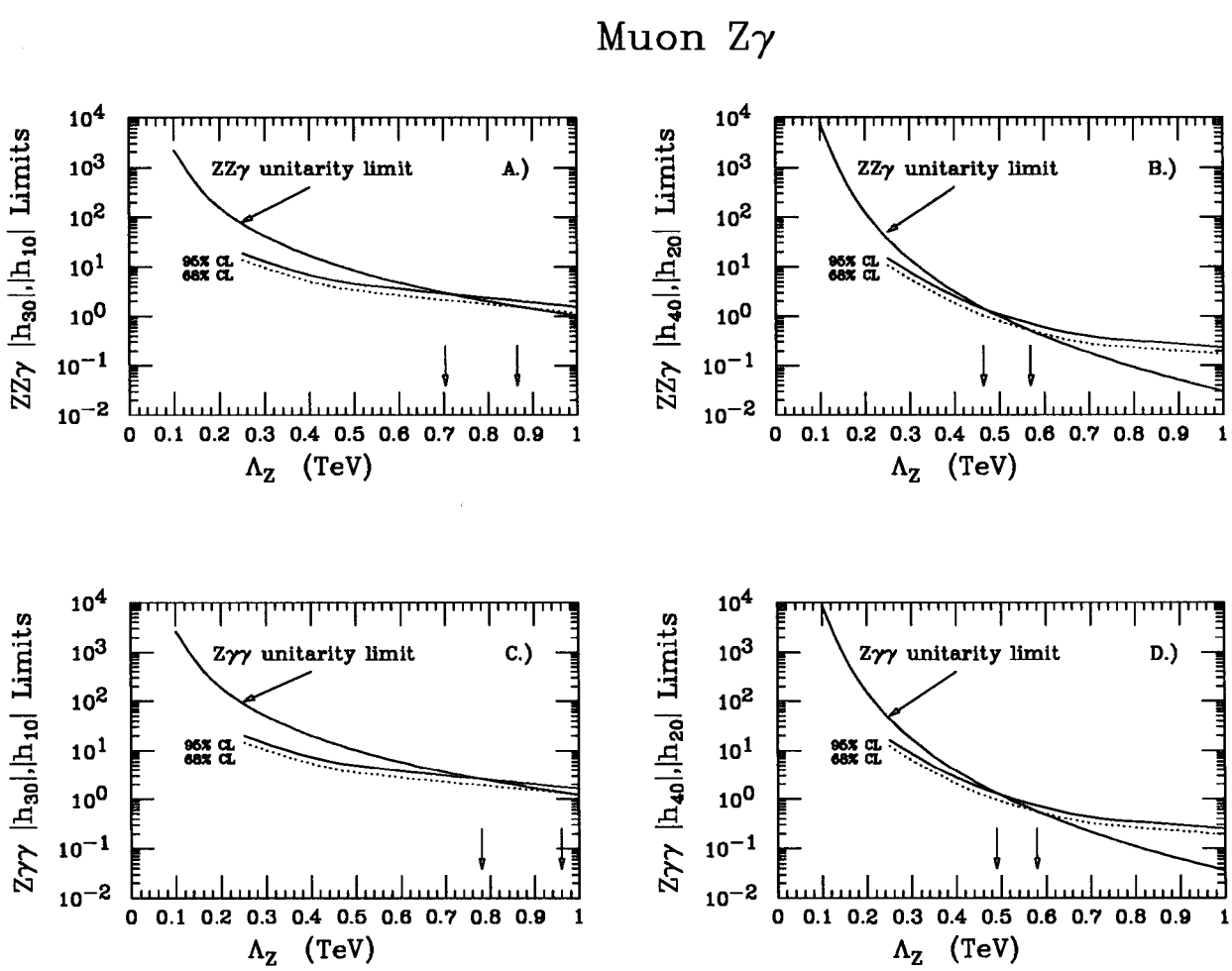


**Figure 8.14**: In A) and B), limits on $h^Z_{10,30}$ and $h^Z_{20,40}$ as a function of $\Lambda_Z$. In C) and D), limits on $h^\gamma_{10,30}$ and $h^\gamma_{20,40}$ as a function of $\Lambda_Z$. The 68% and 95% CL limits from the data are shown as well as the unitarity limit. The regions above the curves are not allowed.

the Compton wavelength of the $W$ and $Z$ bosons, $\lambda\!\!\!^{-}_{W,Z} = \hbar/M_{W,Z}c$. The distance scale sensitivity to which the above energy scale sensitivities correspond are, at the 95% CL,

$$L_W^{\Delta\kappa} \leq 1.4 \times 10^{-4} \text{ fm} = 0.057\ \lambda\!\!\!^{-}_W$$

$$L_W^{\lambda} \leq 1.2 \times 10^{-4} \text{ fm} = 0.049\ \lambda\!\!\!^{-}_W$$

$$L_W^{\tilde{\kappa}} \leq 0.3 \times 10^{-4} \text{ fm} = 0.012\ \lambda\!\!\!^{-}_W$$

$$L_W^{\tilde{\lambda}} \leq 1.4 \times 10^{-4} \text{ fm} = 0.057\ \lambda\!\!\!^{-}_W$$

The results for $ZZ\gamma$ and $Z\gamma\gamma$ are, at the 95% CL:

$$\Lambda_Z^{h_{30,10}^Z} \geq 700\ GeV$$

$$\Lambda_Z^{h_{40,20}^Z} \geq 460\ GeV$$

$$\Lambda_Z^{h_{30,10}^\gamma} \geq 780\ GeV$$

$$\Lambda_Z^{h_{40,20}^\gamma} \geq 500\ GeV$$

These form factor scales correspond to distance scale sensitivities for probing possible internal structure of the $Z$ boson of:

$$L_Z^{h_{30,10}^Z} \leq 2.8 \times 10^{-4} \text{ fm} = 0.129\ \lambda\!\!\!^{-}_Z$$

$$L_Z^{h_{40,20}^Z} \leq 4.3 \times 10^{-4} \text{ fm} = 0.199\ \lambda\!\!\!^{-}_Z$$

$$L_Z^{h_{30,10}^\gamma} \leq 2.5 \times 10^{-4} \text{ fm} = 0.115\ \lambda\!\!\!^{-}_Z$$

$$L_Z^{h_{40,20}^\gamma} \leq 3.9 \times 10^{-4} \text{ fm} = 0.180\ \lambda\!\!\!^{-}_Z$$

## 8.6 Summary

I have presented measured cross sections times branching ratios for both $W\gamma$ and $Z\gamma$ processes as a function of the photon $E_T$ threshold, as well as various cross section ratios as a function of the photon $E_T$ threshold. These measurements, which are based on limited statistics, are all consistent with the SM predictions. Perhaps the most interesting result from the cross section measurements is that the ratio of the $W\gamma$ cross section to the $Z\gamma$ cross section is measured to be of order 3-4. This is lower than the ratio of inclusive $W$ and $Z$ cross sections (which is about 10.9) because of (destructive) interference effects that occur between diagrams in the $W\gamma$ system. The production of $W\gamma$ events is suppressed, which in turn decreases the cross section ratio since no similar effect occurs in the $Z\gamma$ system.

Limits on possible anomalous couplings between the $W$ and photon and the $Z$ and photon have also been extracted. The limits are extracted based on the photon $E_T$ spectra from our diboson samples. In models that assume non-zero anomalous couplings, there is an enhancement of high $E_T$ photons in both $W\gamma$ and $Z\gamma$ events. The 95% CL limits are consistent with the SM values of 0 for all possible couplings in both the $W\gamma$ and $Z\gamma$ systems. However, the most likely value of the $Z\gamma$ couplings are not 0, as shown in Figs. 8.8a-d. This is due to one $Z\gamma$ event that has a photon with $E_T$ of about 64 $GeV$. Whether or not this event is a fluctuation or a sign for potential new physics remains to be seen as more data is collected.

From the limits on anomalous couplings, limits are derived on various static electromagnetic moments of the $W$ boson and transition moments of the $Z$ boson. In addition, the limits on anomalous couplings are used to set limits on form factor energy scales.

# Chapter 9

# Conclusion

The cross section times branching ratio for $W\gamma$ and $Z\gamma$ processes are measured for various values of minimum photon $E_T$ in the muon channel using data collected at CDF. Various cross section ratios are calculated based on those results. Limits are measured and placed on possible anomalous couplings for these diboson processes. Within the Standard Model, the couplings $\Delta\kappa = \kappa - 1$, $\lambda$, $\tilde{\lambda}$ and $\tilde{\kappa}$ are all zero for $W\gamma$ processes, and $h_{i0}^{Z}$, $h_{i0}^{\gamma}$ (where $i = 1$, 2, 3 or 4) are all zero for $ZZ\gamma$ and $Z\gamma\gamma$ processes, respectively. These couplings are zero within the SM because the $W$ and $Z$ bosons are considered to be fundamental point particles, and non-zero values on one or more of the couplings would mean there are non-zero form factors due to an inner structure to these bosons. The various anomalous couplings are directly related to electromagnetic moments of the $W$ and $Z$ bosons, and limits on those moments are extracted from the limits on anomalous couplings. Using the limits on anomalous couplings, limits are extracted on the form

factor energy scales, $\Lambda_{W,Z}$. The results of this analysis are summarized below and are consistent with expectations from the SM.

## 9.1 Summary of Results

Central photons ($|\eta| < 1.1$) with $E_T$ above 7 $GeV$ and which are separated from the muon by at least $\Delta R = 0.7$, are used to measure the production cross section times branching ratio for $W + \gamma$ and $Z + \gamma$ processes in the muon channel. Seven $W\gamma$ and 4 $Z\gamma$ candidate events for each process. Based on a measured integrated luminosity of $18.6 \pm 0.7\ pb^{-1}$, the cross sections times branching ratios are found to be $9.0 \pm 6.4\ pb$ for $W\gamma$ processes and $6.6 \pm 3.4\ pb$ for $Z\gamma$ processes. The procedures used to measure the cross section times branching ratio for a photon $E_T$ cut of 7 $GeV$ are repeated for photon $E_T$ cuts of 11 and 15 $GeV$. Their respective values are, for $W\gamma$ processes, $4.8 \pm 8.6\ pb$ and $6.8 \pm 10.3\ pb$, and for $Z\gamma$ processes, $3.8 \pm 2.7\ pb$ and $2.3 \pm 2.4\ pb$. The uncertainties on these results are the statistical and systematic uncertainties added in quadrature.

Cross section ratios are calculated based on the results mentioned above. The results are:

7 $GeV$:

$$\sigma \cdot BR(W\gamma)/\sigma \cdot BR(W) = 0.4 \pm 0.3\%$$

$$\sigma \cdot BR(Z\gamma)/\sigma \cdot BR(Z) = 3.3 \pm 1.7\%$$

$$\sigma \cdot BR(W\gamma)/\sigma \cdot BR(Z\gamma) = 1.4^{+1.8}_{-1.0}$$

11 $GeV$:

$$\sigma \cdot BR(W\gamma)/\sigma \cdot BR(W) = 0.2 \pm 0.3\%$$

$$\sigma \cdot BR(Z\gamma)/\sigma \cdot BR(Z) = 1.9 \pm 1.4\%$$

$$\sigma \cdot BR(W\gamma)/\sigma \cdot BR(Z\gamma) = 1.3^{+2.6}_{-2.5}$$

15 $GeV$:

$$\sigma \cdot BR(W\gamma)/\sigma \cdot BR(W) = 0.3 \pm 0.4\%$$

$$\sigma \cdot BR(Z\gamma)/\sigma \cdot BR(Z) = 1.2 \pm 1.2\%$$

$$\sigma \cdot BR(W\gamma)/\sigma \cdot BR(Z\gamma) = 2.9^{+5.5}_{-3.5}$$

All of these cross section ratios are consistent with the SM within the quoted uncertainties.

The observed photon $E_T$ spectra from the $W\gamma$ and $Z\gamma$ samples (using a minimum photon $E_T$ cut of 7 $GeV$) are compared to Monte Carlo spectra in order to carry out a maximum likelihood analysis. The results of that analysis are limits on possible anomalous couplings between the $W$-photon and $Z$-photon. The 95% CL limits are measured, for one non-zero anomalous coupling at a time, to be:

For $WW\gamma$:

$$-3.7 < \Delta\kappa < 3.7$$

$$-1.2 < \lambda < 1.2$$

$$-3.8 < \tilde{\kappa} < 3.8$$

$$-1.2 < \tilde{\lambda} < 1.2$$

For $ZZ\gamma$:

$$-4.6 < h^Z_{30} < 4.6$$

$$-1.1 < h_{40}^{Z} < 1.1$$

$$-4.6 < h_{10}^{Z} < 4.6$$

$$-1.1 < h_{20}^{Z} < 1.1$$

For $Z\gamma\gamma$:

$$-4.6 < h_{30}^{\gamma} < 4.6$$

$$-1.1 < h_{40}^{\gamma} < 1.1$$

$$-4.6 < h_{10}^{\gamma} < 4.6$$

$$-1.1 < h_{20}^{\gamma} < 1.1$$

All of the above couplings are consistent with the SM values of 0.

Using the limits on anomalous couplings, it is possible to derive limits on static electromagnetic multipole moments of the $W$ boson and transition moments of the $Z$ boson. The 95% CL limits on the EM moments are found to be:

$W$ Boson Static Moments:

Magnetic Dipole: $-2.0 < (g_W - 2) < 2.0$

Electric Quadrupole: $-2.7 < (q_W^e - 1) < 2.7$

Electric Dipole: $-2.0 < (d_W - 1) < 2.0$

Magnetic Quadrupole: $-2.7 < (q_W^m - 1) < 2.7$

$Z$ Boson Transition Moments:

Electric Dipole: $-1.6 < \delta_{Z_T}^{*} < 1.6$

Magnetic Quadrupole: $-9.0 < q_{Z_T}^{m} < 9.0$

Magnetic Dipole: $-1.6 < g_{Z_T}^{*} < 1.6$

Electric Quadrupole: $-9.0 < q^e_{Z_T} < 9.0$

The limits on anomalous couplings have been used to determine the experimental sensitivity to possible form factor (compositeness) scales. The experimental limits on the form factor scales are, for $W\gamma$ processes:

$$\Lambda_W^{\Delta\kappa} \geq 1.4\ TeV$$

$$\Lambda_W^{\lambda} \geq 1.7\ TeV$$

$$\Lambda_W^{\tilde{\kappa}} \geq 7.4\ TeV$$

$$\Lambda_W^{\tilde{\lambda}} \geq 1.4\ TeV$$

These values can be translated into distance scale sensitivitites for probing possible internal structure of the $W$ boson of order $L_W = \hbar c/\Lambda_W$:

$$L_W^{\Delta\kappa} \leq 1.4 \times 10^{-4}\ \text{fm} = 0.057\ \lambda\!\!\!^{-}_W$$

$$L_W^{\lambda} \leq 1.2 \times 10^{-4}\ \text{fm} = 0.049\ \lambda\!\!\!^{-}_W$$

$$L_W^{\tilde{\kappa}} \leq 0.3 \times 10^{-4}\ \text{fm} = 0.012\ \lambda\!\!\!^{-}_W$$

$$L_W^{\tilde{\lambda}} \leq 1.4 \times 10^{-4}\ \text{fm} = 0.057\ \lambda\!\!\!^{-}_W$$

For $Z\gamma$ processes, the form factor limits are:

$$\Lambda_Z^{h^Z_{30,10}} \geq 700\ GeV$$

$$\Lambda_Z^{h^Z_{40,20}} \geq 460\ GeV$$

$$\Lambda_Z^{h^\gamma_{30,10}} \geq 780\ GeV$$

$$\Lambda_Z^{h^\gamma_{40,20}} \geq 500\ GeV$$

These form factor scales correspond to distance scale sensitivities for probing possible internal structure of the $Z$ boson of:

$$L_Z^{h_{30,10}^Z} \leq 2.8 \times 10^{-4} \text{ fm} = 0.129 \; \lambda\!\!\!^{-}_Z$$

$$L_Z^{h_{40,20}^Z} \leq 4.3 \times 10^{-4} \text{ fm} = 0.199 \; \lambda\!\!\!^{-}_Z$$

$$L_Z^{h_{30,10}^\gamma} \leq 2.5 \times 10^{-4} \text{ fm} = 0.115 \; \lambda\!\!\!^{-}_Z$$

$$L_Z^{h_{40,20}^\gamma} \leq 3.9 \times 10^{-4} \text{ fm} = 0.180 \; \lambda\!\!\!^{-}_Z$$

## 9.2 Future Opportunities

The best opportunity (in the near future) of getting better results is analyzing larger data samples. The 1994-95 Tevatron run (Run 1B) is currently underway and there are hopes of recording 5-10 times as much data to tape than is available from Run 1A. Diboson production is a fairly rare process, and as data samples grow the cross sections times branching ratios, cross section ratios, limits on anomalous couplings, and limits on electromagnetic moments should improve.

The analysis of photons in the CDF environment has typically been limited to a pseudorapidity region of $|\eta| < 1.1$, or the central region of the detector. If the photon acceptance was extended into the plug and forward calorimeters, one would have larger statistics as well as the chance to begin exploring the expected radiation zero in $W\gamma$ events. In the lab frame the radiation zero is expected to show itself in the form of a dip in the distribution of photon pseudorapidity minus lepton pseudorapidity. The dip should occur for larger differences, and this effect would be enhanced using plug and

forward photons, since muons are detected in the central region. Preliminary studies have begun to look at the photon backgrounds in the plug region of CDF. A second possibility for the electron channel would be to look at $W$ decays where the electron goes into the plug region while the photon goes into the central region. This also would allow larger pseudorapidity differences to occur.

Larger statistics would allow for more detailed studies of kinematic distributions for both $W\gamma$ and $Z\gamma$ events. In this analysis the photon $E_T$ spectrum is fitted to extract limits on anomalous couplings. It may be possible to try and fit *several* kinematic variables simultaneously to maximize the sensitivity to anomalous couplings. For instance, the photon $E_T$, the photon-lepton separation, and the transverse cluster mass (for $W\gamma$) or dilepton-photon invariant mass (for $Z\gamma$) all contain useful information in terms of anomalous couplings. Using *all* of that information together could produce better results. All of this future work would allow us to have a better understanding about several properties of the $W$ and $Z$ bosons, the most important being whether or not they are truly fundamental point particles as required by the Standard Model.

# Appendix A

# The Central Muon Upgrade at CDF

I describe here the Central Muon Upgrade system (CMP) at CDF. We designed, built and tested the CMP at the University of Illinois at Urbana-Champaign [26, 55], and later installed the detector at CDF in between the 1988-89 and 1992-93 data-taking runs. The motivation for this detector upgrade was to have a better muon identification system by greatly reducing the effects of hadrons getting through the material in front of the CMU (i.e. the calorimeters) and being misidentified as muons. In the 1988-89 run, when only the CMU detector existed, this "hadronic punchthrough" created high muon trigger rates and backgrounds to interesting events such as $W$ and $Z$ decays. The CMP has the benefit of 60 cm of additional steel to reduce punchthrough in the CMP chambers by a factor of $\sim$ 20. This reduction in punchthrough was necessary in the 1992-93 CDF run because the average luminosity delivered by the Tevatron increased by a factor of about 4-5, and higher luminosities means higher rates of punchthrough. For the regions

where the CMP overlaps the CMU, the CMP provides confirmation of CMU hits and the punchthrough reduction takes effect.

Section A.1 describes the general design and construction of the CMP drift chambers. Section A.2 describes some details of the data acquisition electronics used to obtain data from the chambers. Section A.3 shows the performance of the chambers using cosmic ray and $p\bar{p}$ collision data.

## A.1 Design and Construction of the CMP

The CMP system consists of drift chambers, which are rectangular aluminum tubes 2.54 cm by 15.24 cm in cross section and 6.4 m long. A small number of chambers of length 6.1 m were also installed on the bottom of the detector due to space limitations. Four individual chambers were glued together in a half-cell staggered manner (see Figure A.1), forming the 'stacks' that were installed at CDF. The chambers are staggered in order to eliminate left-right ambiguities, as well as reduce the time needed to detect hits from a muon traveling through a stack by a factor of two. Note that in Figure A.1 there is also a description of chamber residuals, which are discussed below in section A.3.

Each chamber has a single 50 $\mu$m gold-plated tungsten anode wire extending down the center. Copper cathode strips are made along a single PC board which is glued to the top and bottom of the extrusion. There are eight strips ($\frac{1}{4}$" $\times$ 21') on either side of a wide (1" width), central strip. A PVC wire support is used due to the long length of the chambers in order to prevent electrostatic instabilities due to wire sag. The anode

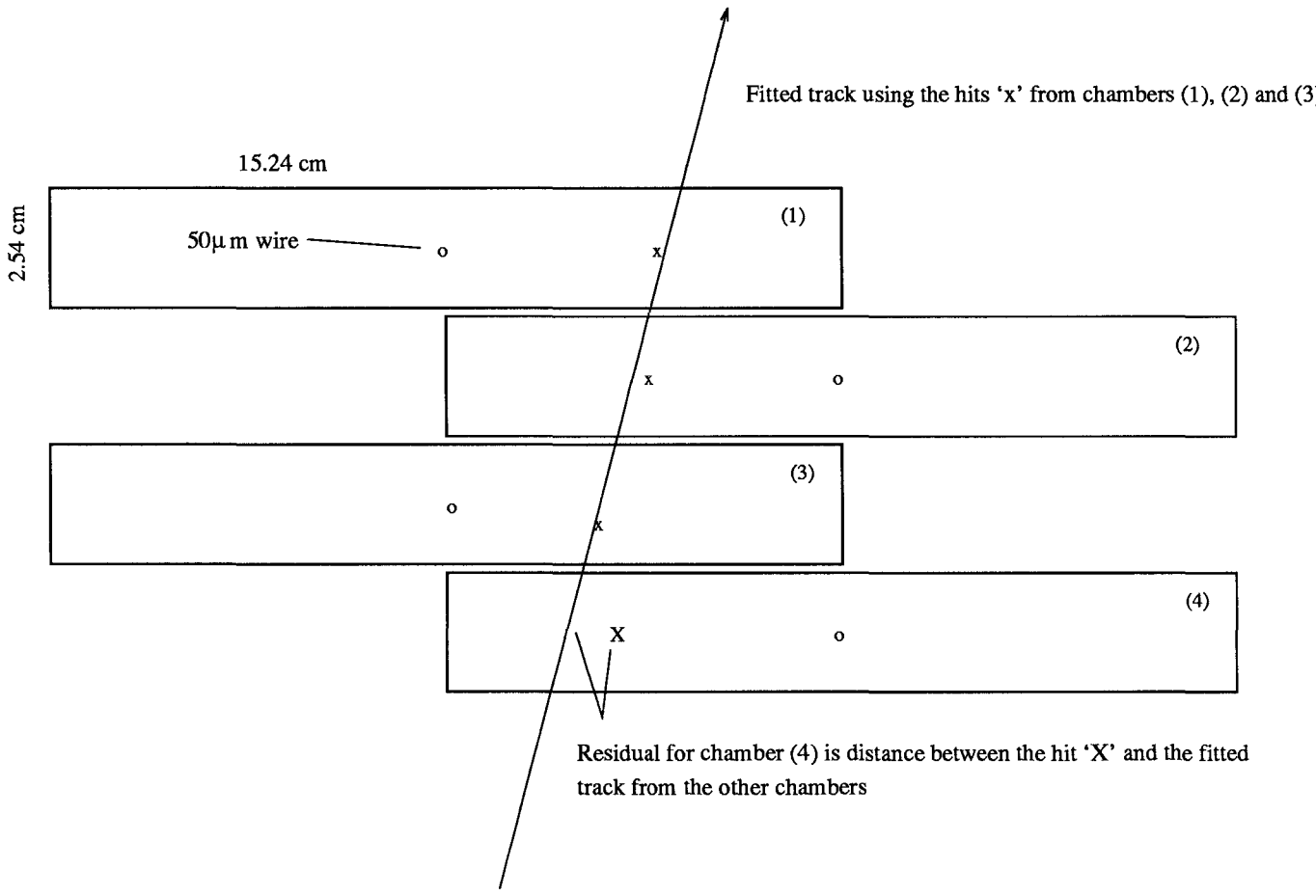


**Figure A.1**: Schematic of a CMP stack. Four chambers are glued together in the staggered positions shown here. Also drawn in is a description of chamber residuals, which give the tracking resolution of the chambers. See section A.3 for more details.

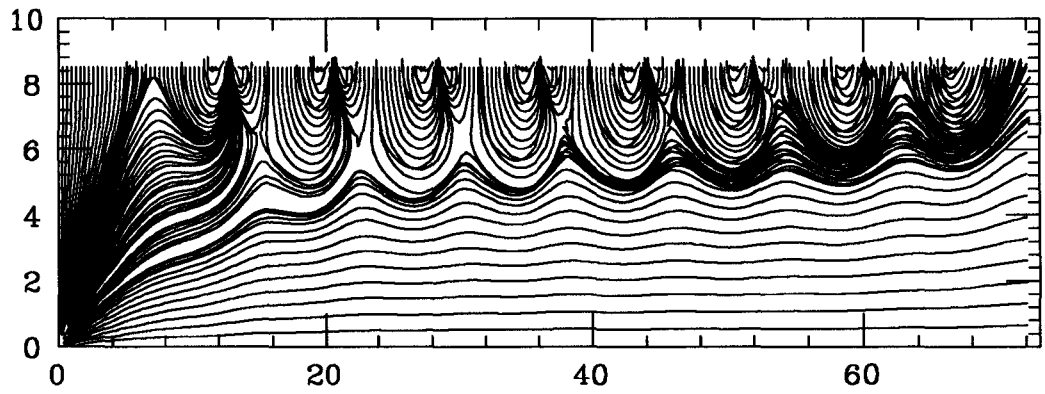


**Figure A.2**: Electric field lines in one quadrant of a CMP chamber. The axes represent the chamber dimensions in millimeters.

wire is held at +5400 V and the central strip is held at +2800 V. These voltages are selected because the chambers then operate in proportional mode. The other strips are held at voltages which decrease from the central strip in eight equal steps. The stepped down voltages are created by a $20\text{M}\Omega \times 8$ hybrid divider resistor which are fed through an endplate to the pads. Together, the voltage differences between the strips and anode wire provide a fairly uniform electric field in most of the drift volume, as shown in Figure A.2. Note that the outside strips are grounded to the aluminum extrusion by silver epoxy, and that they are half the width of the other strips to keep the equipotential lines at the edge of the chamber the same shape as those for the rest of the chamber.

The chambers operate filled with a mixture of 50% Argon-50% Ethane gas at 1 atm. The Argon-Ethane is bubbled through an isopropyl alcohol bath which is kept at $-7°$ C, and is then sent to the chambers. A 0.5% volume of isopropyl alcohol mixed in with the Argon-Ethane assists in preventing electric discharges from occuring within the

chambers. When a charged particle, such as a muon, passes through the gas, the gas is ionized. The electrons from the ionization then drift along the electric field lines toward the anode wire. This mixture of gas is used because the drift velocity of the electrons plateaus and remains constant at 43 mm/$\mu$s with respect to the electric field. When the drift electrons are close to the anode wire an electron "avalanche" occurs due to multiple ionizations in the large electric field close to the wire. With the pad voltage at 2800 V and the anode wire voltage at 5400 V the Argon-Ethane mixture used in the CMP has a measured gas gain of about $6 \times 10^4$. The large number of electrons create a signal which is pre-amplified at the end of the chamber and then sent over a 30' twisted pair cable to a second stage of amplification followed by discrimination. Timing information is derived using TDCs. Details about the electronics are described below.

The voltages we use are well below streamer mode, which is important because of the position of the Main Ring relative to some of the CMP chambers. The chambers placed on top of the CDF detector lie directly beneath the Main Ring. Sprays of charged particles from the Main Ring bombard the CMP, thus producing large currents within the chambers which potentially can cause the high voltage power supplies to sag or trip. This is avoided by keeping the CMP in proportional mode, where the gain is lower than in streamer mode.

## A.2 CMP Electronics

Every CMP stack which is installed at CDF has a board with preamplifiers attached to it. The wire signals which are created as a result of a charged particle passing through the stack are taken out through a 2200 pF blocking capacitor and fed to a Radeka preamp chip [18]. A schematic of the circuit which is contained on the board attached to one end of a stack is shown in Figure A.3. The amplified signals are sent over 100 $\Omega$ shielded, twisted pair cables to an isolation transformer board, which is in turn attached to an Amplifier-Shaper-Discriminator (ASD) card located in the CDF collision hall. With muon signals of order 1 V, the ASD threshold was set at 120 mV during the 1992-93 run. The signals coming out of the ASD are differential ECL signals, and they are sent to a counting room via custom ribbon cables. These signals are fed into LeCroy 1879 TDCs [18]. The TDCs provide drift times which are used along with the drift velocity and $t_0$ to calculate the coordinates, transverse to the beam direction, of where the particle traversed a particular chamber. The $t_0$ is defined as the time difference between when the TDC time window starts and the earliest arrival time of signals at the TDC. The TDC time window begins a fixed time after proton and antiproton bunches arrive in the interaction region in order to leave time for propagation of signals to the counting room. If two or more chambers record hits a fit can be made which reconstructs the path that the charged particle took as it made its way through the chambers. Such information is used at the trigger level to decide if the track, or 'stub', matches to any stubs in the CMU within a $\phi$ angle of 5° (see Chapter 4). The CMP stubs used in the trigger are

formed between either chambers 1 and 3 or chambers 2 and 4 (see Fig. A.1) in order to reduce the effects of single hit inefficiency. Muon reconstruction software also make use of calorimeter information. Real muons are identified as particles which not only make it through large amounts of material to the muon detectors, but also deposit small amounts of hadronic and electromagnetic energy in the calorimeter towers that they traverse.

## A.3 Performance of the CMP in 1992-93 Run

The CMP performed very well during Run 1A. Some general characteristics of the chambers include the drift velocity mentioned above and an average tracking resolution. The drift velocity, $v_d$, is calculated using drift times from 3 chambers, the geometry of the wires, and the assumption that the drift velocity is the same in all four chambers of a stack:

$$v_d = \frac{a}{bt_1 + ct_2 + dt_3} \tag{A.1}$$

where $a$, $b$, $c$, and $d$ are constants that depend on the relative positions of the wires, and $t_1$, $t_2$ and $t_3$ are the three drift times for a given track.

A residual for a chamber refers to the distance between a hit in a specific chamber and an extrapolated track based on hits in the other chambers of the stack. If, for example, a muon passes through all four chambers of a stack, one can use three of the four chambers to fit the path the muon traveled. That fit line can be extrapolated through the remaining chamber, and the distance between the line and the hit in that chamber is

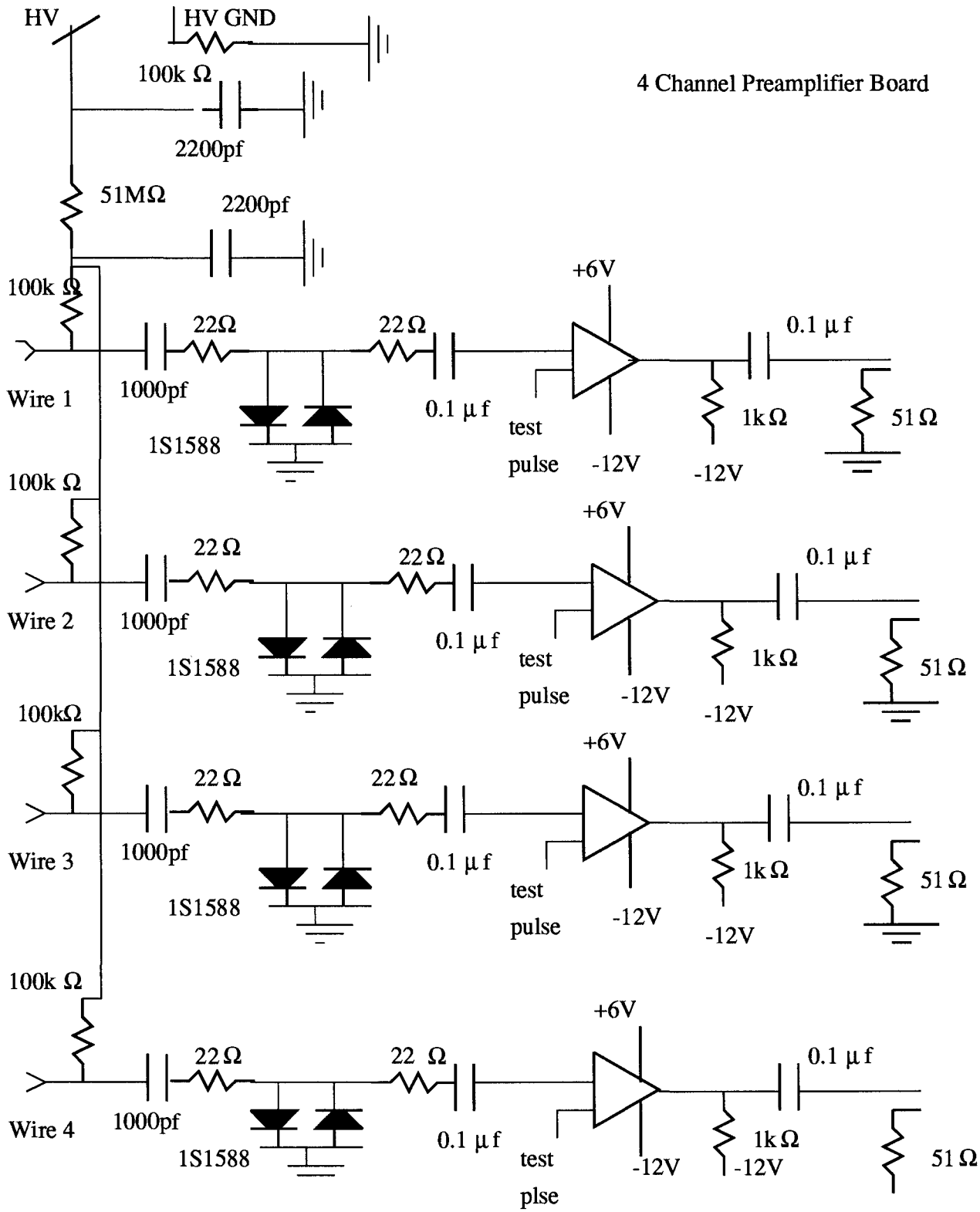


**Figure A.3**: Schematic of CMP preamp board. These boards are connected directly to each stack.

the residual. Note that the drift distance in a chamber is equal to $v_d \cdot (t_{drift} - t_0)$. Figure A.1 above gives a visual description of how residuals are measured. Figure A.4 shows a typical distribution of the tracking residuals. The resolution is the width of the residual distribution, and is typically about 250 $\mu$m.

As mentioned in Chapter 3, there are several regions in $\phi$ with gaps in the CMP system due to the lack of supporting structures at CDF in those regions. Figures A.5a-b show the $\eta$ and $\phi$ distributions of muons which went through the CMP detector.

The purpose of the CMP, as stated above, is to help eliminate hadronic punchthrough which can be misidentified as muons, and to thereby reduce trigger rates and improve the muon identification. Figure A.6 shows that indeed the CMP does help eliminate a large amount of the punchthrough. The solid histogram shows the energy deposited in the hadronic calorimeter (CHA) for particles which passed through *both* the CMU and CMP The dashed histogram shows the same variable for muons which passed through *only* the CMU. Notice that the high end tail is nearly eliminated for muons which went through both detectors. The CMP requirement removes particles that are, for example, part of jets and make it out to the CMU but cannot penetrate the extra steel in front of the CMP. A different way of observing the effect the CMP has on reducing punchthrough and backgrounds from the data is to plot the muon $P_T$ distributions from $W$ candidate decays for CMU-only muons and CMU plus CMP muons. Figure A.7a is the CMU-only distribution and Figure A.7b shows the CMU with CMP distribution. The CMU-only muon $P_T$ distribution shows a small peak below 30 $GeV/c$, which is the result of $W$ backgrounds (i.e. punchthrough). The combined CMU-CMP distribution shows the

usual Jacobian peak with no hints of large backgrounds. The muon $\eta$, $\phi$ and residual distributions all came from the inclusive $W$ sample, as did the muon $P_T$ spectra. Figure A.6 uses data from an inclusive muon sample which required the muon $P_T$ to be above 15 $GeV/c$. Overall, the CMP provides a very efficient means of identifying real muons ($\approx$ 97% efficient) in the messy CDF environment.

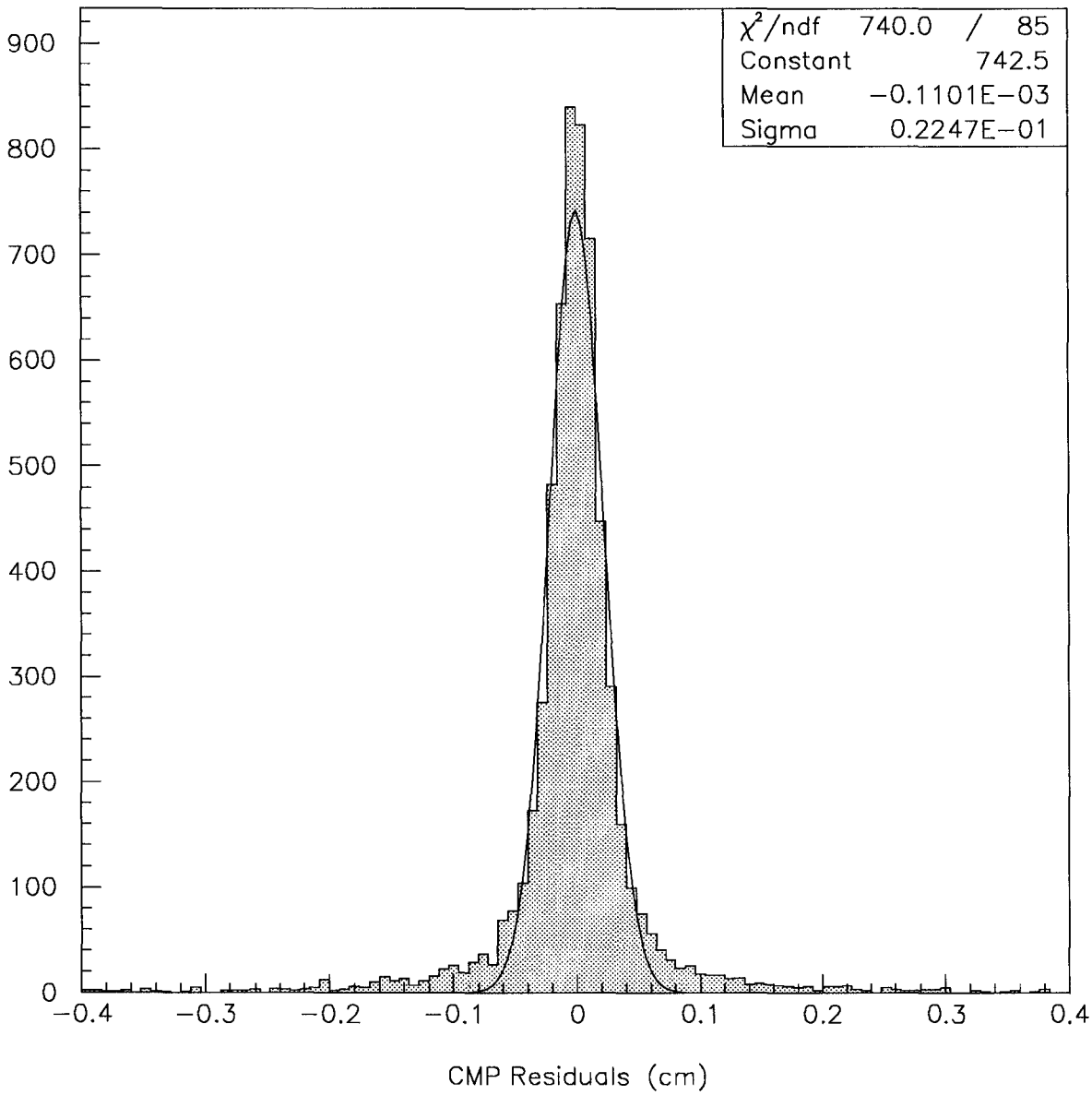


**Figure A.4**: CMP residuals from inclusive $W$ data. A residual for a single chamber is defined as the distance between the track of a particle reconstructed from the surrounding chambers and the point where the particle passed through the chamber in question.

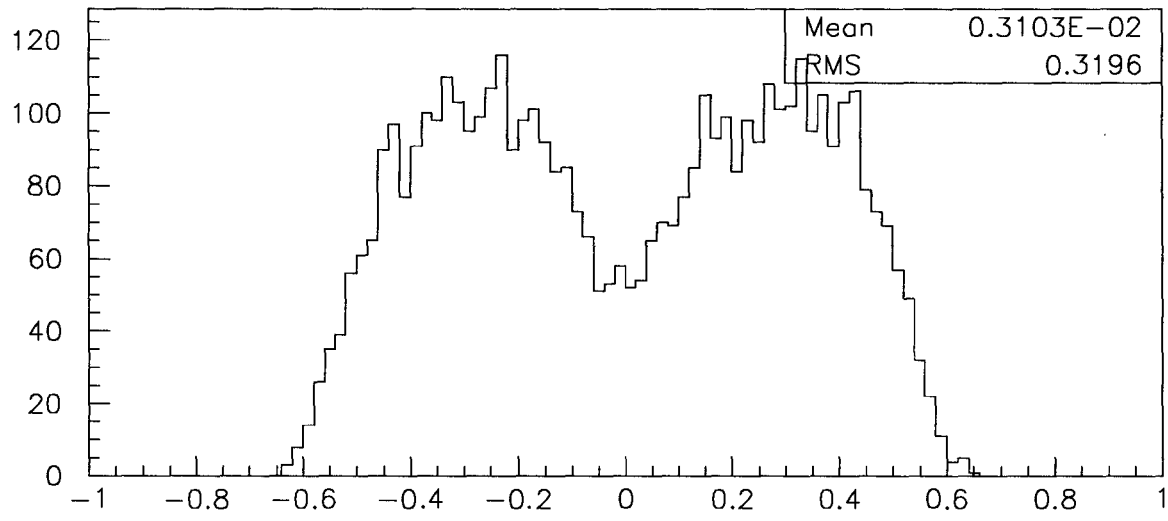


a) Eta of muons in CMP

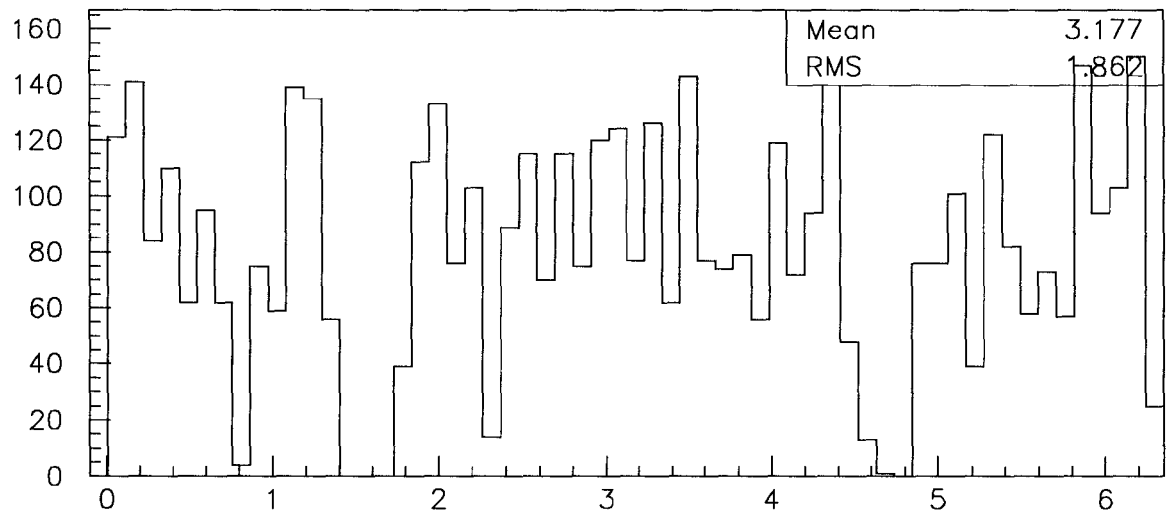


b) Phi of muons in CMP

**Figure A.5**: $\eta$ and $\phi$ distributions of muons which passed through the CMP.

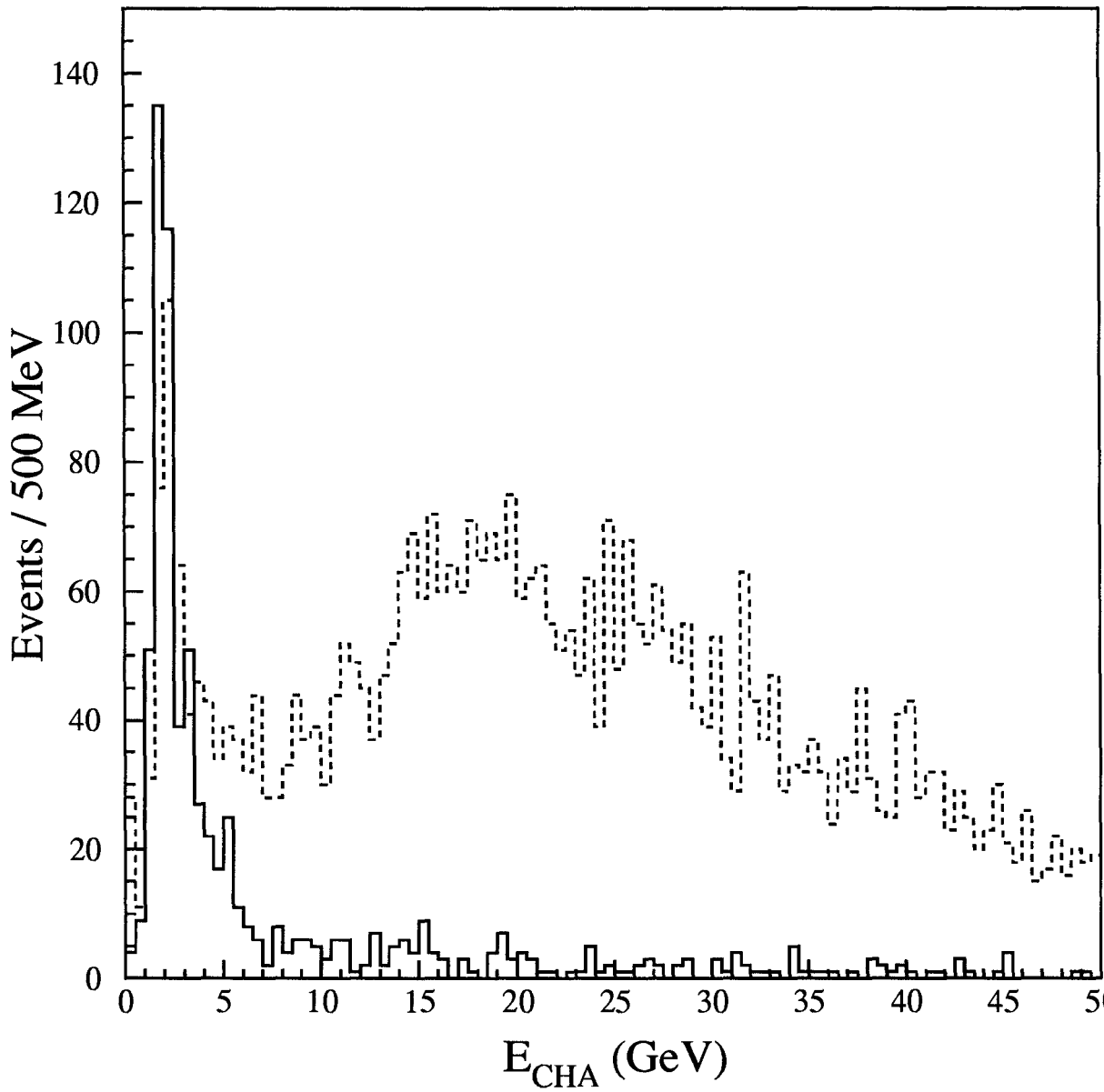


**Figure A.6**: Distributions of hadronic energy for muon candidates that only passed through the CMU (dashed line) and candidates that passed through both the CMU and CMP (solid line). The large tail for CMU-only particles is caused by hadrons that punch through the calorimeter.

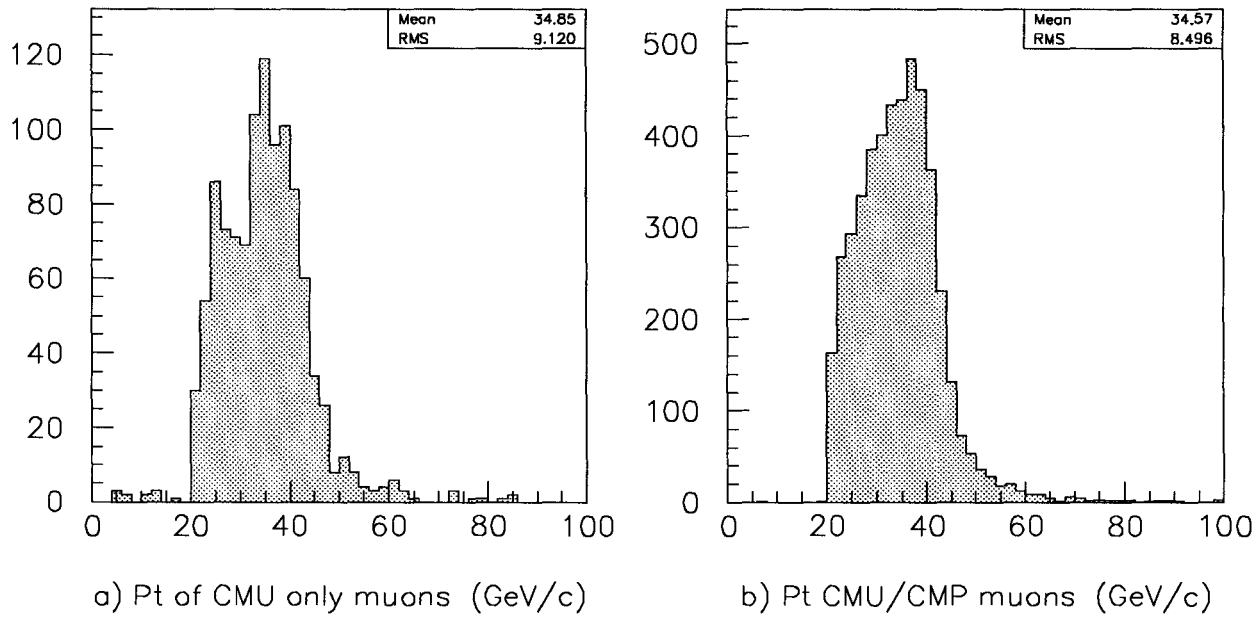


**Figure A.7**: Muon $P_T$ spectra for a) CMU-only muons, and b) CMU plus CMP muons, resulting from $W$ decays. Figure a) shows background peaking below 30 $GeV/c$, the result of punchthrough.

# Appendix B

# CDF Calorimeter Clustering Algorithm

Photon identification at CDF depends on accurately determining the shower shapes and energies in the calorimeter. I will briefly describe the clustering algorithm which results in good electron and photon identification at CDF.

The calorimeter is segmented into towers of size 0.1 units of $\eta$ and 15° in $\phi$. Electromagnetic clustering was designed with the goal of locating all the energy in an EM shower that came from a single photon or electron. The energy clusters for a given photon or electron are formed around seed towers with electromagnetic (EM) $E_T$ of at least 3 $GeV$. If there are two or more neighboring towers with EM $E_T$ above 3 $GeV$, then the tower with the highest $E_T$ is designated as the seed tower for that cluster. In the CEM the clustering is limited to the two towers which are nearest to the seed tower in $\eta$. Nearest towers in $\phi$ are not used because $\phi$ cracks between adjacent towers in the CEM are larger

than a typical electromagnetic shower, and therefore little energy is deposited across the cracks [14]. A cluster is formed when the ratio of hadronic energy to electromagnetic energy is 0.125 or less and the total $E_T$ from the seed and adjacent towers is at least 5 $GeV$. Clusters which satisfied these criteria were referred to as "ELES objects" at CDF, and it was from $W \rightarrow \mu\nu_\mu$ and $Z \rightarrow \mu^+\mu^-$ events which contained ELES objects that the $W\gamma$ and $Z\gamma$ samples used in this analysis were extracted.

# Appendix C

# CDF Jet Clustering Algorithm

The background estimation made a good deal of use of jet information, both from the inclusive $W$ and $Z$ samples as well as from the 16 $GeV$ photon sample. The general jet clustering algorithm is described below.

Energy deposits from QCD jets are in general more spread out in the detector (in $\eta - \phi$ space) than those from electrons or photons. Because of this, the jet finder uses a cone of $\sqrt{\Delta\eta^2 + \Delta\phi^2} = 0.7$ to define a jet rather than individual calorimeter towers. The jet clustering begins by searching for seed towers with $E_T$ of at least 1 $GeV$. For jets it does not matter if the energy is more electromagnetic or hadronic. Each seed tower has a cone of 0.7 put around it. If two or more seed towers are within the same cone the tower with the highest $E_T$ is designated as the seed of that jet. All towers within the seed cone that have more than 0.200 $GeV$ of $E_T$ deposited in them are then recorded, and the $E_T$-weighted cluster centroid of the cone is determined.

If the $E_T$-weighted centroid does not have the same $\eta - \phi$ coordinates as the centroid of the seed cone being used, a new cone of 0.7 is formed around the $E_T$-weighted centroid. All towers in the new cone that have $E_T$ above 0.200 $GeV$ are summed together. Depending how far from the seed centroid this new cone is, some towers which were originally part of the cluster may be subtracted out and others which were not part of the original cluster may be added in. The $E_T$-weighted centroid of this new cluster is then determined, and if it does not match with the previous centroid the process is repeated. This continues until there are no new towers added or subtracted to the jet cluster [56]. The choice of a cone size of 0.7 is chosen based on the distribution of energy flow with respect to the jet axis in events dominated by two jets. Most of the jet energy is contained within a cone of 0.7. From Monte Carlo studies, it was determined that jets with observed energies of 5 $GeV$ could be identified with this algorithm [57].

# Appendix D

# Monte Carlo Cross Section and Acceptance Calculations

The Baur Monte Carlos generate $W\gamma$ and $Z\gamma$ event samples which are then run through a CDF detector simulation and standard analysis code. This process leads to theoretical predictions for cross sections and event yields. It also provides the geometrical and kinematic acceptance for these types of events which is used for the experimental cross section measurement. In this appendix I discuss how the cross section after all analysis cuts, i.e. the *expected* cross section, is determined from the generated cross section from the Monte Carlo as well as the details involved in the $Z\gamma$ acceptance calculation.

## D.1 Monte Carlo Cross Sections

The Baur Monte Carlos generate $W\gamma$ and $Z\gamma$ events with some overall cross section based on the matrix elements that describe the production of these types of events. These requirements consist of photon and muon $P_T$ above 1 $GeV/c$, photon and muon maximum pseudorapidity of 6, and photon-muon separation of $\Delta R > 0.3$. The SM Baur generated cross section times branching ratio, $\sigma \cdot BR(V+\gamma)_{gen}$, where $V = W, Z$, is 90.0 $pb$ for $W\gamma$ and 19.8 $pb$ for $Z\gamma$. It is important to keep in mind that these generated cross sections are recorded before all the analysis selection requirements are made on the muon and photon. What is needed to compare to experimental measurements is the cross section after all analysis requirements are made and all selection efficiencies are accounted for. This is the cross section times branching ratio after selection cuts, $\sigma \cdot BR(V+\gamma)_{cuts}$.

The predicted number of events for either $W\gamma$ or $Z\gamma$ processes can be related to both cross sections:

$$N_{pred}^{V\gamma} = \sigma \cdot BR(V+\gamma)_{cuts} \cdot \int Ldt \cdot (A \cdot \epsilon)_{V\gamma} \tag{D.1}$$

$$N_{pred}^{V\gamma} = \sigma \cdot BR(V+\gamma)_{gen} \cdot \int Ldt \cdot (A' \cdot \epsilon)_{V\gamma} \tag{D.2}$$

The term $A$ is the overall kinematic and geometrical acceptance presented in Ch. 6, and $\epsilon$ is the total efficiency for all analysis requirements (i.e. the product of the total muon and photon efficiencies from Ch. 5). The term $A'$ is the overall kinematic and geometrical

acceptance for finding central photons with $ET > 7\ GeV$ and $\Delta R > 0.7$ from the *generated* samples with the relaxed kinematic requirements on the photon mentioned above. Both acceptances are obtained from the Monte Carlo.

Using the above equations, one can relate the cross section after all selection cuts, $\sigma \cdot BR(V+\gamma)_{cuts}$, to $\sigma \cdot BR(V+\gamma)_{gen}$ by the following relationship:

$$\sigma \cdot BR(V+\gamma)_{cuts} = \sigma \cdot BR(V+\gamma)_{gen} \cdot \left(\frac{A'}{A}\right) \tag{D.3}$$

This is how the predicted cross sections in Ch. 6 are obtained from the fast Monte Carlo.

## D.2 $Z\gamma$ Acceptance

The acceptance for $Z\gamma$ processes is discussed in Ch. 6. The actual presentation there is simplified. Here I describe in detail how the $Z\gamma$ acceptance is calculated. Because there are two muons in a $Z$ decay, there are two chances to get at least one muon to hit a muon detector. The other muon may or may not pass through a muon detector. Each combination of where the two muons go leads to separate acceptance terms, which then need to be combined with the proper efficiencies. The full equation for the $Z\gamma$ $A \cdot \epsilon$ is:

$$\begin{aligned} A_{Z\gamma} \cdot \epsilon_{Z\gamma} = \frac{1}{f_{DY}} \cdot \epsilon_{zvx} \cdot A_{M_Z} \cdot (T \cdot \epsilon^{\mu}_{cent} \cdot \epsilon_{cos}) \\ \times [A_{Zcc} \cdot (2-T) \cdot (2\epsilon^{\mu}_{centL_1} - \epsilon^{\mu}_{centT}) \\ \cdot (f^{\gamma}_{Zcc} \cdot A^{\gamma}_{Zcc} \cdot \epsilon^{\gamma}_{cem}) \end{aligned}$$

$$+(A_{Zc\bar{c}} \cdot \epsilon^{\mu}_{cent_{L_2}}) \cdot (f^{\gamma}_{Zc\bar{c}} \cdot A^{\gamma}_{Zc\bar{c}} \cdot \epsilon^{\gamma}_{cem})] \tag{D.4}$$

The term $\frac{1}{f_{DY}}$ is a theoretical correction factor (97% for muons) which explicitly takes into account the removal of the Drell-Yan $DY + \gamma$ contribution to events in the $Z + \gamma$ data within the dimuon mass window [58]. It also corrects for the loss of $Z + \gamma$ events outside the dimuon mass window. The term $T$ is the total muon trigger efficiency.

Other terms not defined above are: $f^{\gamma}_{Zcc}$, the fraction of all photons in $Z\gamma$ events that are in the central region of the detector, when *both* muons are detected within the CMU or CMU+CMP fiducial volume (represented by the '$Zcc$'); $f^{\gamma}_{Zc\bar{c}}$, the fraction of all photons in $Z\gamma$ events that are in the central region of the detector, when one muon is in the CMU or CMU+CMP fiducial volume and the other is not (represented by the '$Zc\bar{c}$'). The acceptance terms $A^{\gamma}_{Zc\bar{c}}$ and $A^{\gamma}_{Zcc}$ can be written as

$$A^{\gamma}_{Zcx} = (A^{\mu_1}_{Zc\ P_T} \cdot A^{\mu_1}_{Zc\ fid}) \cdot (A^{\mu_2}_{Zx\ P_T} \cdot A^{\mu_2}_{Zx\ fid}) \tag{D.5}$$

where $Zcx = Zcc$ or $Zc\bar{c}$, $A^{\mu_1}_{Zx\ fid}$ is the geometrical fiducial acceptance associated with the central muon systems and $A^{\mu_1}_{Zx\ P_T}$ is the kinematic acceptance for the "tight" muon passing the $P_T > 20\ GeV/c$ cut. The term $A^{\mu_2}_{Zx\ P_T}$ is the kinematic acceptance for the "loose" second leg muon and $A^{\mu_2}_{Zx\ fid}$ is the geometrical acceptance for either the fiducial ($x = c$) or the non-fiducial ($x = \bar{c}$) second-leg muon. The second-leg muon is accepted

| Term | Acceptance value (%) |
|---|---|
| $A_{M_Z}$ | $85.27 \pm 0.08$ |
| $A_{Zcc}$ | $76.37 \pm 0.13$ |
| $A_{Zc\bar{c}}$ | $75.18 \pm 0.08$ |
| $f^{\gamma}_{Zcc}$ | $76.44 \pm 0.16$ |
| $f^{\gamma}_{Zc\bar{c}}$ | $76.61 \pm 0.09$ |
| $A^{\mu}_{Z\gamma}$ (Total) | $5.81 \pm 0.01$ |

**Table D.1**: Acceptances needed for $Z\gamma$ analysis. The total $Z\gamma$ acceptance includes both $Zcc$ and $Zc\bar{c}$ occurrences.

as long as it has a minimum ionizing track with $P_T > 20\ GeV/c$, and it has $|\eta| < 1.2$. These acceptance terms have values which are shown in Table D.1.

Finally the efficiency terms can be written as

$$\epsilon^{\mu}_{centT} = \epsilon_{iso} \cdot \epsilon_{had} \cdot \epsilon^{\mu}_{em} \cdot \epsilon_{cmuo} \cdot \epsilon_{trk} \cdot \epsilon_{cmudx} \tag{D.6}$$

where $\epsilon_x$ are the muon selection efficiencies listed in Table 5.1. The overall "loose" central fiducial and non-fiducial muon efficiencies are

$$\epsilon^{\mu}_{centL_1} = \epsilon_{had} \cdot \epsilon_{em} \cdot \epsilon_{cmuo} \cdot \epsilon_{trk} \tag{D.7}$$

for second-leg muons which go through the CMU or CMU+CMP, and

$$\epsilon^{\mu}_{centL_2} = \epsilon_{had} \cdot \epsilon_{em} \cdot \epsilon_{trk} \tag{D.8}$$

for second-leg muons which miss the muon coverage but are within $|\eta| < 1.2$. The values for all muon and photon efficiencies are listed in Ch. 5.

# Appendix E

# Photon Subtraction Algorithm at CDF

The method for estimating the QCD background for both the $W\gamma$ and $Z\gamma$ samples employs an algorithm which estimates the fraction of electromagnetic clusters in the background sample that result from single, prompt photons, as well as the fraction which results from multi-photon decays (such as $\pi^0$ decay). The algorithm [59] is discussed below.

The algorithm, which I'll refer to as the $\chi^2$−ratio method, uses strip (measures $z$ position) and wire (measures $x$ position) $\chi^2$ information from the CES detector. The idea is to compare the shower shapes of photon candidates to electron test-beam data, since a single isolated photon should look like an electron, minus the charged track. The CES has fine spatial resolution, which helps distinguish between one and two shower events. Multi-shower events will not match well with the test-beam shower shapes, and

it is here that one hopes to eliminate a large portion of the background to single photons. The transverse shower shapes are fitted and a $\chi^2$ comparison is made to test-beam data, thus providing a means of identifying good matches (the signal, which consists of single photons) as well as bad matches (photon backgrounds).

Unfortunately, the method does not work on an event-by-event basis. One reason for this is that there can be fluctuations in the shower itself, and what really was a good photon candidate could end up looking more like photon background. Also, one of the two photons from a $\pi^0$ decay can go into a crack in the calorimeter and thus look like a single photon. This algorithm works best with large statistics.

The subtraction of real photons from the 16 $GeV$ photon sample I used for the QCD background estimate, relies on "known" $\chi^2$ distributions for both the signal and backgrounds as a function of $E_T$. The electron test-beam transverse shower $\chi^2$ distributions are used in the QFL Monte Carlo to simulate single photons and $\pi^0$ decays. The average CES $\chi^2$ (the average of the strip and wire $\chi^2$) and the $E_T$ are the only data needed to use this algorithm. Efficiencies are obtained, for both signal and background, over some $E_T$ range from the Monte Carlo studies for events which had an average $\chi^2$ less than 4 as well as between 4 and 20. The efficiencies are defined as

$$\epsilon_\gamma = \frac{N^{\gamma_{MC}}_{\chi^2<4}}{N^{\gamma_{MC}}_{\chi^2<20}} \tag{E.1}$$

$$\epsilon_B = \frac{N^{B_{MC}}_{\chi^2<4}}{N^{B_{MC}}_{\chi^2<20}} \tag{E.2}$$

where $N^{\gamma MC}_{\chi^2<4}$ is the number of Monte Carlo produced photons with an average $\chi^2$ less than 4, and $N^{\gamma MC}_{\chi^2<20}$ is the number of Monte Carlo produced photons with an average $\chi^2$ less than 20. Equation E.2 uses the same convention, but for Monte Carlo produced background ($B$) events, such as $\pi^0$.

The following matrix form is used to predict the number of events with $\chi^2 < 4$ (more likely to be signal) and $4 < \chi^2 < 20$ (more likely to be background);

$$\begin{pmatrix} N_{\chi^2<4} \\ N_{\chi^2>4} \end{pmatrix} = \begin{pmatrix} \epsilon_\gamma & \epsilon_B \\ 1-\epsilon_\gamma & 1-\epsilon_B \end{pmatrix} \begin{pmatrix} N_\gamma \\ N_B \end{pmatrix} \qquad (E.3)$$

where $\epsilon_\gamma$ and $\epsilon_B$ are the $\chi^2$ efficiencies, as determined from Monte Carlo, for signal and background, and $N_{\chi^2<4}$ and $N_{\chi^2>4}$ are the number of events in the $E_T$ bin with $\chi^2 < 4$ and $4 < \chi^2 < 20$, respectively. $N_\gamma$ and $N_B$ are the actual number of photons and photon background events in the sample being studied.

The matrix can be inverted to obtain the prediction of the number of photons and the number of background in a particular sample

$$\begin{pmatrix} N_\gamma \\ N_B \end{pmatrix} = \frac{1}{\epsilon_\gamma - \epsilon_B} \begin{pmatrix} 1-\epsilon_B & -\epsilon_B \\ -(1-\epsilon_\gamma) & \epsilon_\gamma \end{pmatrix} \begin{pmatrix} N_{\chi^2<4} \\ N_{\chi^2>4} \end{pmatrix} \qquad (E.4)$$

Events can individually be assigned a weight for being signal or background by substituting (1,0) or (0,1) for ($N_{\chi^2<4}$,$N_{\chi^2>4}$), depending on the appropriate efficiencies and $E_T$ of the photon candidate. If each photon is assigned a weight, they can be added together to get an estimate of the number of events which are more like single prompt

photons and the number of events which appear to be more like photon backgrounds. This procedure led to the values found in Table 7.2. The statistical error on the number of estimated signal events is calculated by adding the squares of the individual signal weights and then taking the square root of the sum. The same method is used to obtain the statistical error on the estimate of the number of photon background events in the sample. The statistical errors associated with the signal and background estimates using the $\chi^2$ method are in general larger than the usual $\sqrt{N_{obs}}$ errors by a factor of $\sim \sqrt{2}$.

There are systematic errors also associated with the estimates of signal and background when using the $\chi^2$ method. They include uncertainties in photon shower corrections, the inclusion of energy [59] from the underlying event, effects of CES saturation during the data runs, and possible differences in the background mixtures of neutral mesons such as $\pi^0$ and $\eta$ in the data. Table 7.2 lists both the statistical and systematic errors for each $E_T$ bin, which are the result of using the $\chi^2$ method in the estimation of the QCD backgrounds in the $W\gamma$ and $Z\gamma$ event samples.

# Bibliography


[1] D. H. Perkins, *Introduction to High Energy Physics*, Third Edition, (Addison-Wesley Publishing Company, Inc., Menlo Park,1987) Pp. 314-340.

[2] F. Abe *et al*, Phys. Rev. D**50**, 2966 (1994).

[3] D0 Collaboration, Phys. Rev. Lett. **72**, 2138 (1994).

[4] U. Baur and E. L. Berger, Phys. Rev. D**41**, 1476(1990).

[5] K. Hagiwara et al., Nucl. Phys. B**282**, 253 (1987).

[6] U. Baur, S. Errede and G. Landsberg, to be published in Phys. Rev. D.

[7] T.D. Lee and C.N. Yang, Phys. Rev. **128**, 885 (1962).

[8] Review of Particle Properties, Phys. Rev. D**45**, VIII.8 (1992).

[9] U. Baur and D. Zeppenfeld, Nucl. Phys. B**308**, 127 (1988).

[10] J. Smith, D. Thomas and W.L. van Neerven, Z. Phys. C**44**, 267 (1989).

[11] U. Baur and E.L. Berger, Phys. Rev. D**47**, 4889 (1993).

[12] Private communication from U. Baur.

[13] F. Abe, *et al*, to be submitted to Phys. Rev. D (1994).

[14] D. Benjamin, Ph.D. Thesis, Tufts University (1993).

[15] D. Griffiths, *Introduction to Elementary Particles*, (Harper and Row, New York, 1987) P. 249.

[16] F. Abe et al., Nucl. Instr. and Meth. A271 (1988) 387-403.

[17] The SVX of the Collider Detector at Fermilab, Nucl. Instr. and Meth., to be published.

[18] F. Bedeschi *et al*, Nucl. Instr. and Meth. A**268**, 50 (1988).

[19] Private communication with Sacha Kopp.

[20] S. Bhadra *et al*, Nucl. Instr. and Meth. A**268**, 92 (1988).

[21] L. Balka *et al*, Nucl. Instr. and Meth. A**267**, 301 (1988).

[22] D. Saltzberg, Ph.D. Thesis, University of Chicago (1994).

[23] S. Bertolucci *et al*, Nucl. Instr. and Meth. A**267**, 280 (1988).

[24] F. Abe *et al*, Nucl. Instr. and Meth. A**271**, 387 (1988).

[25] G. Ascoli *et al*, Nucl. Instr. and Meth. A**267**, 218 (1988).

[26] A. Gauthier *et al*, to be submitted to Nucl. Instr. and Meth.

[27] G. Brandenburg *et al*, to be submitted to Nucl. Instr. and Meth.

[28] P. Schlabach, Ph.D. Thesis, University of Illinois at Urbana-Champaign (1990).

[29] U. Baur and E.L. Berger, Phys. Rev. D**41**, 1476 (1990).

[30] U. Baur and E.L. Berger, Phys. Rev D**47**, 4889 (1993).

[31] VEGAS, G. Peter Lepage, J. Comp. Phys. **27**, 192-202, Academic Press (1978); G. Peter Lepage, CLNS-80/447 (1980).

[32] PDFLIB, H. Plothow-Besch, Computer Phys. Comm. **75**, 396 (1993).

[33] A.D. Martin, R.G. Roberts and W.J. Stirling, Phys. Lett. B**306**, 145 (1993).

[34] M. Kobayashi and M. Maskawa, Prog. Theor. Phys. **49**, 652 (1973).

[35] F. Abe *et al*, to be submitted to Phys. Rev. Lett. (1994).

[36] The VVJET Monte Carlo, U. Baur, E.W.N Glover and W.J. Stirling, Phys. Rev. D**42**, 798 (1990).

[37] M. Lindgren, CDF Internal Note 1952 (1993).

[38] ISAJET Monte Carlo, F.E. Paige and S.D. Protopopescu, BNL Technical Report No. 38034, 1986 (unpublished).

[39] C. Luchini, Ph.D. thesis, University of Illinois at Urbana-Champaign (1993).

[40] P.N. Harriman, A.D. Martin, R.G. Roberts and W.J. Stirling, Phys. Rev. D**42**, 798 (1990).

[41] A.D. Martin, R.G. Roberts and W.J. Stirling, Phys. Rev. D**47**, 867 (1993).

[42] J. Botts *et al*, Phys. Lett. B**304**, 159 (1993).

[43] F. Abe *et al*, Phys. Rev. Lett. **66**, 2951 (1991).

[44] P.B Arnold and M.H Reno, Nucl. Phys. B**349**, 381 (1991).

[45] U. Baur, S. Errede, and J. Ohnemus, Phys. Rev. D**48**, 4103 (1993).

[46] W. Badgett, private communication.

[47] MINUIT, F. James and M. Roos, CERN Report D506, 1988.

[48] F. Abe, *et al.*, to be submitted to Phys. Rev. D (1994).

[49] VECBOS Monte Carlo, F.A. Berends , W.T. Giele, H. Kuijf and B. Tausk, Nucl. Phys. B**357**, 32 (1991).

[50] HERWIG Monte Carlo, G. Marchesini and B.R. Webber, Nucl. Phys. B**310**, 461 (1992).

[51] S.D. Ellis, R. Kleiss and W.J. Stirling, Phys. Lett. B**154**, 435 (1985).

[52] R.G. Wagner, Comp. Phys. Commun. **29**, 15 (1992).

[53] F.A Berends and R. Kleiss, Z. Phys. C**27**, 365 (1985).

[54] F. James, Comp. Phys. Comm. **20** (1980), p. 29-35.

[55] The Illinois group which built the CMP detector was led by Prof. Tony Liss and included Dr. Alain Gauthier, Randy Keup, Andrew Martin and Mark Vondracek.

[56] F. Abe *et al*, Phys. Rev. Lett. **45**, 1448 (1992).

[57] D. Brown, Ph.D. Thesis, Harvard University (1989).

[58] F. Abe *et al.*, Phys. Rev. Lett. **62**, 1005 (1989); F. Abe *et al.*, Phys. Rev. D**44**, 29 (1991).

[59] L. Nakae, Ph.D. Thesis, Brandeis University (1992).

[redacted]

Mark Frank Vondracek [redacted] Little did young Mark know he would always live within 10 miles of that spot for the first 18 years of his life, and never make it out of this grand state of corn and soybeans. Mark graduated from Streamwood High School in 1986 and then decided to attend the University of Illinois at Urbana-Champaign to enjoy some Big Ten sports with his friends. He started in the physics curriculum and remained there to this date. A Bachelor's of Science degree was earned in 1990, and Mark thought about graduate school. He had worked for Tony Liss, a professor of physics in Urbana, during his senior year on some muon drift chambers. That was pretty neat, so Mark started a graduate career at UIUC. He had all sorts of fun with the qualifying exam, and persistence paid off. After receiving his Master's degree in physics on a cold day in January, 1992, Mark set his sights on the grand-daddy of 'em all, the doctorate degree. Chambers were installed, data was taken, and Mark took off with some dibozos to look for that one breathtaking discovery that would shatter the Standard Model! Well, if you made it this far you know how that turned out.